Abstract

This Thesis concerns two subjects: the dynamics of ripples beneath surface waves and shell models of turbulence.

For the study of ripples, a computational model is developed (chapter 2). The model consist of a flow model, a sediment transport model and a morphological model. Using this model as the main tool, the dynamics of the ripples are studied. First the formation of ripples on a flat bed is described (chapter 3). Here a granular model for the formation of rolling grain ripples is developed. The model shows that the spacing between the rolling grain ripples are proportional to $\sqrt{\theta - \theta_c} d$ where θ is the Shields parameter, θ_c is the critical Shields parameter and d is the grain diameter. In the chapters 4 and 5 the flow and the sediment transport are examined. Focus is on the size and the strength the separation bubble. The sediment transport can be classified into two regimes: one where the sediment transport is dominated by near-bed sediment transport when the settling velocity is large and a regime where the sediment transport is dominated by advected suspension for small settling velocities. Another important finding is that the flow and sediment transport over fixed ripples is very close to that over moving ripples. The dynamics of the ripples are explored in chapter 6 using morphological calculation. A stability analysis of the fully developed ripple profiles is performed and the minimal wave length of the ripples is calculated. A simple model, based on the ripples represented as particles, is developed to illustrated the dynamics of the ripples.

Two topics in shell models of turbulence are treated in chapter 8. The first is the continuous and zero-spacing limits of the GOY model. The model was found to be dominated by pulse solutions, with a behaviour similar to that of the KdV-equation. Finally a minimal shell model for the advection of a passive scalar by a Gaussian time correlated velocity field is studied. The anomalous scaling properties of the white noise limit are studied analytically. The effect of the time correlations are investigated using perturbation theory around the white noise limit and non-perturbatively by numerical integration.

Abstract in danish

Denne Thesis omhandler to emner: dynamikken af riller under overfladebølger og skal-modeller for turbulens.
For at kunne studere riller er en numerisk model blevet udviklet (kapitel 2). Modellen består af en strømningsmodel, en sedimenttransportmodel og en en morfologisk model. Ved at bruge denne model som værktøj studeres dynamikken af rillerne. Først bliver dannelsen af rillerne fra en flad bund beskrevet (kapitel 3). Her udvikles en granular model som beskriver dannelsen af rullekornsriller. Denne model viser at afstanden mellem rillerne er proportional med $\sqrt{\theta - \theta_c}d$ hvor θ er Shields parameteren, θ_c er den kritiske Shields parameter og d er korndiameteren. I kapitlerne 4 og 5 bliver strømningen og sedimenttransporten undersøgt. Fokus er på størrelsen og styrken af seperationsboblen. Sedimenttransporten kan klassificeres i to regimer: et hvor sedimenttransporten er domineret af transport tæt på bunden for store flad-hastigheder, og et hvor sedimenttransporten er domineret af advekteret opslemmet transport for små fald-hastigheder. Et andet vigtigt resultat er, at strømningen og sedimenttransporten over faste og bevægelige riller er stort set ens. Dynamikken af riller er undersøgt i kapitel 6 v.h.a. morfologiske beregninger. En stabilitetsanalyse af de fuldt udviklende riller bliver udført, og den minimale bølgelængde beregnet. En simpel model, baseret på rillerne repræsenteret som partikler, bliver udviklet for at illustrere dynamikken af rillerne.
To emner i skalmodeller af turbulens er behandlet i kapitel 8. Den første er kontinuums eller nul-afstands-grænsen for GOY modellen. Det blev fundet at modellen er domineret af puls-løsninger, med en opførsel der svarer til KdV-ligningen. Endelig bliver en minimal skal-model for advektionen af en passiv skaler af et Gaussisk tids-korrelleret hastighedsfelt studeret. Den anormale skalering af grænsen med hvid støj er studeret analytisk. Effekten af tid-korrelationen er undersøgt v.h.a. perturbationsteori omkring grænsen for hvid støj og udover grænsen hvor perturbationsteori gælder v.h.a. numerisk integration.

"A large step for me,
a small step for mankind."

Preface

The present Thesis is the outcome of three years work as a Ph.D. student in theoretical physics. The work was carried out partly at the Centre for Chaos and Turbulence Studies group (CATS), the Niels Bohr Institute at the University of Copenhagen, and partly at the Institute of Hydraulic Research and Water Resources (ISVA), The Technical University of Denmark, in the period January 1th 1996 to March 1th 1999.

The work presented here are partly on the subject of ripples beneath surface waves and partly on shell models of turbulence. The main part of the Thesis is concerned with the ripples. Only a small part concerning simulations of the friction and roughness of a flow over a rippled bed has been submitted for publication (the attached article "Wave plus current over a ripple-covered bed"). The rest has not yet been submitted for publication. The work on shell models has been done in collaboration with various other people from the NBI, and have all been submitted for publication. This work is therefore mainly reported in the attached articles, and only a brief introduction is given (chapter 8).

I am indebted to the my colleges at the CATS and at ISVA for providing the inspiration needed to undertake a Ph.D. study, in particular my supervisors Tomas Bohr and Jørgen Fredsøe. A thanks goes to those who have commented on the present text, and thus helped to make it somehow readable: Martin van Hecke, Jacob Hjelmager Jensen, Vachtang Putkaradze and Kirsten Djørup. A particular thanks goes to Anna for showing extraordinary patience with me in the months when the Thesis were written.

The study was founded jointly by the Danish Technical Research Council (STVF) under the program "Marin Teknik II" and by the Commission of the European Communities, Directorate-General XII for Science, Research and Development Program Marine Science and Technology Contract No. MAS 2 CT 92-0027, and Contract No. MAS3-CT97-0115 (SEDMOC).

List of symbols

a	The amplitude of the oscillatory motion in a wave.
a_g	The amplitude of the oscillatory motion of a single grain.
α	Wavenumber of the ripple.
α_s	The length of the shadow zone divided by the height.
β	The factor for a linear gravity correction in the bed load.
γ	The slope of the bed.
$C(t)$	Growth of perturbation.
c	Time averaged growth rate of a perturbation.
$c(x,y,t)$	The concentration of suspended sediment.
c_b	Bed boundary condition for suspended sediment.
C_D	Drag coefficient.
d	The grain diameter.
δ	The viscous boundary layer thickness: $\delta = \sqrt{2\nu'/\omega'}$.
Δx_{crest}	The distance between grid points near the crest.
Δm	The amount of mass transfered over the trough between two ripples.
ϵ	The height of a perturbation on the bed (small).
ϵ_d	The dissipation of the wave due to the presence of ripples.
f_e	The dissipation factor.
f_{ew}	The wave-only dissipation.
f_{wc}	The wave plus current friction factor.
g	The gravitational acceleration.
h	The height of the ripple measured from trough to crest.
$h(x,t)$	The height of the bed.
κ	von Kármán's constant.
k_N	The Nikuradse roughness.
k_{wc}	The Nikuradse roughness of a wave plus current flow.
L	The length of the computational domain.
λ	The length of the ripple.
λ_{equ}	The equilibrium wave length.
λ_f	Average initial distance between the centers of the grains in the simple model of rolling grain ripples.
λ_m	The marginal wave length.
λ_{max}	The maximum wave length of a ripple.
λ_{sep}	The maximum extent of the separation bubble.
M	The number of grid points in the vertical direction.
μ_D	The dynamics friction.
μ_S	The static friction.

n	The porosity of the bed.
n	The number of grain per area in motion as bed load.
N	The number of grid points in the horizontal direction.
ν	The kinematic viscosity.
ω	Angular frequency. In the k-ω model ω is the dissipation of turbulent kinetic energy.
ψ	The mobility number.
ϕ	The angle of repose for sand.
ϕ_b	Non dimensional bed load.
ϕ_s	Non dimensional suspended load.
ϕ_t	Non dimensional total load.
q_b	The mass flux of sand pr. width due to bed load.
ρ	The density of water.
ρ_s	The density of the sediment.
Re_D	Reynolds number using the depth: $Re_D = U_m D/\nu$.
Re_d	Reynolds number using the grain diameter: $Re_d = U_m d/\nu$.
Re_δ	Reynolds number using the viscous boundary layer thickness: $Re_\delta = U_m \delta/\nu$.
s	The relative density of sediment; $s = \rho_s/\rho$.
τ_b	Shear stress on the bed.
θ	The Shields parameter.
θ'	The maximum Shields parameter on a flat bed.
θ_c	The critical Shields parameter for initiation of grain motion.
$\theta_{c\gamma}$	The critical Shields parameter corrected for a sloping bed.
U_b	The velocity of a grain.
U_c	The depth-averaged steady current component of the horizontal velocity.
U_m	The amplitude of the velocity.
U_f	The friction velocity, $U_f = \sqrt{\tau/\rho}$.
U_f'	The maximum friction velocity on a flat bed.
V	The vertical velocity.
w_s	The settling velocity.
Δx	The distance between two rolling grain ripples.
Δx_{crest}	The grid spacing near the crest of the ripple.
y	Height above the bed.
y_0	Height above the bed where the velocity used for the determination of the bed load is taken.
y^+	Non-dimensional distance from the bed; $y^+ = yU_f/\nu$.

Notation

$\langle\ \rangle_x$	Spatial average over one ripple.
$\langle\ \rangle_t$	Time average over one wave period.
$\langle\ \rangle_{1/2}$	Time average over one half wave period.
$'$	Maximum value on a flat bed.

Contents

Abstract iii

Abstract in danish iv

Preface v

List of symbols vi

1 Introduction 1
- 1.1 Ripples 2
- 1.2 Dimensional analysis 5

2 The computational model ix
- 2.1 The flow module ix
  - 2.1.1 Turbulent closure using the k-ω model x
- 2.2 The boundary conditions xvi
- 2.3 The numerical solver xvii
- 2.4 Modelling the sediment transport xix
  - 2.4.1 The bed load xx
  - 2.4.2 Corrections to the bed load and the bed BC for suspended transport xxiii
  - 2.4.3 The final sediment transport model xxv
- 2.5 Morphological calculations xxvii
- 2.6 Grid independence of the solutions xxviii
  - 2.6.1 Grid sensitivity of the flow xxviii
  - 2.6.2 Grid sensitivity for suspended transport xxx

3 Initiation of ripples xxxiii
- 3.1 The rolling grain ripples xxxiii
- 3.2 A simple granular model of rolling grain ripples xxxv
  - 3.2.1 Formulation of the model xxxv
  - 3.2.2 Numerical and analytical solutions of the model xl

3.2.3 Comparison with experiments xlii
3.3 Linear stability analysis xliv
3.3.1 Mathematical formulation of the problem xlv
3.3.2 Results xlix
3.3.3 Dependence on parameters l
3.4 Creation of vortex ripples via nucleation liii
3.5 Concluding remarks liv

4 The flow around vortex ripples 57
4.1 Previous efforts (and some more recent) 58
4.1.1 Comparison with experiments 60
4.1.2 Live vs. fixed ripples 60
4.2 Wave-only flows 61
4.2.1 Vortex dynamics 61
4.2.2 The evolution of the separation bubble 65
4.3 Wave plus current flow conditions 69
4.4 Integrated flow quantities 72
4.4.1 The dissipation 74
4.4.2 Comparison with "live" ripple 76
4.5 Turbulent kinetic energy 79
4.6 Summing up 79

5 Sediment transport over ripples 81
5.1 Four test cases 81
5.2 Sediment transport in wave plus current situations 87
5.3 Summing up 92

6 The dynamics of vortex ripples 93
6.1 Measurements of ripple geometry 93
6.2 Qualitative dynamics of the ripples 96
6.3 Stability analysis 101
6.3.1 The exchange of sediment between ripples 102
6.3.2 Results 108
6.4 The stability analysis using fixed profiles 110
6.5 A simple model of the dynamics of ripples 113
6.5.1 Results 116
6.6 The equilibrium profile of ripples 118
6.6.1 Results 120
6.7 Waves plus current 120
6.8 Summing up 123

7 Discussion 125
7.1 A qualitative bifurcation diagram 125
7.2 Summary of main findings 126

8 Topics In Shell Models of Turbulence 129
8.1 The GOY model 130
8.1.1 Properties of the GOY model 131
8.2 Continuous limit of the GOY model 132
8.2.1 ϵ-expansion 132
8.2.2 The zero-spacing limit 133
8.3 Advection of a passive scalar 133

Attached articles 143

Chapter 1

Introduction

In Nature a free surface of sand is mainly found in three different environments: in deserts, in rivers and in the sea, particularly the coastal zone. The sand surface is rarely flat but is covered with patterns created by the motion of the surrounding fluid: air or water. A flat surface only exists either where there is not enough motion in the surrounding fluid to disturb the sand, or if the motion is so strong that the boundary between the fluid and the sand is a thick slurry of moving mixture of sand and water. The encyclopædia of the patterns in sand describes a large variety of patterns and covers length and time scales from millimetres and seconds – rolling grain ripples in the sea – to thousands of kilometres and years for the draas in the desert.

In the desert one finds small ripples, believed to be created by the saltation of single grains (Anderson, 1990; Hoyle and Woods, 1997; Terzidis *et al.*, 1998; Nishimori and Ouchi, 1993; Csahók *et al.*, 1998). These ripples usually exist on top of larger structures: the dunes. The family of dunes contain several sub-branches, e.g., barchan dunes, created when the sand is eroded down to the solid bed and transverse dunes created when there is plenty of sand. These two kinds of dunes are aligned with the crest perpendicular to the dominant wind direction. When the wind is alternating between two predominant directions, longitudinal dunes with the crest aligned parallel to the wind is created. When the wind is alternating between more than two direction star dunes are created (see the attached article no. I: (Nishimori *et al.*, 1998). The largest and oldest patterns in the desert are the draas, which are believed to be relict structures, created by rolls in the planetary boundary layer.

In rivers the ripples are again discovered. Here, however, there is no saltation of the grains, and the origin of the ripples is controversial (see e.g. Raudkivi (1997)). Another difference with the ripples formed by the wind is that the steady state pattern of ripples in water is very two dimensional, while the ripples in the desert form a nearly one dimensional pattern with few defects. Dunes formed on a river bed comes in two varieties: ordinary dunes, moving in the same direction as the current, and anti dunes which are moving against the current (for a review of dunes in rivers see Fredsøe (1996)).

The coastal zone differs from the deserts and the rivers in one important aspect, namely that the predominant flow is created by the waves and only secondarily by a current superposed on top of the waves. Patterns created by waves are the rolling grain ripples and the vortex ripples. Due to a combination of the long-shore current and the oscillatory action of the waves, yet another pattern can be observed, namely the mega ripples (Gallagher *et al.*, 1998). Finally the oscillatory motion of the tidal wave creates large structures known as sand waves (Hulcher, 1996).

Even though many similarities between all these features can be recognised, they are generally created by different mechanisms. It is therefore not thought that all of these features can be described by one general theory. For the major part of them, the flow of the air or water around them is very important as it determines the transport of sand.

What makes these patterns particularly difficult to describe mathematically is the granular nature of the sand. One of the manifestations of this is that once a pattern has been made, it does not disappear even when the wind or the current that generated the pattern vanishes. This illustrates the strong sub-critical nature of the patterns, a property which makes them difficult to treat with perturbative methods such as amplitude equations.

This Thesis deals with the ripples that are generated by the waves in the coastal zone. Both the rolling grain ripples and the larger vortex ripples will be studied.

1.1 Ripples

The subject of ripples generated by an oscillatory flow is quite rich. As indicated above there are at least two distinct types of ripples. Secondly the ripples have a complex phase diagram with different equilibrium shapes and sizes, and in some areas they have many defects and surprising interactions.

The most important type of ripples is the *vortex ripple* (figure 1.1), labelled so by Bagnold (1946). The vortex ripple has also been referred to as the orbital ripple (Wiberg and Harris, 1994) reflecting the fact that the length of the ripple is a function of the orbital amplitude of the wave motion. The vortex ripples are triangular in shape, with the slope of the sides being close to the angle of repose. The flow around the ripples is dominated by

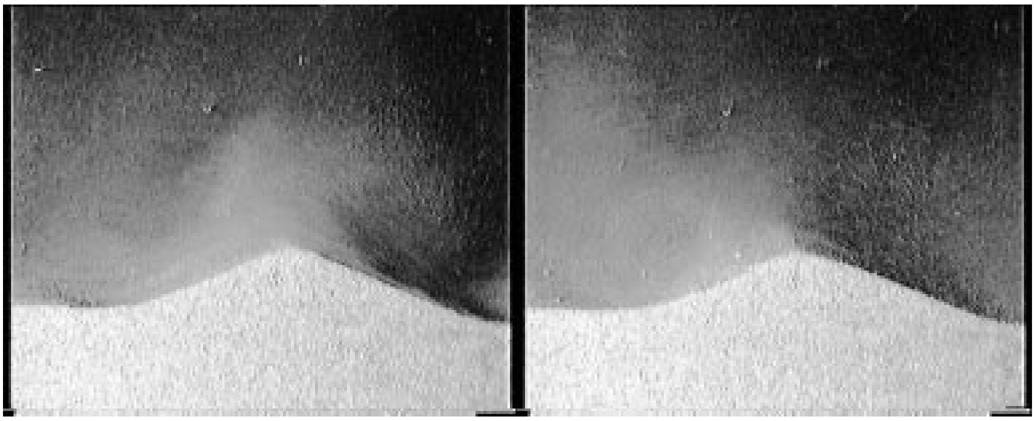

Figure 1.1: Two snapshots of a vortex ripple. In the left picture the flow has just reversed, and a cloud of sediment is thrown over the crest. In the right picture a strong separation bubble is seen in the left side of the ripple, carrying a lot of sediment

the vortices created by the crest in the lee side of the ripples. The sediment transport is dominated by avalanches of sand rolling down on the sides of the ripples. The vortex ripples are the dominant pattern in the coastal zone where they make significant contributions to the roughness of the bed and the dissipation of the waves (section 4.4). They induce a sediment transport which is much bigger than there would have been if the bed was flat (chapter 5). This is especially interesting for the case where waves are superposed by a current (wave plus current flows), where the net sediment transport can even be opposing the main current (section 5.2). An important and not well understood property of the vortex ripples is their equilibrium wave length; this will be explored in chapter 6.

The study of the vortex ripples forms the core of this Thesis. To this end an advanced computational model for the flow and sediment transport has been employed (chapter 2), which is able to describe the two-dimensional flow over a one-dimensional train of ripples in great detail. The idea behind using the advanced model is to construct a numerical laboratory where the ripples can be studied under "clean" conditions. This means that a very simple set up has been used: the flow over the ripples is only sinusoidal. Consequently many of the effects related to real waves are not resolved, i.e., orbital motion, streaming in the boundary layer, and asymmetric oscillatory motion. All these effects might be relevant, especially for the sediment transport, but since the ideal case described above is far from being well understood, it was felt that to understand the influence of these more complicated effects, a thorough understanding of the ideal case was required to form a solid base.

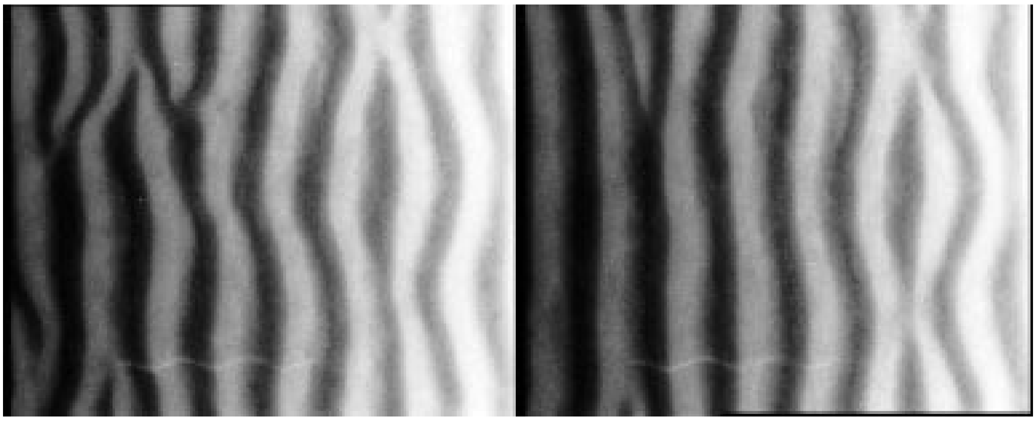

Figure 1.2: An example of a two-dimensional pattern of vortex ripples taken from an experiment at the NBI, at two times. Defects in the pattern are seen in the top left corner and in the right side. The bright line in the bottom of the picture is due to a laser beam used to extract a ripple profile.

A major goal has been to distill the knowledge obtained from the study of the model into a simple model illustrating the dynamics of the ripples (section 6.5).

The dynamics of a two-dimensional bed filled with vortex ripples can show some very interesting pattern dynamics (see for example figure 1.2). Unfortunately it has not been possible to cover these aspects of the vortex ripples in the present work, which focuses only on one-dimensional ripples.

Of more academic interest is the other ripple state, the *rolling grain ripple*, first described by Bagnold in 1946. This kind of ripple is formed on a flat bed and consists of small triangular heaps, spaced by a stretch of flat bed, much longer than the height of the triangular heap. The heaps are ordered in nice straight bands, thus forming a basically one-dimensional pattern. Although the rolling grain ripples also form a vortex in the lee side, this vortex is not dominant in the wave length selection as is the case for the vortex ripples. A theory based on the motion and amalgamation of single grains into the ripples is developed in section 3.2. The classical theory on the creation of rolling grain ripples by Blondeaux and co-workers (Blondeaux, 1990; Vittori and Blondeaux, 1990; Vittori and Blondeaux, 1991; Foti and Blondeux, 1995b; Foti and Blondeux, 1995a; Blondeaux *et al.*, 1996) is presented and discussed in section 3.3.

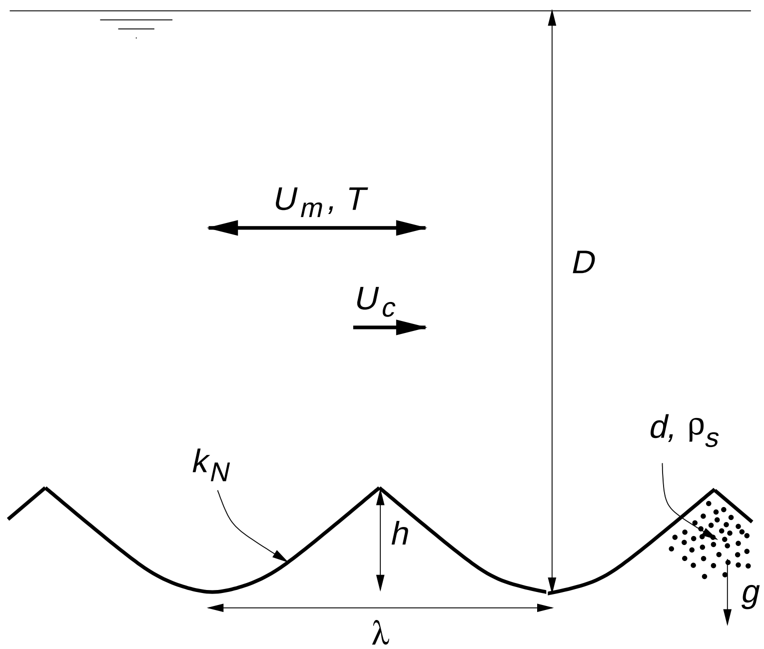

Figure 1.3: The dimensional quantities appearing in the ripple problem.

1.2 Dimensional analysis

Ever since Rayleigh in 1915 [1], scolded his colleagues for wasting their time on trivialities it has been known that a good starting point for the study of a physical system is a dimensional analysis:

> "It happens not infrequently that results in form of "laws" are put forward on the basis of elaborate experiments, which might have been predicted *a priori* after of few minutes of consideration".

With "a few minutes of consideration" he refers to the dimensional analysis, which he called "The principle of similitude". The problem of ripples involves a significant number of dimensional quantities, which can be combined in many ways, some meaningful, some not. The present choice is not invented out of thin air, but represents the combined efforts of many researchers through half a century of work on sediment transport and ripples.

Considering the flow over ripples, the following dimensional quantities are involved (figure 1.3):

[1]See also the ongoing discussion in the same volume of Nature for several letters regarding this article and replys by Rayleigh.

λ – the length of the ripples.
h – the height of the ripples.
U_m – the amplitude of the oscillatory flow.
T – the period of the oscillatory flow.
D – the depth of the flow.
k_N – the Nikuradse roughness of the bed.
ν – the kinematic viscosity of the fluid.
U_c – the current strength in a wave plus current flow.

With eight dimensional quantities and only two fundamental dimensions, time and space (the density has been excluded by using the kinematic viscosity instead of the dynamical viscosity), it is possible to form six non-dimensional quantities. The oscillatory flow sets the most important length scale, namely the amplitude of the motion of the fluid:

$$a = \frac{U_m T}{2\pi}. \tag{1.1}$$

The ripples can then be described by two parameters: λ/a and the steepness h/λ. For wave-only flow there are three parameters describing the flow, the Reynolds number $Re_a = aU_m/\nu$, the depth D/a, and the roughness k_N/a. For a fully developed turbulent flow the Reynolds number becomes unimportant. As the drag on the bed is mainly carried by the ripples and not by the individual grains, the roughness of the bed is also of minor importance (as long as $k_N \ll h$). The situations investigated involves depths much larger than the boundary layer created by the ripples, suggesting that the depth becomes unimportant as well. It turns out that the most relevant parameters are the length and the steepness of the ripples, i.e., λ/a and h/λ. If a current is added, the parameter U_c/U_m relating the current strength and the wave strength comes into play together with the depth D/a.

Adding sediment transport to the problem makes the dimensional analysis much more complicated. Three new parameters are added to the problem:

d – the grain diameter.
g – the gravitational acceleration.
ρ_s – the density of the sediment.

which implies that three new non-dimensional quantities are created. The relative density is the ratio between the sediment and the water $s = \rho_s/\rho$. For quartz sand (and glass spheres) $s \simeq 2.65$. This quantity is kept constant in the present work. There are many possible ways to create the remaining two quantities. The choice made here is to use the maximum value of the

Shields parameter on a flat bed:

$$\theta' \equiv \frac{\tau_b'}{\rho g(s-1)d}. \tag{1.2}$$

τ_b is the shear stress on the bed and the prime denotes the maximum value on a flat bed during the wave period. This parameter will be discussed in more detail in section 2.4.1, but for now it suffices to regard it as a non-dimensional shear stress. For laminar flow τ_b' can be found exactly from the Navier-Stokes equations as the solution of Stokes' second problem (Landau and Lifshitz, 1959):

$$\tau_b' = U_m\sqrt{\omega\nu} \tag{1.3}$$

where ω is the angular frequency of the wave.

For turbulent conditions, the shear stress on a flat bed can be found using the constant friction factor of Jonsson (1976)

$$\tau_b' = \frac{1}{2}\rho f_w U_m^2, \tag{1.4}$$

with a relation for the wave friction factor f_w:

$$f_w = 0.04\left(\frac{a}{k_N}\right)^{-0.25}, \quad \frac{a}{k_N} > 50, \tag{1.5}$$

which is a fit to the numerical solution of the integrated momentum equation for the wave boundary layer (Fredsøe and Deigaard, 1992). The final parameter is the settling velocity, made non-dimensional with the flow velocity: w_s/U_m. The reciprocal of this quantity is a measure of how far a grain can be transported by the flow. The settling velocity can be found from:

$$w_s = \sqrt{\frac{4(s-1)gd}{3C_D}}. \tag{1.6}$$

For a sphere the drag coefficient C_D is given by the Stokes formula:

$$C_D = \frac{24}{Re}, \tag{1.7}$$

where $Re = w_s d/\nu$. For natural sand the drag is given by the empirical relation (Fredsøe and Deigaard, 1992):

$$C_D = 1.4 + \frac{36}{Re}. \tag{1.8}$$

The complete set of non-dimensional parameters reads:

$$\boxed{\frac{\lambda}{a},\ \frac{h}{\lambda},\ \theta' \ \text{ and } \ \frac{w_s}{U_m}}$$

being of major importance and

$$\frac{k_N}{a},\ \frac{D}{a},\ Re_a \ \text{ and } \ s$$

being of minor importance, supplemented by

$$\boxed{\frac{U_c}{U_m} \quad \text{and} \quad \frac{D}{a}}$$

for wave plus current situations.

Chapter 2

The computational model

The model which has been developed for the numerical calculations is a quite complex system. The model is split into three modules: the flow module (section 2.1), the sediment transport module (section 2.4) and the morphological module (section 2.5). In this chapter the equations used in the model are described together with a brief overview of the underlying numerical solver (section 2.3). Particular attention is paid to the derivation of the equations for the transport of sand.

The equations in boxes, are the ones which are actually used and solved by the model.

2.1 The flow module

The turbulent flow around ripples is resolved based on a turbulent closure of the Reynolds-averaged Navier-Stokes (RNS) equations, which are derived from the Navier-Stokes equations (here written in tensorial notation):

$$\frac{\partial u_i}{\partial t} + u_j \frac{\partial u_i}{\partial x_j} = -\frac{1}{\rho}\frac{\partial p}{\partial x_i} + 2\nu \frac{\partial s_{ij}}{\partial x_j} \tag{2.1}$$

$$\frac{\partial u_i}{\partial x_i} = 0 \tag{2.2}$$

u_i is the velocity, p is the pressure, ρ the density and ν the kinematic viscosity. The strain-rate tensor is defined as

$$s_{ij} = \frac{1}{2}\left(\frac{\partial u_i}{\partial x_j} + \frac{\partial u_j}{\partial x_i}\right). \tag{2.3}$$

The Reynolds-averaging is effected by splitting the velocity into mean and fluctuation parts, U_i and u_i' respectively. These are inserted in (2.2) and (2.2) and the equations are averaged, resulting in the RNS equations:

$$\boxed{\begin{aligned} \frac{\partial U_i}{\partial t} + U_j \frac{\partial U_i}{\partial x_j} &= -\frac{1}{\rho}\frac{\partial P}{\partial x_i} + \frac{\partial}{\partial x_j}\left(2\nu \frac{\partial S_{ij}}{\partial x_j} - \overline{u_j' u_i'}\right). \\ \tfrac{\partial U_i}{\partial x_i} &= 0 \end{aligned}} \tag{2.4}$$

Apart from the replacement of instantaneous variables by mean values the only difference between (2.2) and (2.4) is the appearance of the correlation $\tau_{ij} = -\overline{u_j' u_i'}$; the Reynolds stress tensor. The trace of τ_{ij} is called the turbulent kinetic energy, $k = -\frac{1}{2}\tau_{ii}$.

The equations are closed using the eddy viscosity concept. By analogy with the molecular viscosity, the Reynolds stress tensor is modelled as:

$$\boxed{\tau_{ij} = \nu_T \frac{\partial S_{ij}}{\partial x_j} - \frac{2}{3} k \delta_{ij}.} \tag{2.5}$$

The second term on the right hand side is needed to obtain the proper trace of τ_{ij}. ν_T is referred to as the turbulent viscosity or the eddy viscosity. The effect of the eddies, which are averaged out by the Reynolds-averaging, is therefore modelled as a diffusion process with a time- and space-varying diffusivity.

2.1.1 Turbulent closure using the k-ω model

To calculate the eddy viscosity as a function of time and space, a turbulence model will have to be applied. The simplest model is to set ν_T to a constant or using a fixed variation in the vertical. This can be done with some success on a flat bed, but for the more complicated flow around ripples a more elaborate model need to be applied. Numerous models exist (for a review see Wilcox (1993b)), but the most commonly used are the so-called two-equations models, with the k-ϵ model being particularly popular. Although the turbulence models are sometimes presented as being more or less derived from the RNS equations (2.4), it is more correct to say that they are very advanced semi-empirical models, loosely based upon the RNS equations, physical reasoning, and dimensional arguments.

In the present work the k-ϵ model have been abandoned, mainly for two reasons: 1) the boundary conditions on a rough bed in an unsteady flow, are not very satisfactory, and 2) it is known to perform badly in areas with strong adverse pressure gradients, which is exactly the case for areas with, or close to, separation (Bradshaw, Launder, and Lumley, 1996; Wilcox, 1993a).

The k-ω model of Wilcox (Wilcox, 1988; Wilcox, 1993b) does not share these deficiencies and has therefore been employed with success.

On dimensional grounds, the eddy-viscosity is given as:

$$\boxed{\nu_T = \gamma^* \frac{k}{\omega},} \tag{2.6}$$

where γ^* is a model constant. The quantities k and ω are determined from the model equations (Wilcox, 1993b):

$$\boxed{\begin{array}{lllllll} \dfrac{\partial k}{\partial t} + U_j \dfrac{\partial k}{\partial x_j} & = & \dfrac{\partial}{\partial x_j}\left[(\nu + \sigma^* \nu_t)\dfrac{\partial k}{\partial x_j}\right] & - & \overline{u_i u_j}\dfrac{\partial U_i}{\partial x_j} & - & \beta^* k \omega \\ \dfrac{\partial \omega}{\partial t} + U_j \dfrac{\partial \omega}{\partial x_j} & = & \dfrac{\partial}{\partial x_j}\left[(\nu + \sigma \nu_t)\dfrac{\partial \omega}{\partial x_j}\right] & + & \gamma \dfrac{\omega}{k}\left(-\overline{u_i u_j}\dfrac{\partial U_i}{\partial x_j}\right) & - & \beta \omega^2 \end{array}} \tag{2.7}$$

where the closure coefficients are given as:

$\gamma^* = 1,$	$\gamma = 5/9,$	$\beta^* = 9/100,$
$\beta = 3/40,$	$\sigma = 1/2,$	$\sigma^* = 1/2.$

The k-ω model is very similar to the k-ϵ model, in that it has a transport equation for the turbulent kinetic energy. But where the k-ϵ -model operate with a second equation for the dissipation of turbulent kinetic energy ϵ, the k-ω model operate with an equation for the quantity ω. Usually, ω is characterised as the specific dissipation rate, because it is defined as being proportional to ϵ/k. As the dimension of ω is one over time, it can just as well be interpreted as a frequency of the turbulent fluctuations. Saffman (1970) derived a two-equation model for the square of ω, and he characterises ω as a vorticity of the energy-containing eddies. It should be stressed that ω does not necessarily have any direct physical significance; it is just some field variable introduced by analogy to the vorticity in order to calculate the mean velocity and eddy viscosity.

The relation between ϵ used in the k-ϵ model and ω is given as:

$$\epsilon = \beta^* k \omega. \tag{2.8}$$

The model equations (2.7) have the form of transport equations for k and ω. The left hand side of the k and ω equations specifies the rate of change and advection. On the right hand side, the first term is the viscous and turbulent diffusion. The second term is the production of turbulent kinetic energy and specific diffusion. The last term specifies the dissipation of turbulence and dissipation of the dissipation ω (!)

To describe the roughness of a wall the Nikuradse-roughness is commonly applied. For a steady flow that follows the law of the wall (e.g., (Landau and Lifshitz, 1959)):

$$\frac{U(y)}{U_f} = \frac{1}{\kappa} \ln\left(\frac{y}{y_0}\right), \tag{2.9}$$

the constant y_0 was determined by Nikuradse to be $y_0 = k_N/30$ for a rough bed, where k_N was the grain diameter of the sand paper used as roughness. For a sand bottom with loose sand the roughness is enhanced and it is usually set to $k_N = 2.5d_{50}$, where d_{50} is the median of the sediment distribution (Fredsøe and Deigaard, 1992). The boundary conditions for rough walls can be modelled in three ways (Patel and Yoon, 1995):

1. As wall functions where the value of u, v, k and ω is specified some distance from the wall, under the assumption that the law of the wall is valid.

2. The second approach is to include a drag term in the momentum equations to account for the presence of the roughness elements.

3. The third approach is the one followed in the present model, which is to modify the smooth-wall boundary conditions to fit with a known, empirical, solution for rough walls (2.9).

Wilcox has shown that the boundary conditions at the wall reduce to $k = 0$, no-slip for the velocities and a specification of ω on the wall (Wilcox, 1993b). To specify ω he uses the Anzats:

$$\omega = U_f^2 S_R/\nu, \tag{2.10}$$

where U_f is the friction velocity defined as $U_f \equiv \sqrt{\tau_{wall}/\rho}$. The whole system is now closed except for the specification of the constant S_R, which is used to fit the solution to the law of the wall:

$$u^+ = \frac{1}{\kappa} \ln y^+ + B, \tag{2.11}$$

where $u^+ = U/U_f$ and $y^+ = yU_f/\nu$. By generating solutions for different values of S_R and comparing with (2.11), a correlation for B is obtained as:

$$B = 8.4 + \frac{1}{\kappa} \ln \frac{S_R}{100}, \qquad \text{as} \qquad S_R \to 0. \tag{2.12}$$

Now using the Nikuradse determination of B as:

$$B = 8.5 + \frac{1}{\kappa} \ln \frac{1}{k_N^+}; \qquad k_N^+ = U_f k_N / \nu, \tag{2.13}$$

the correlation for S_R as a function of k_N^+ can be determined as:

$$S_R = 100/k_N^+; \qquad k_N^+ \gg 1, \tag{2.14}$$

and thus the system is closed. For small roughness heights, Wilcox claims that the correlation is:

$$S_R \sim (1/k_N^+)^2. \tag{2.15}$$

Putting these two correlations together gives:

$$S_R = \begin{cases} (50/k_N^+)^2, & k_N^+ < 25 \\ 100/k_N^+, & k_N^+ \geq 25 \end{cases} \tag{2.16}$$

Patel and Yoon (1995) shows, that the last relation is valid for a flat wall up to $k_N^+ \approx 4000$. For sake of completeness it should be mentioned that, when performing calculations on a smooth wall, the rough-wall approximation is often used for numerical reasons with a value of $k_N^+ = 5$.

For the velocity components, no-slip conditions are used. This means that there actually exists a viscous boundary layer in the calculations, which again means that the molecular viscosity has to be retained in the equations for k and ω. This is usually not the case in a turbulence model, that operates with wall functions and therefore avoids integrating through the viscous sub-layer. The use of wall-functions is only theoretically justified in an equilibrium boundary layer. Since a major part of the flows treated with the present model involves separation or strong adverse pressure gradients, the use of wall functions is therefore questionable. However, the inclusion of a viscous sub-layer does not necessarily seem the right thing to do either, because the existence of such a layer is usually tied to the concept of a smooth wall. On a rough wall, the size of the individual roughness elements is larger than the size of the viscous sub-layer, and thus the existence of a viscous sub-layer is doubtful. Rather, the friction should be viewed as pressure drag and not as viscous drag. Consequently, the viscous sub-layer generated by the k-ω model is not really "physical", but just a convenient way to perform the parameterisation of the roughness through the parameter S_R.

There is one problem with the k-ω model, though. The results seem to be sensitive to the value of the free stream boundary condition used for ω (Menter, 1993; Wilcox, 1993b). In the problems treated in this Thesis, the boundary condition on the top is a symmetry condition, which makes a specification of the free-stream value of ω superfluous.

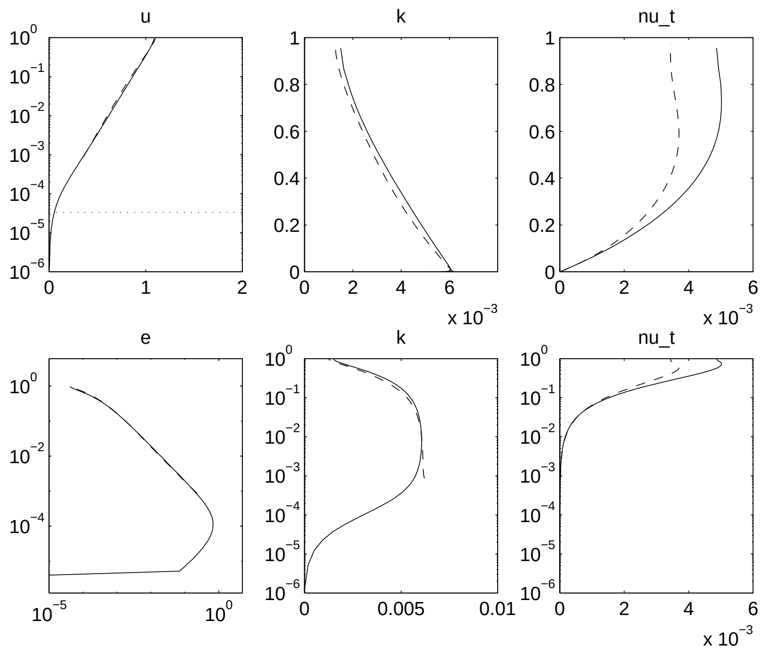

Figure 2.1: Comparison of k-ϵ model (dashed line) and k-ω model (full line) for a rough wall, $k_N/D = 0.001$. The dissipation ϵ in the k-ω model is calculated from (2.8).

Testing the model on a flat rough bed

The first test to make is the boundary layer on a flat wall. Here the model is expected to give the law of the wall with high accuracy.

Figure 2.1 shows a comparison between the k-ω and the k-ϵ models for a run over a rough wall with $k_N/D = 0.001$. There seems to be a good correspondence between the two models, which is to be expected. The k-ω model produces a viscous sub-layer, whereas the k-ϵ model relies on wall functions. The dotted line in the upper left figure is drawn at $y = k_N/30$, which is the level of the theoretical wall, where the horizontal velocity is supposed to vanish if the logarithmic region is extrapolated down.

To check if the solution is independent of the value of Re_D, four runs was made with Re_D between $5 \cdot 10^4$ and $5 \cdot 10^6$, for $k_N/D = 0.005$ (table 2.1). The resultant velocity profiles are seen in figure 2.2. It is seen how the largest viscous sub-layer is found for the lower Re_D. In table 2.1 the resultant friction-velocity is seen, and the only calculation which differs from the others is the one for the lower Re_D. When calculating k_N^+, it is also seen that the wall in this calculation is to be considered as being in the transition-to-roughness regime.

Table 2.1: The parameters used for the runs with different Re_D. The last column corresponds to the ratio between the height of the smooth-wall viscous boundary layer to the roughness.

Re_D	U_f	k_N^+
$5 \cdot 10^4$	0.047	12
$5 \cdot 10^5$	0.052	130
$1 \cdot 10^6$	0.052	260
$5 \cdot 10^6$	0.052	1300

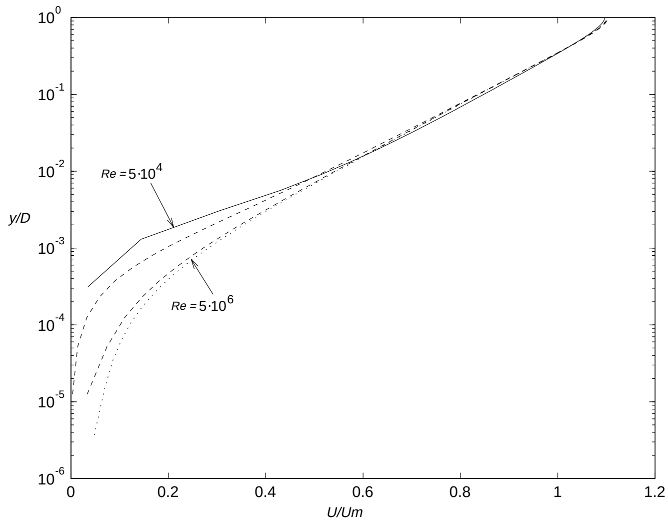

Figure 2.2: Velocity profiles for four runs on a wall with $k_N/D = 0.005$, and Reynolds number ranging from $5 \times\ 10^4$ (upper, solid line) to $5 \times\ 10^6$ (lower, dotted line).

Testing in a oscillatory boundary layer

The classical turbulence models, like the k-ϵ and k-ω models, are developed for flows where the turbulence is supposed to be in local equilibrium. It is therefore not obvious that they will perform well in non-equilibrium situations. A simple non-equilibrium situation, which is essential for the present study, is the turbulent oscillatory boundary layer over a flat bed.

The test was made with a period $T = 9.72$ s, $a = 3.1$ m, $Re_D = 4.0\times\ 10^5$ and the Nikuradse roughness $k_N = 0.84 \times\ 10^{-3}$ m. These parameters correspond to run no. 13 in the experimental work of Jensen (1989).

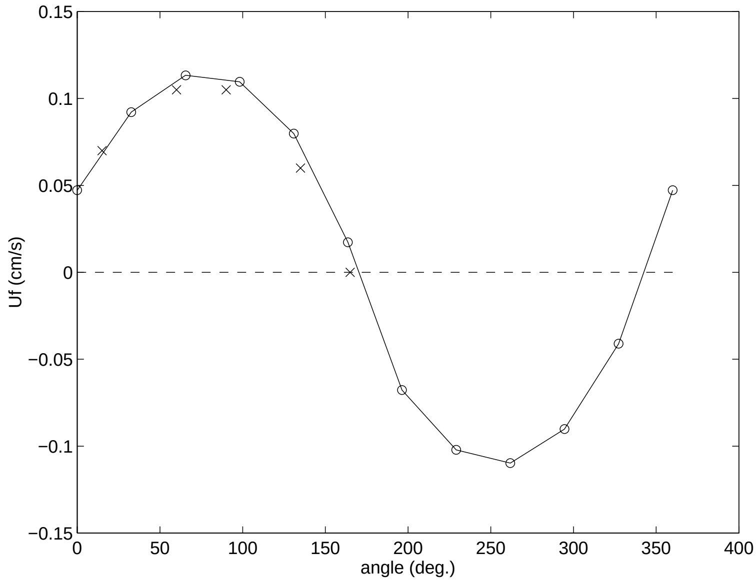

Figure 2.3: Comparison between friction-velocity obtained by k-ω and by the measurements of B.L. Jensen, run 13 (Jensen, 1989).

In figure 2.3 a comparison is seen between the friction-velocity obtained by the run, and a few of the measured points. A quite good agreement is achieved.

2.2 The boundary conditions

The set of equations to be solved is the RNS equations (2.4) for the horizontal and vertical velocities U and V and the pressure P. The turbulence is resolved by the equations for k and ω (2.7).

On the sides of the domain periodic conditions are used, so that the calculation is in effect made on a infinite train of ripples (figure 2.4). At the top symmetry conditions is used, i.e.

$$\frac{\partial}{\partial y} = 0 \quad \text{and} \quad V = 0 \quad \text{at} \quad y = D. \tag{2.17}$$

The boundary conditions on the bed is $U = V = k = 0$ and ω given by (2.10) and (2.16)

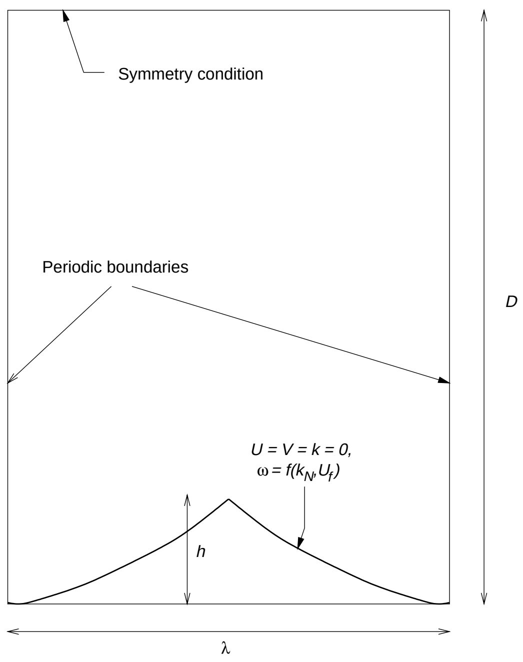

Figure 2.4: The computational domain with boundary conditions and important quantities.

2.3 The numerical solver

The governing equations are discretized using the Finite Volume method, for details see Patankar (1980) or Versteeg and Malalasekera (1995). The equations are written in general curvilinear coordinates to allow the grid to fit smoothly to the boundaries (see Tjerry (1995) for details).

The main difficulty solving the Navier-Stokes equations in the incompressible case is that specific measures have to be taken to find the pressure, as there is no explicit equation for the pressure. To find the pressure the PISO algorithm (Patankar, 1980) is used.

It was found that high order discretization in space was needed to avoid numerical diffusion. The discretization is the so-called ISNAS scheme of Zijlema (1996), which is third order accurate in space and monotonicity preserving.

The discretization in time is implicit, except the advective terms which are semi-implicit.

The grid is made using a hyperbolic grid generator, with a concentration of points near the bed. In the morphological calculations a simple transfinite interpolation has been used to create a grid.

To drive the waves and the current through the domain an extra force

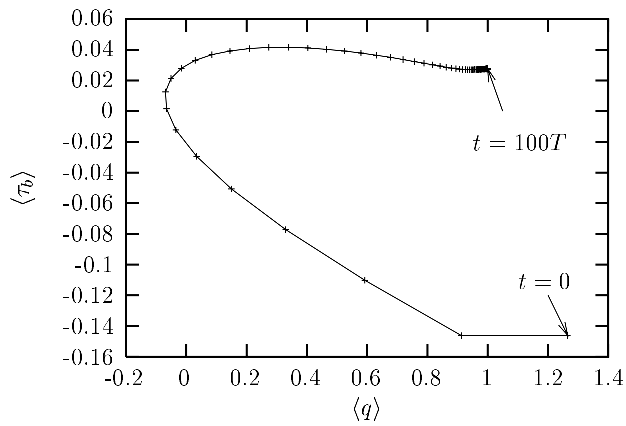

Figure 2.5: An example of the convergence of the flow over a ripple using PID-control. The flow is converging towards a flux of 1.0 during 100 periods.

term is added to the equations. This term is oscillating for the wave, and a constant for the current. The current part deserves some extra attention. Usually a specific average current is wanted, but the force which is needed to drive that current is unknown. The process of iteration to find the correct current is accomplished using PID-control.

PID control

The basic idea is that three parameters are available when the flux q is searched for: The difference between the calculated and the wanted flux, $P = q' - q$ ('P' is for proportional), the integrated value of the flux $I = \int_0^t (q' - q)\,dt$ ('I' is for integral) and the gradient of the flux $D = \partial q'/\partial t$ ('D' for derivative). In steady current t is the time and q' is the flux, in waves t is the number of periods and q' is the flux averaged over one period. All three parameters P, I and D, have to vanish when the solution is converged. Thus the change in the slope s can be found as:

$$s = -\sigma \left(\sigma_P (q' - q) + \sigma_D \frac{\partial q'}{\partial t} + \sigma_I \int_0^t q' - q\,dt \right), \qquad (2.18)$$

where σ is the general relaxation factor and σ_P, σ_D and σ_I are relaxation factors for P, D and I, respectively. This is as simple as it looks and very easy to implement. An example of a flow over a ripple converged using PID-control is seen in figure 2.5.

The rôle of each of the relaxation factors is as follows:

Relaxation parameter	Rise time	Overshoot	Settling time
σ_P	Decreases	Increases	No change
σ_D	No change	Decreases	Decreases
σ_I	Decreases	Increases	Increases

The table can be used to tune the relaxation factors. If there is a too large overshoot, then σ_D should be increased and so on. These are just general guidelines; if for example σ_D is too large, the system will become unstable.

The values of the relaxation parameters used in the following are:

$$\sigma = 0.1 \quad \sigma_P = 1.0 \quad \sigma_D = 3.0 \quad \sigma_I = 0.05$$

For some cases the settling time can be decreased if the I-control is completely disabled and σ_D is made somewhat larger.

2.4 Modelling the sediment transport

The transport of sediment is usually split into two partitions: *bed load* and *suspended load.*

The bed load is a thin layer of sand rolling and sliding on the surface of the bed. In water the density of the sand and the water is of the same order of magnitude, and thus the process of saltation is not present, as it is in air where the sand is much heavier than the air. The bed load is therefore in constant contact with the bed and is a function of the local shear stress and the local slope only. In the model the bed load is described as a volume flux of sediment.

Due to turbulent fluctuations the sediment is lifted out of the bed load layer and into suspension. Here the sediment is advected by the flow, diffused due to turbulent "diffusion" and is drifting towards the bed due to gravity. The suspension is described as a field variable c which is the concentration of sediment. This is modelled by a transport-diffusion equation:

$$\boxed{\frac{Dc}{Dt} = w_s \frac{\partial c}{\partial y} + \nabla(\epsilon_s \nabla c),} \tag{2.19}$$

where w_s is the settling velocity and ϵ_s is the diffusivity of the suspended sediment, which is usually assumed to be equal to ν_T. This formulation has to be supplied with a boundary condition at the bed, which will be derived in together with the bed load.

The most important quantity determining the sediment transport is the local shear stress on the bed, τ_b. If a single grain is considered the shear stress acts as a destabilising force on the grain due to both lift and drag:

$$F_{destab} \sim d^2 \tau_b. \tag{2.20}$$

Counter to the destabilising force of the shear stress is the stabilising force due to gravity:

$$F_{stab} \propto \rho g(s-1)d^3. \tag{2.21}$$

Forming the ratio between the destabilising and the stabilising forces gives a non-dimensional shear stress, the Shields parameter:

$$\theta \equiv \frac{\tau_b}{\rho g(s-1)d} \sim \frac{F_{destab}}{F_{stab}} \tag{2.22}$$

which will be encountered numerous times throughout this Thesis.

The Shields parameter directly determines the bed load and is indirectly responsible for the amount of the suspension through the boundary condition at the bed.

In the following the relations for the bed load and the bed boundary condition for suspended transport will be derived through a mixture of fundamental principles, physical reasoning, and empirical relations.

2.4.1 The bed load

The flux of sediment q_b is the volume transported per time and per width through a cross section in the bed. The flux can be found if the velocity of a single grain in the bed load layer is known together with the number of grains in motion.

The velocity of a single grain is found by considering the driving and stabilising forces on a single grain in motion (figure 2.6). The main driving force is the drag on the grain, which is modelled using the Morison equation (i.e. Sarpkaya and Isaacson (1981)):

$$F_D = \frac{1}{2}\rho C_D \frac{\pi}{4} d^2 |U_r| U_r, \tag{2.23}$$

ρ is the density of water, C_D is the drag-coefficient, and U_r is the relative velocity of the water affecting the grains. The relative velocity is $U_r = U|_{y=d} - U_b$, where U_b is the velocity of the grain. For convenience later on $U|_{y=d}$ is written as $U|_{y=d} = \alpha U_f$. Assuming a logarithmic velocity profile close to the bed (2.9) $\alpha \simeq 10$. The numerical sign around U_r is important in order to keep the right sign of the drag-force.

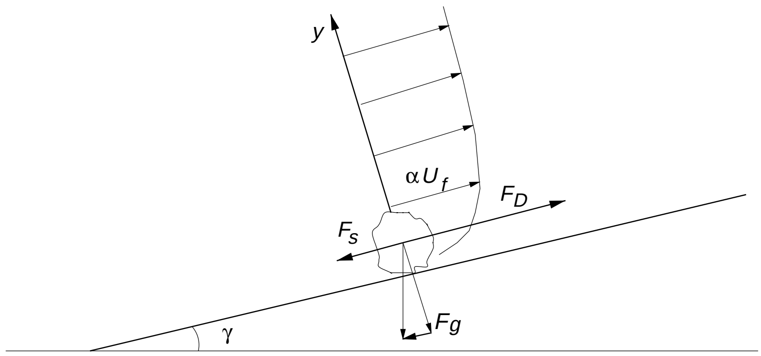

Figure 2.6: The forces acting on a single grain on a sloping bed

The other component of the driving force arises from the gravity, and has the form:

$$F_g = -W \sin\gamma, \tag{2.24}$$

where W is the gravitational force: $W = \rho g(s-1)d^3\pi/6$. In the example in figure 2.6 this force actually acts as a retarding force.

The stabilising force is the friction created by the component of the gravity normal to the bed:

$$F_s = -\mu_D W|\cos\gamma|\sigma, \tag{2.25}$$

where μ_D is the dynamic friction coefficient, and σ is the sign of the direction of the bed load.

It is now possible to make a balance of forces:

$$F_D + F_g + F_s = 0, \tag{2.26}$$

and the velocity of the grains can be expressed as:

$$U_b = \alpha U_f - s\alpha\sqrt{\theta_c}\sqrt{\sigma\cos\gamma + \sin\gamma/\mu_D}\sqrt{(s-1)gd}, \tag{2.27}$$

where θ_c is the critical Shields parameter for a flat bed:

$$\theta_c = \frac{4\mu_D}{3C_D\alpha^2}. \tag{2.28}$$

From measurements (the so-called Shields diagram, see e.g. (Fredsøe and Deigaard, 1992)) it is found for $Re = U_f d/\nu > 5$ that θ_c is independent on Re and $\theta_c \approx 0.05$. If the velocity of the grains is set to zero, the criterion for the threshold of motion on an arbitrarily sloping bed can be found:

$$\theta_{c\gamma} = \theta_c\left(\sigma\cos\gamma + \frac{\sin\gamma}{\mu_D}\right), \tag{2.29}$$

where θ_c is defined similar to the the definition of θ in equation 2.22. Substitution of θ_c into equation 2.27 gives:

$$\frac{U_b}{U_f} = \alpha \left(1 - \sqrt{\left|\frac{\theta_{c\gamma}}{\theta}\right|}\right). \tag{2.30}$$

Now that the velocity of the grains is calculated, it still remains to determine the number of grains per area n in the bed load layer, before the bed load can be calculated.

The force balance on a small volume of the bed load layer is written as:

$$\tau_b = \tau_g + \tau_{c\gamma}. \tag{2.31}$$

The interpretation of the terms is as follows: The parameter τ_b is the shear stress on the top of the bed load layer. It is assumed that this is equal to the shear stress on a fixed flat bed. τ_G is the stress arising from the inter-granular collisions, giving rise to "grain-stresses" (Kovacs and Parker, 1994; Fredsøe and Deigaard, 1992). This is modelled as: $\tau_G = nW\mu_D$. Finally, the parameter τ_B is assumed to be equal to the critical shear stress on the bottom $\tau_{c\gamma}$. It is thus assumed that the inter-granular stress absorbs all the stress, except the critical stress. This is called the "Bagnold hypothesis" (Kovacs and Parker, 1994). Making equation 2.31 non-dimensional by dividing with $\rho(s-1)gd$ the number of grains in motion is found as:

$$n = \frac{6}{\pi d^2 \mu_D}(\theta - \theta_{c\gamma}), \tag{2.32}$$

where $\theta_{c\gamma}$ is defined in (2.29). If $\theta < \theta_{c\gamma}$, then no grains are in motion and $n = 0$.

Now, finally, the bed load can be calculated. The bed load, q_b is defined as the flux of sand per width and is made non-dimensional as $\phi_b = q_b/\sqrt{(s-1)gd^3}$. This then gives:

$$\begin{aligned} \phi_b(\theta, \gamma) &= n\frac{\pi}{6} d^3 U_b \sqrt{(s-1)gd^3} && (2.33) \\ &= \frac{\alpha}{\mu_D}(\theta - \theta_{c\gamma})(\sqrt{|\theta|} - \sqrt{|\theta_{c\gamma}|}). && (2.34) \end{aligned}$$

Again this is only valid for $\theta > \theta_{c\gamma}$. In the flat-bed limit this equation is very similar to the classical empirical relation by Meyer-Peter and Müller from 1948 :

$$\phi_b(\theta) = 8(\theta - \theta_c)^{1.5}. \tag{2.35}$$

Fredsøe proposed to add a simple linear gravity correction to the Meyer-Peter formula, valid for small γ (Fredsøe, 1974):

$$\phi_b(\theta, \gamma) = 8(\theta - \theta_c - \beta \frac{\partial h}{\partial x})^{1.5} \tag{2.36}$$

with $\beta \simeq 0.1$. Only very few measurements exist of the bed load on a sloping bed. In a recent study Damgaard, Whitehouse, and Soulsby (1996) suggested that the Meyer-Peter formula should be corrected with the empirical factor f_{slope}:

$$f_{slope} = 1 + 0.8 \left(\frac{\theta_c}{\theta}\right)^{0.2} \left(1 - \frac{\theta_{c\gamma}}{\theta_c}\right)^{1.5+\theta/\theta_c}, \tag{2.37}$$

such that

$$\phi_b(\theta, \gamma) = 8 f_{slope}(\theta - \theta_c - 0.1 \frac{\partial h}{\partial x})^{1.5}. \tag{2.38}$$

This formula f_{slope} is not the most elegant fit, i.e., it is not well defined for all positive slopes.

2.4.2 Corrections to the bed load and the bed BC for suspended transport

Engelund and Fredsøe have elaborated on the bed load transport derivation presented in the previous section, and proposed some empirical corrections for high Shields parameters (Engelund and Fredsøe, 1976). This also leads to a derivation of a bed boundary condition for the suspended transport (Fredsøe and Deigaard, 1992).

First of all it was found that the velocity of the grains fitted the measurement better if the expression:

$$\boxed{\frac{U_b}{U_f} = \alpha \left(1 - 0.7\sqrt{\left|\frac{\theta_{c\gamma}}{\theta}\right|}\right)} \tag{2.39}$$

was used instead of equ. (2.27). This is a very small correction to the bed load.

A more important correction is to extend the formula to high shear stress rates, where it is well known that the Meyer-Peter formula overestimates the bed load. The argument goes that there can only be one layer of grains in motion in the bed load layer. Further layers of grains belong to the suspended load. This sets an upper limit on n such that $n \leq d^{-2}$. This can be realized adopting the expression:

$$\boxed{n = \frac{1}{d^2}\left[1 + \left(\frac{\frac{\pi}{6}\mu_d}{\theta' - \theta_c}\right)^4\right]^{-0.25}}. \tag{2.40}$$

This means that there will be an excess stress in equ. (2.31) which will be attributed to stresses in the upper part of the moving layer; suspended transport. The stress in a thick slurry of sediment and water was measured by Bagnold (1954) to be:

$$\tau_G = 0.013\rho s(\lambda_f d)^2 \left(\frac{\partial u}{\partial z}\right)^2, \tag{2.41}$$

where d/λ_f is the mean free path of the particles, which is related to the concentration of sediment as:

$$c = c_0 \left(1 + \frac{1}{\lambda_f}\right)^{-3}, \quad c_0 = 0.65. \tag{2.42}$$

A crude approximation is to assume that the velocity gradient in the lower layer is logarithmic and unaffected by the presence of the sediment, so that it follows the law of the wall, which in differential form reads:

$$\frac{\partial U}{\partial y} = \frac{U_f}{\kappa y}, \tag{2.43}$$

which is inserted in (2.41).

The balance in the bed load layer now reads:

$$\tau_b = \tau_g + \tau_G + \tau_{c\gamma}. \tag{2.44}$$

Inserting the stresses and dividing by $\rho g(s-1)d$ the mean free path of the sediment can be found to be:

$$\lambda_f^2 = \frac{\kappa^2 y^2}{0.013\rho s d^2\theta}\left(\theta - \theta_{c\gamma} - n\frac{\pi}{6}d^2\mu_D\right). \tag{2.45}$$

The bed boundary condition for the suspended sediment is usually taken at $y = 2d$ leading to:

$$\lambda_f^2|_{y=2d} = \frac{4\kappa^2}{0.013\rho s\theta}\left(\theta - \theta_{c\gamma} - n\frac{\pi}{6}d^2\mu_D\right). \tag{2.46}$$

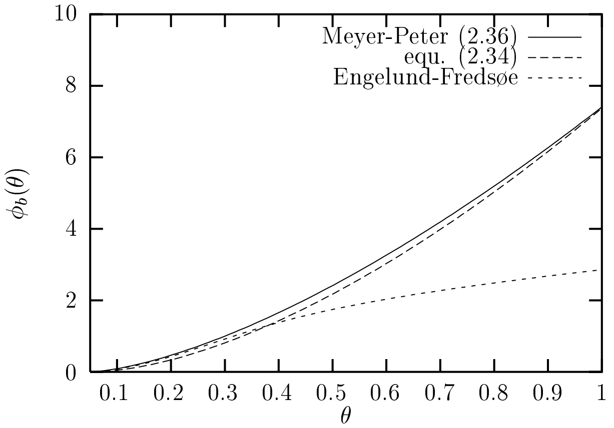

Figure 2.7: The bed load as calculated by different formulas on a level bed. The parameters used are: $\alpha = 6.5$ and $\mu_D = 0.65$.

Using equ. (2.40) to find n and equ. (2.42] to find the concentration from equ. (2.46), a boundary condition for the suspended sediment can be found as:

$$\boxed{c_b(\theta, \gamma)|_{y=2d}.} \tag{2.47}$$

The bed load is again found as before equ. (2.34), but now using the corrected expression for U_b equ .(2.39) and n equ .(2.40).

The different bed load formulas are compared in figure 2.7 for a level bed. For small and medium shear stress rates the formulas give almost identical results, but for higher shear stress rates ($\theta > 0.4$) the correction in the Engelund-Fredsøe formula sets in and limits the bed load.

The different formulas are also quite similar when the bed load at different bed slopes are compared (figure 2.8). For low shear stresses the formula derived in (2.34) fits the empirical f_{slope} correction best, while for high shear stress rates the Engelund Fredsøe formula fits better. The empirical f_{slope}-formula has a strong correction close to the angle of repose, showing that small avalanches are already setting in. This shows that the dynamic angle of repose is smaller than the static angle of repose for flow down slope.

2.4.3 The final sediment transport model

Now a complete formulation of the bed load and the suspended load can be constructed.

The bed load is described using the Engelund-Fredsøe formulation equ . (2.34), (2.39) and (2.40). The sloping bed is taken into account through

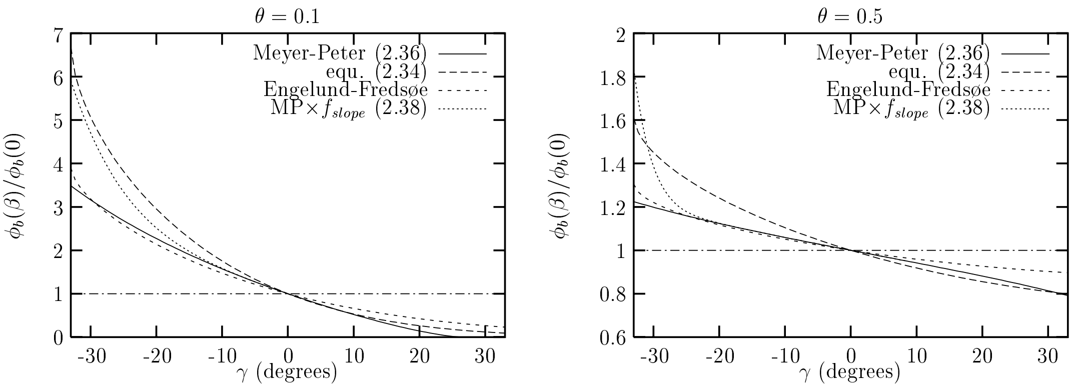

Figure 2.8: The bed load calculated for different slopes and at small shear stress (left) and high shear stress (right). The bed load have been divided with the bed load at a flat bed to make a facilitate an easier comparison of the slope effect alone.

the critical shear stress equ. (2.29), with a strong down-slope flux if the bed slope is larger than the angle of repose.

The suspended sediment is described using the transport equation (2.19), supplied by the bed boundary condition equ. (2.40), (2.42) and (2.46).

This formulation has the advantage of being a consistent description of both the bed load and the bed boundary condition for the suspended sediment.

The most important shortcoming of the model is that the bed load and the bed boundary condition are functions of the *average* shear stress only. The turbulent fluctuations, represented by k, are ignored. This is especially bad for the bed boundary condition for suspended sediment. An example where this boundary condition fails is at a reattachment point. Here the average shear stress is zero, but there is a lot of motion giving rise to large values of k. In an experimental situation (i.e. the reattachment point behind a dune) large clouds of sediment are thrown into suspension exactly here. One way to take this into account would be to derive a bed boundary condition involving not only the shear stress but also the turbulent kinetic energy.

Although far from perfect the present sediment transport formulation captures the most important aspects of the sediment transport. The deficiencies it has are not believed to bar an understanding of the basic mechanisms behind the dynamics of ripples.

2.5 Morphological calculations

When the flow and the sediment transport have been calculated it is, at least in principle, simple to make a morphological calculation where the bed profile is continuously changed. The change in the bed profile can be found using the continuity equation for the sediment

$$\boxed{\frac{\partial h(x,t)}{\partial t} = -\frac{1}{1-n}\frac{\partial q_t(x,t)}{\partial x},} \tag{2.48}$$

where n ($= 0.4$) is the porosity of the bed and q_t is the total sediment flux through a cross-section

$$q_t(x,t) = q_b(x,t) + \int_{h(x,t)}^{D} q_s(x,y,t)dy. \tag{2.49}$$

The continuity equation is discretized using the QUICK scheme of Leonard (1979) which is third order accurate in space. To avoid numerical instabilities the sediment transport is smoothed using an ordinary running average. In principle the bed can be updated every time step using the continuity equation, but in practice this requires that acceleration terms due to the moving grid are incorporated in the governing equations (e.g. Mayer, Garapon, and Sørensen (1998)). Instead a more pragmatic approach has been adopted – the bed is only updated every tenth time step. This way the solver is "kicked" every time the bed and the grid are updated, but after ten time steps it has recovered completely. Usually 3000 time steps per period have been employed for morphological calculations.

One major, and basically unresolved, problem with the morphological calculations is the appearance of instabilities manifested as small steady-current ripples with a wave-length of 5–10 grid points. These might be caused by numerical instabilities, but these often manifest themselves as oscillations with a wave-length of only two grid points. The small ripples might also be semi-physical, that is, they are solutions to the quite complicated flow- and sediment model. As these ripples are not present in Nature, they represent a shortcoming of the model.

The morphological calculations of ripples are very fortunate in so that they are dominated by avalanches down the sides of the ripples which sweep out the small ripples. Thus no special measures are taken to dampen these small ripples.

In the morphological calculation the angle of repose will often be encountered, so the bed load formula need to be able to handle this situation. A very pragmatic solution has been employed: when the angle of the bed slope is equal to or larger than the angle of repose, a strong bed load flux is made down-slope, regardless of the shear stress.

2.6 Grid independence of the solutions

One of the more boring aspects of numerical work is the need to test whether the results are insensitive to the grid spacing used. Nevertheless it has to been done. This and other numerical aspects are the topic of this section. The not-so-technically-interested reader is encouraged to skip this section.

2.6.1 Grid sensitivity of the flow

All the tests have been made around a "standard test case". The Reynolds number is $Re_a = 3 \cdot 10^5$, which ensures that even a flat bed has a fully turbulent developed rough boundary layer. The length of the ripple is $\lambda/a = 1.2$, and the steepness is $h/\lambda = 0.20$, both are around the expected equilibrium shape.

There are several parameters that affect the quality of the grid. The most notable is the number of points in the x and y directions, N and M correspondingly. It was found that the flow was quite sensitive to the density of points just around the crest, so a stretched grid was used, concentrating the points around the crest. The important parameter is then $\Delta x_{crest}/a$ and not N, where Δx_{crest} is the grid spacing at the crest. In the vertical direction another important point is how close the points are spaced near the bed. With the k-ω model it is necessary that the viscous sub-layer is resolved, and therefore some points are needed here. The important parameter is then the distance from the bed to the first grid cell $y_0^+ = y_0 U_f/\nu$, which should not be larger than 2 (Wilcox, 1993b). The friction velocity is not known beforehand, so the value of U_f used is the one from a flat bed, found using a constant friction factor. Finally there is the depth of the flow. This is more a physical than a numerical parameter, but a criterion for the simulations to be independent on the depth is needed.

The four parameters to be examined are then: $\Delta x_{crest}/a$, M, y_0^+ and D/a.

In figure 2.9 the friction velocity averaged over one half period are shown for grids with different values of $\Delta x_{crest}/a$ and N. There are not any major differences, but it seems as if a grid with $\Delta x_{crest}/a < 0.012$ results in some minor instabilities near the crest. Thus $\Delta x_{crest}/a$ should be at maximum 0.012 and 40 points in the horizontal direction should be enough.

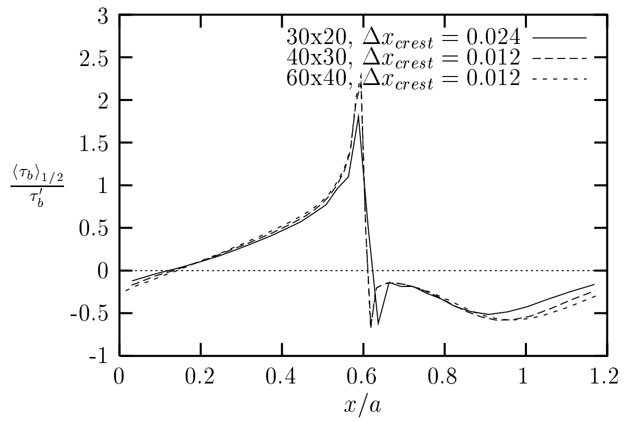

Figure 2.9: The friction velocity averaged over one half period for different grids. The number of iterations per period are between 800 and 2000. $y_0^+ = 0.80$.

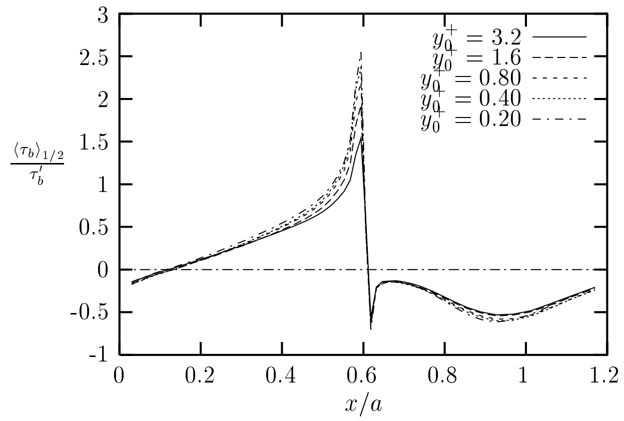

Figure 2.10: The friction velocity averaged over one half period, for different values of y_0^+ and N. $\Delta x_{crest}/a = 0.012$.

The influence of changing the value of y_0^+ is mostly felt in areas where the shear stress is large, i.e., on the "wind"-side of the crest (figure 2.10). For $y_0^+ \leq 0.40$ the solution seem independent on y_0^+.

If the wave boundary layer created by the ripples is thin compared to the depth of the flow, it is also expected that the flow over the ripples are insensitive to the depth of the water above them. As one does not want to waste grid points resolving the potential flow far above the ripples, one must know how shallow a depth can be used without affecting the flow around

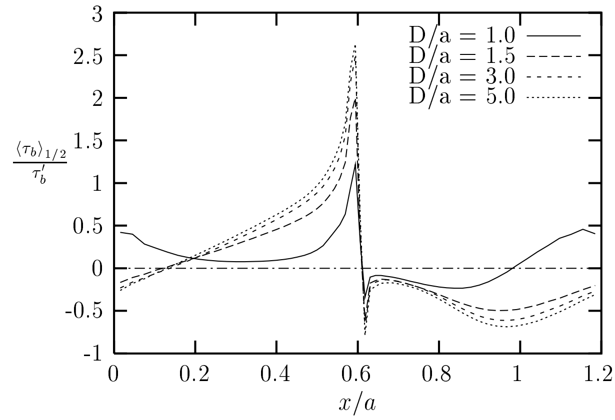

Figure 2.11: The friction velocity averaged over one half period, for different values of the depth D/a. The grid is 60×40, $y_0^+ = 0.40$ and $\Delta x_{crest}/a = 0.012$.

the ripples. In figure 2.11 the flow is calculated while varying the depth. It is seen that a small depth $D/a < 1.0$ clearly affects the flow with a strong inhibition of the separation bubble.

A summation of the results from the tests with various grids is as follows: The grid size should be 40×30, with the spacing at the crest $\Delta x_{crest}/a \leq 0.012$ and $y_0^+ \leq 0.40$. For the simulation to be independent of the depth $D \geq 3.0a$. A grid satisfying the above minimal requirements is shown in figure 2.12.

2.6.2 Grid sensitivity for suspended transport

In figure 2.13 the transport of suspended sediment with three different grid sizes is shown. The settling velocity is $w_s/U_m = 0.065$ which is quite small, resulting in large amounts of suspension. For all three grids the flow is the same, as could be expected from the grid sensitivity tests in section 2.6. The transport averaged over the whole period is much smaller than the transport averaged over a half period. The period-average can be performed as the average of the half-period averaged transport in the first and the second half of the period. Thus the period average is the difference of two large numbers, which have to converge to a small number. This is what is numerically called a *stiff* problem, and it means that it is very hard to converge the period averaged sediment transport, often around 50 periods are needed.

A sad fact is seen from the figure, namely that grid convergence is not completely achieved, even with grids with up to 100 vertical points. The difference between the grid with 40 vertical points and the grid with 100

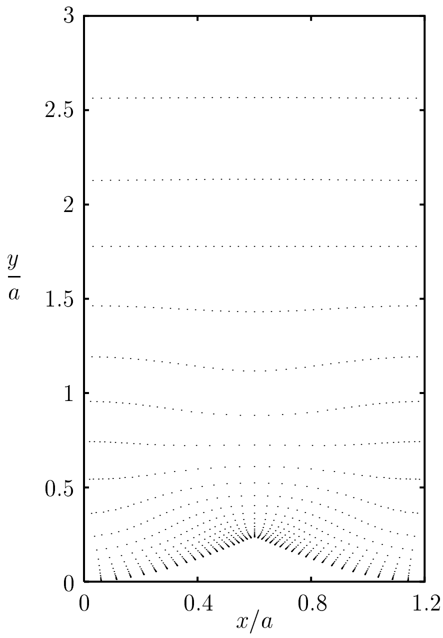

Figure 2.12: A grid created using a hyperbolic grid generator above a rippled bed with steepness $h/\lambda = 0.20$. The grid satisfies the minimal requirements for the flow to be independent on the grid.

vertical points is around 10 %. The cause of the problems with the suspended transport is the very strong gradients in the suspended transport near the bed. To resolve these gradients correctly an extremely fine grid is needed. The use of finer grids takes up more computer time, both because of the larger number of cells, but also because the time-step has to be reduced when the grid size is reduced. This makes the use of a grid which resolves the suspended transport correctly prohibitive in this model.

It is always annoying to have a result without complete grid insensitivity, but in this case the uncertainty has to be weighted against the uncertainty inherent in the modelling of the suspended sediment. As already pointed out in section 2.4.2, there are already some weak points in the modelling of the suspended sediment. It is reasonable to assume that these uncertainties overshadow the grid problem. Still the modelling of the suspended transport gives sensible results qualitatively.

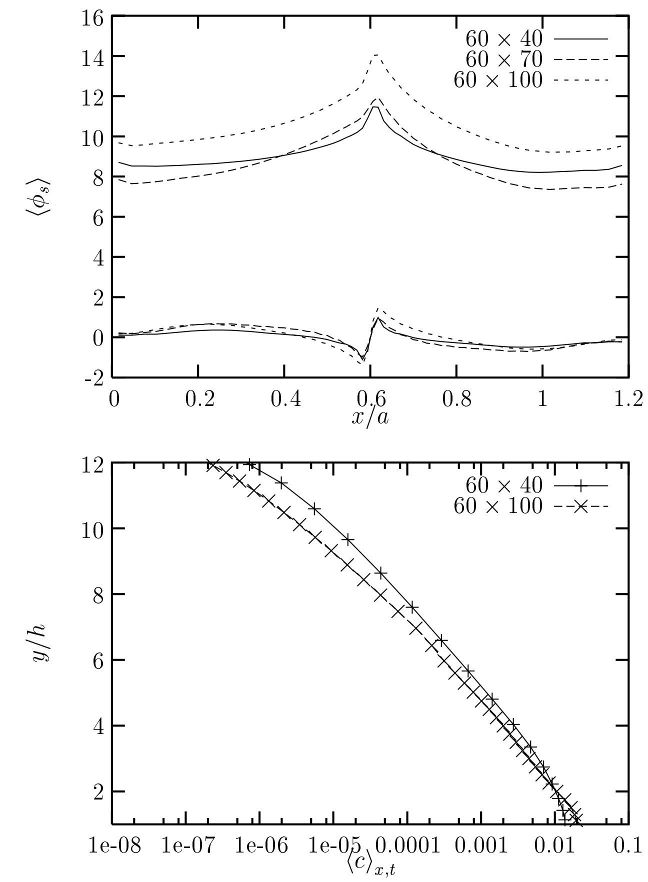

Figure 2.13: The transport of suspended sediment over ripples using different grids. On the top figure is shown the period-averaged flux of sediment ($\langle \phi_s \rangle_t$, lower lines) and the half-period-averaged flux of sediment ($\langle \phi_s \rangle_{1/2}$, upper lines). The lower figure shows the concentration of suspended sediment averaged over one wave period, for two different grids ($\lambda/a = 1.2,\ h/\lambda = 0.2,\ \theta' = 0.15,\ w_s/U_m = 0.065$).

Chapter 3

Initiation of ripples

This chapter is devoted to the study the formation ripples from an initially flat bed. For the coastal engineer this problem is only of academic interest, because a flat bed is rarely found in Nature. For the understanding of the ripples as a pattern-forming system the way the bifurcation from a flat bed to a rippled bed takes place is important. Three different mechanisms for the creation of ripples will be described. From a flat bed the rolling grain ripples appear as a transient phenomenon, which eventually grow into vortex ripples. Two conceptually different explanations of the creation of rolling grain ripples from a flat bed will be explored. The first model is based on the motion and amalgamation of single grains (section 3.2). This model is essentially a granular theory. The other mechanism is a theory where the selected wave length is found from a linear stability analysis of the Stokes boundary layer flow (section 3.3). This theory is then a fluid dynamics theory. Finally vortex ripples can be created via nucleation (section 3.4). This is where an initial finite perturbation on the flat bed nucleates other ripples. An example of the formation stage of ripples is seen in figure 3.1.

3.1 The rolling grain ripples

The ripples first appearing on a flat bed, when the Shields parameter is close to the critical value, have been called *rolling grain ripples* by Bagnold (1946). At this stage the grains which are pulled loose from the bed, start rolling back and forth on the top of the flat bed. After a while they collect together and form small triangular ridges: rolling grain ripples. Viewed from above the rolling grain ripples form long and very regular bands.

According to Bagnold (1946) the rolling grain ripples are stable if the Shields parameter is less that two times the critical Shields parameter. If

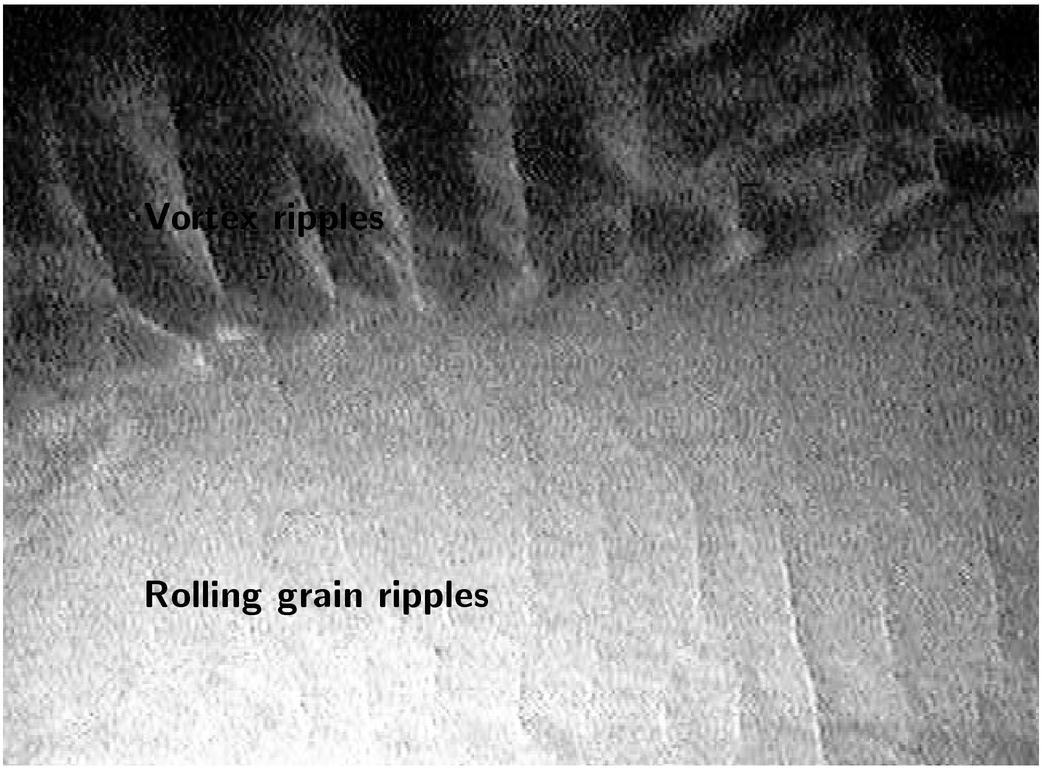

Figure 3.1: An example of a flat bed with rolling grain ripples and vortex ripples invading from the top.

the Shields parameter becomes larger than this, the lee vortex becomes so strong that it is able to initiate grain motion in the space between two ripples and thus scoop grains toward the crest of the ripples. In this case the ripple growth set in and will continue until the equilibrium vortex ripples are reached. However, stable rolling grain ripples have not been found in the recent high-quality experiments of Scherer *et al.* (1999) and Stegner & Wesfried (1998). It seems as if the rolling grain ripples are always developing into vortex ripples, but the transient can be very long if the grain motion is close to threshold. Probably Bagnold had problems with invasion of ripples via nucleation from the boundaries, and this invasion happened faster than the rolling grain ripple could evolve into vortex ripples on their own accord.

Some attempts have been made to estimate the length of the rolling grain ripples. The most complete theory is due to Blondeaux, Vittori and Foti ((Blondeaux, 1990; Vittori and Blondeaux, 1990; Vittori and Blondeaux, 1991; Foti and Blondeux, 1995b; Foti and Blondeux, 1995a; Blondeaux *et al.*, 1996)). This is a linear stability analysis of the flow, coupled to the sediment motion. Before presenting the linear stability analysis, a simple model based on the motion of the individual grains is developed.

3.2 A simple granular model of rolling grain ripples

In Bagnolds original classification of the rolling grain ripples from 1946 , he describes how they are created by grains moving back and forth over the bed:

> Though initially distributed at random, the rolling grains become organised as time goes on, and tend to come to rest in parallel transverse zones. More grains reach these zones than leave them, so there is a progressive congregation of grains in them, and the zones soon become little wavy ridges a few grains high, whose crests sway from lee side to lee side during successive stroke reversals. Each lee side becomes a miniature scree at the angle of repose. As the ridge grows it shelters from the water action a wider and wider strip of flat surface on its successive lee sides; and when the sheltered area extends as far as the next ridge no further grain movement can take place anywhere but on the ridge itself. Hence, since the ridges can now collect no more grains, they cease to grow, and the arrangement becomes stable. The repetition distance is evidently the width of the flow shadow of the ridge, and depends on its height.

This description of grains rolling back and forth, merging to create ridges, and attracting nearby grains due to a shadow zone has been put into a simple mathematical model.

3.2.1 Formulation of the model

The model consists of N particles rolling on top of a rough, solid surface. Each particle has a position x_i and an area. As the model is one-dimensional the areas is referred to as the mass m_i of the particle. As the particles merge, they become small rolling-grain ripples with a height $h_i = \sqrt{m_i}$.

The flow moves back and forth above the bed and makes the particles move on the bed. Behind each particle/ripple there is a shadow zone, due to the creation of a separation bubble. The shadow zone is the area behind the particle where the absolute value of the shear stress is smaller than it

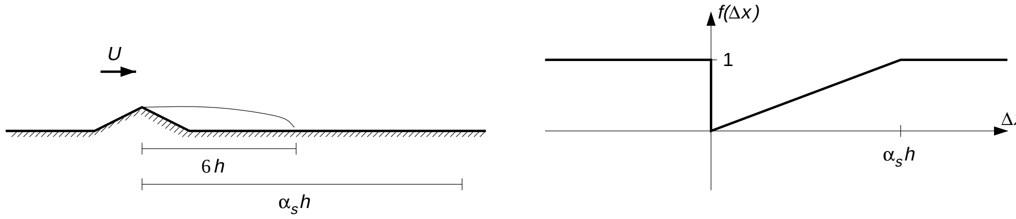

Figure 3.2: Each particle has a shadow zone extending a length $\alpha_s h_i$ in the upstream direction (left). Right: The function f is used to describe how a particle is slowed down when it enters the shadow zone of another particle. Δx is the distance between two neighbouring ripples. The example shown here is a a time in the wave period when the flow is from the left to the right.

would be on a flat bed. The length of the shadow zone is therefore larger than the length of the separation bubble. If the shadow zone is much smaller than the amplitude of water motion, the flow in the lee side of the ripple can be assumed to have sufficient time to become fully developed. The fully developed flow is similar to that past a backward facing step in steady flow, which has been extensively studied (see e.g. Tjerry (1995)). In that case the separation bubble itself has approximately a length of six times the height of the step, but the shadow zone will be longer than that. Approximately 16 step heights away from the step there is a maximum in the shear stress on the bed, which sets the maximum extent of the shadow zone. As a first assumption the shadow zone is assumed to have a length which is proportional to the height of the particle: $l_{s.i} = \alpha_s h_i$. If a particle enters the shadow zone of another particle, it is slowed down according to the distance between the particles. This means that the actual velocity of a grain is $u_i f(\Delta x)$ where Δx is the distance between the grain and the nearest neighbour downstream, and f is the function determining the nature of the slowing of the motion of the particle. A simple linear function is used, as shown in figure 3.2. The exact form of the function f is not crucial, the important parameter is the extent of the shadow zone α_s.

When two particles collide, they stick together, and form a new particle with a mass which is the sum of the masses of the two colliding particles. They now form a small ripple. The ripple moves more slowly back and forth than a single particle, according the "one-over-height" law. This law is well known in the study of dunes in the desert (Nishimori *et al.*, 1998) or sub-aqueous dunes (Fredsøe, 1996; Fredsøe and Deigaard, 1992), and can be illustrated by a simple geometrical argument. Suppose there is a flux of sand over the crest of a ripple or a dune q_{crest} (see figure 3.3). To make the ripple move a distance δx an amount of sand $h\delta x \sin(\phi)$ is needed (ϕ being

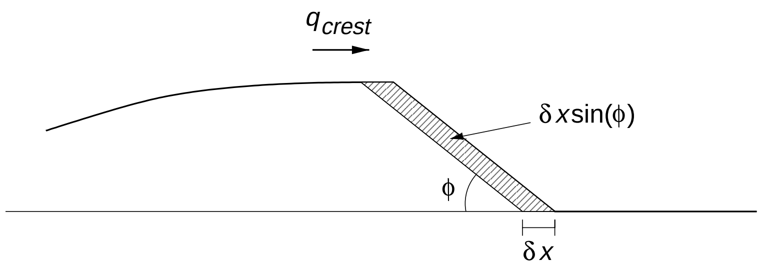

Figure 3.3: Geometrical illustration of the quantities involved in the derivation of the one-over-h law.

the angle of repose). As the sediment flux is amount of sand per unit time, the velocity of the ripple is $u_{ripple} = q_{crest}/(h\sin(\phi)) \propto 1/h$. A single grain has the velocity U_b, so the velocity of a particle with height h_i becomes: $u_i = U_b d/h_i$.

It is now possible to write the equations of motion for the particles as a system of coupled ODEs:

$$\dot{x}_i = \frac{d}{h_i} U(t) \underbrace{f\left(\frac{x_i - x_{i-1}}{\alpha_s h_{i-1}} \frac{U(t)}{|U(t)|}\right)}_{\text{positive half period}} \underbrace{f\left(\frac{x_i - x_{i+1}}{\alpha_s h_{i+1}} \frac{U(t)}{|U(t)|}\right)}_{\text{negative half period}}, \quad i = 1 \dots N \tag{3.1}$$

where $U(t)$ is an oscillating flow with amplitude U_b and period T.

When lengths are scaled by the diameter of the grains and time by the period T, it is possible to identify the three relevant dimensionless parameters of the model:

α_s – The length of the shadow zone divided by the height.
a_g/d – The amplitude of the motion of a single grain, divided by the grain diameter.
λ_f/d – The initial distance between the grains; $\lambda_f = L/N$, where L is the length of the computational domain and N is the total number of grains.

It can be argued that new grains will continuously be lifted from the bed and added to the initial number of grains in motion. As the part of the flat bed between the ripples is covered by the shadow zones of the particles, these stretches will be shielded from the full force of the flow, and only very slowly will new grains be loosened here. This small addition of new grains is what makes the rolling grains ripples eventually grow into vortex ripples. This slow growth is very well illustrated by the measurements of Stegner & Wesfried (1998).

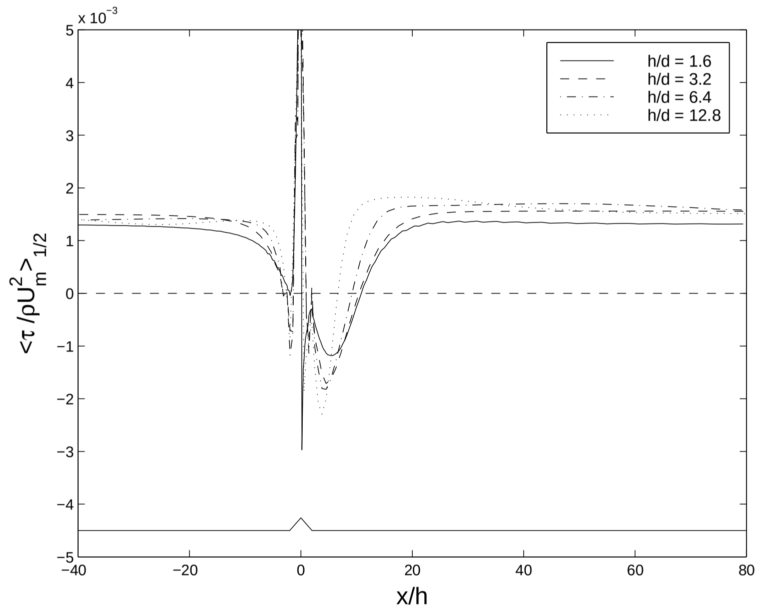

Figure 3.4: The shear stress on the bed averaged over the first half of a wave period, where the flow is predominantly from the left to the right. Results from ripples with four different heights are shown. The profile of bed is shown as the lower curve ($Re_a = 3300$ and $a/k_N = 333$).

Even though the model is quite heuristic, the values of its parameters can be related to physical parameters governing the grain properties and the flow.

The amplitude of the single-grain motion is

$$a_g/d = TU_b/2\pi d, \tag{3.2}$$

where the particle velocity on a flat bed can be found from equ. (2.30):

$$\frac{U_b}{U_f} = \alpha\left(1 - \sqrt{\left|\frac{\theta_c}{\theta}\right|}\right). \tag{3.3}$$

The number of grains in motion per area in the bed load layer n can be found using equ. (2.32) to be:

$$n = \frac{6}{\pi\mu_D d^2}(\theta' - \theta_c), \tag{3.4}$$

This can also be viewed as the initial density of grains, and from that the

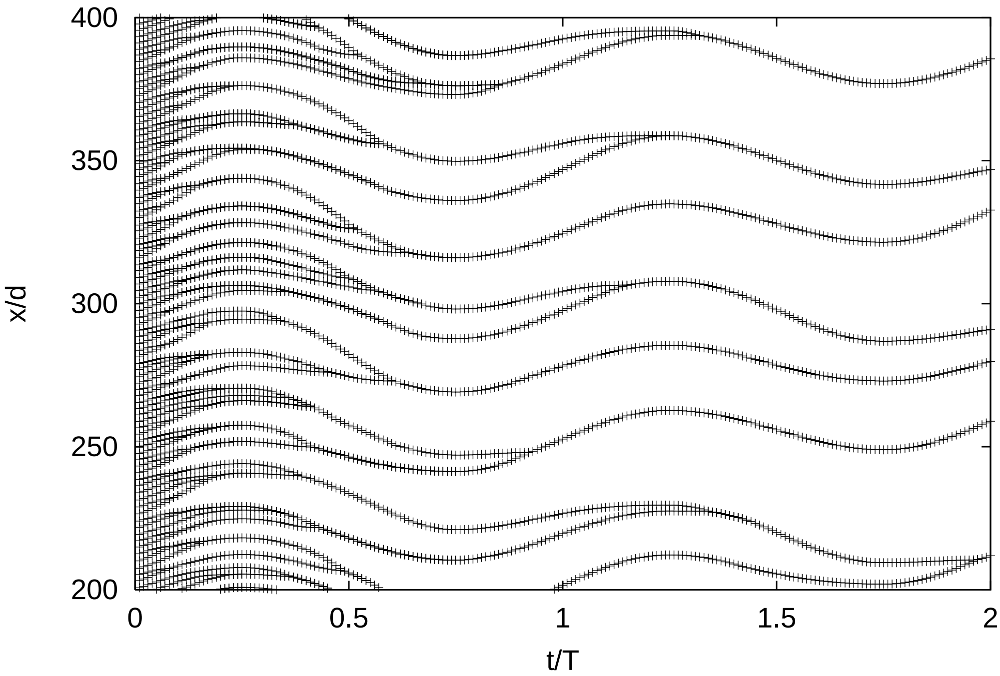

Figure 3.5: Zoom of the movement of the particle in the first two wave periods. $a_g/d = 35$, $\lambda_f = 3.23$ and $\alpha_s = 10.0$.

initial distance between the grains becomes:

$$\frac{\lambda_f}{d} = \frac{1}{\sqrt{n}d} \tag{3.5}$$

$$= \sqrt{\frac{\pi\mu_D}{6(\theta' - \theta_c)}}. \tag{3.6}$$

The last parameter, α_s, is a bit harder to estimate. Following the analogy to the flow over a backward facing step the length of the shadow zone must be larger than the length of the separation bubble ($6h$) and smaller than the point with maximum shear stress ($16h$). Thus $6 < \alpha_s < 16$.

The length of the shadow zone can also be examined using numerical simulations over a small triangular ripple. In figure 3.4 the shear stress on the bed is shown averaged over one half wave period. A strong separation bubble is seen in the lee side of the ripple. For the two smallest ripples, the length of the shadow zone is shorter than 20 ripple heights, and as the ripples become larger, the shadow zone diminishes. For the large height it seems as if the approximation $\alpha_s h \ll a$ breaks down, and the shadow zone is then

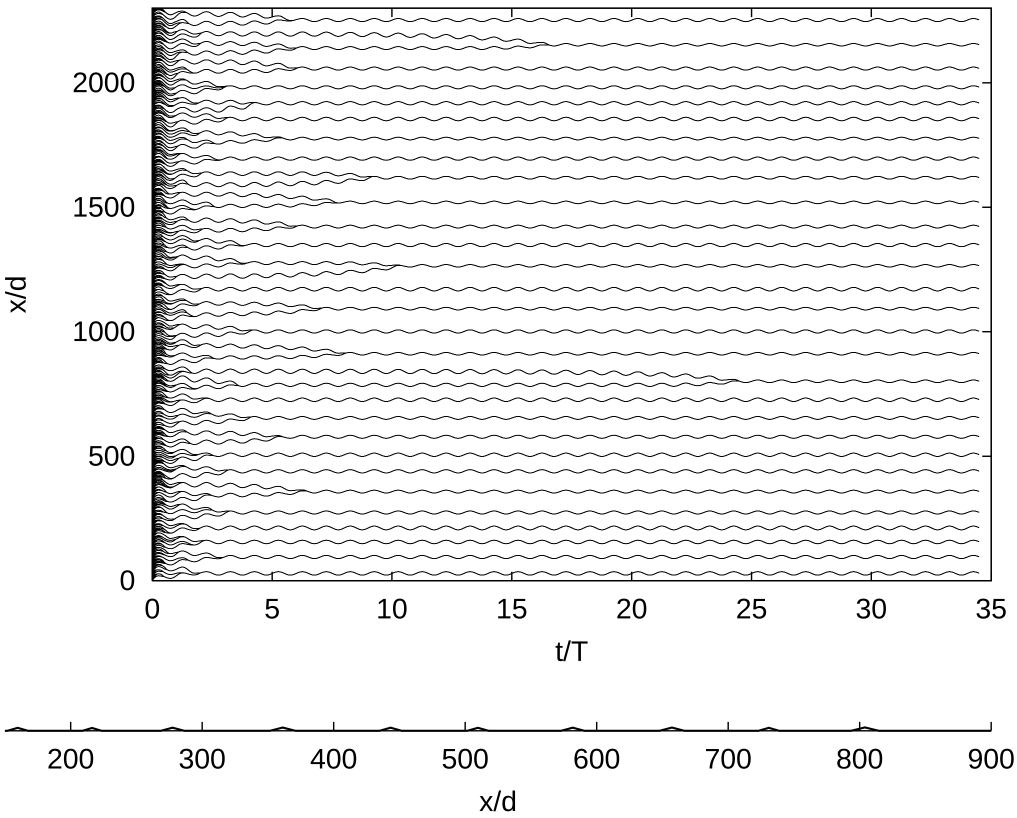

Figure 3.6: The development of the particles until steady state is reached (top). A section of the bed at steady state is shown in the bottom figure.

no longer just proportional to the height of the ripple, but is limited by the amplitude of the fluid motion.

3.2.2 Numerical and analytical solutions of the model

The runs in this section are based on a simple example with $\theta' = 0.1$, a grain diameter of $d = 0.2$ mm and a wave period of $T = 2$ sec. This gives: $a_g/d = 35$ and $\lambda_f/d = 3.23$. α_s is set to 10. As initial condition all particles have size and mass $1.0\pm$ 10 %, to add some initial perturbations. There are several thousand particles initially.

In the first few periods a lot of grains is colliding and merging (figure 3.5). As the ripples are formed and grow bigger the evolution slows down, until a steady state is reached (figure 3.6). There is clearly a well defined average spacing between the ripples in the steady state, but there is scatter

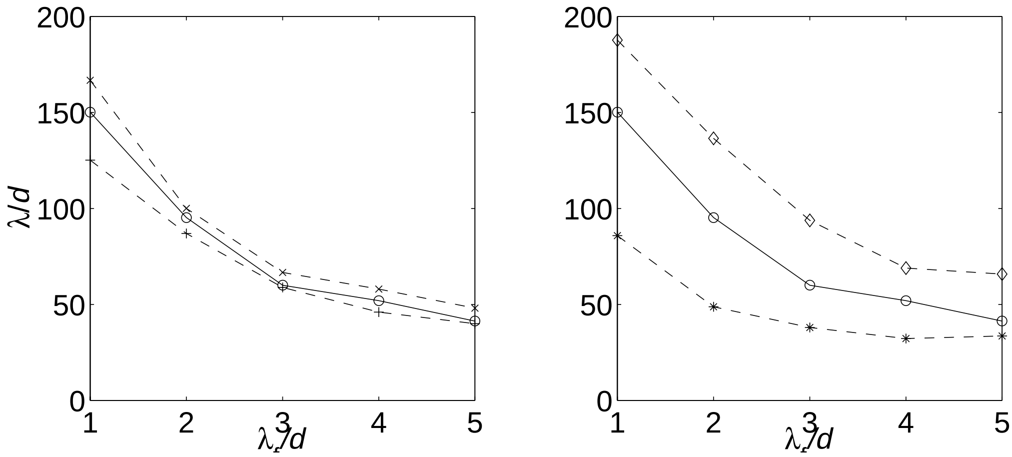

Figure 3.7: The average length between the rolling grain ripples at equilibrium. The basic example is shown with the full line: $a_g/d = 35$ and $\alpha_s/d = 10.0$. To the left, the value of a_g/d is varied, for pluses $a_g/d = 20$, crosses $a_g/d = 50$. To the right α_s/d is varied; stars: $\alpha_s/d = 7$, diamonds: $\alpha_s/d = 13$.

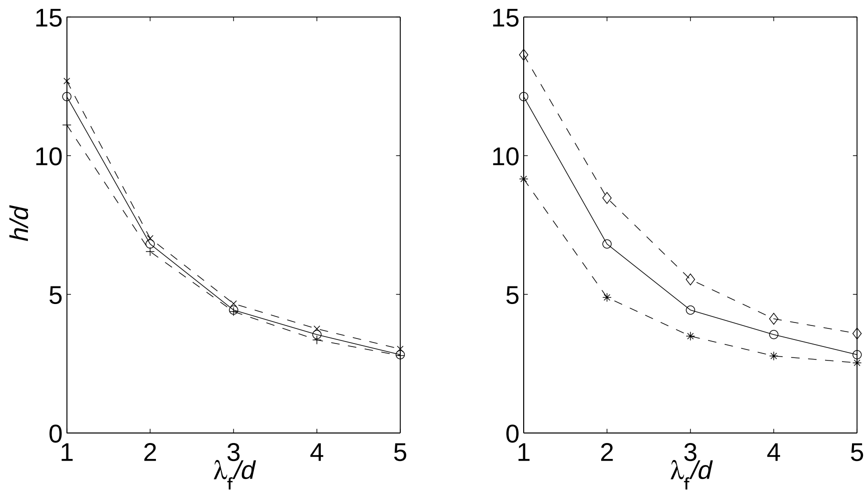

Figure 3.8: The average height of the rolling grain ripples at equilibrium. The legend is the same as in figure 3.7

of the spacing around the average value.

In figures 3.7 and 3.8 the average lengths and heights of the ripples in the steady state is shown with different values of the parameters. Each run is started from the initial disordered state.

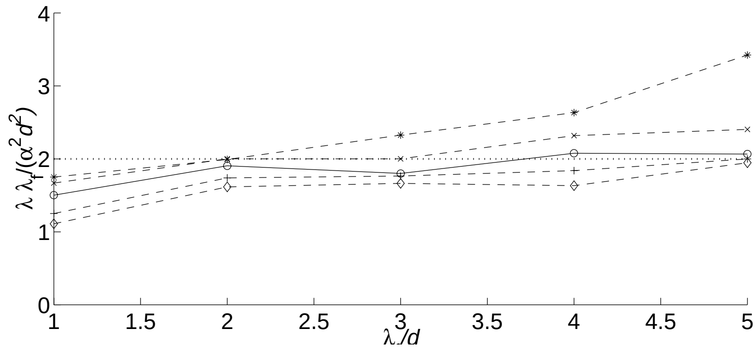

Figure 3.9: The equilibrium length between the rolling grain ripples, scaled using equ. (3.9). The legend is the same as in figure 3.7. The dotted line corresponds to the results of equ. 3.9.

Changing a_g/d does not produce any noticeable change in the wave length or the height of the rolling grain ripples. The ripples do depend on the length of the shadow zone α_s/d. The longer the shadow zone, the larger the ripples. This can be used to estimate the average equilibrium length between the ripples. When the distance between two ripples is longer than the shadow zone of the ripples, they are no longer able to interact. The criterion is:

$$\lambda_{eq} \approx 2\alpha_s h_{eq}, \tag{3.7}$$

$$= \alpha_s^2 \sqrt{\frac{24}{\pi \mu_D}} \sqrt{\theta' - \theta_c} \tag{3.8}$$

where subscript eq denotes average value at equilibrium. The height at equilibrium can be found by splitting the initial number of particles evenly onto the equilibrium ripples. Then $m_{eq} = \lambda_{eq}/\lambda_f d^2$ and so $h_{eq}/d = \sqrt{\lambda_{eq}/\lambda_f}$, which gives a minimal equilibrium wave length:

$$\frac{\lambda_{eq}}{d} \approx 2\frac{\alpha_s^2 d}{\lambda_f}. \tag{3.9}$$

This result is illustrated in figure 3.9. It is seen that the length between the ripples is around the value given in equ. (3.9). There still seem to be a weak dependency on λ_f/d which is not accounted for in equ. (3.9). The fact that the final wave length is reached when the ripples no longer interact shows that the exact form of the interaction function f is not important.

3.2.3 Comparison with experiments

The only parameter which has not been accurately determined is α_s. The value of this parameter can be estimated by comparison with measurements.

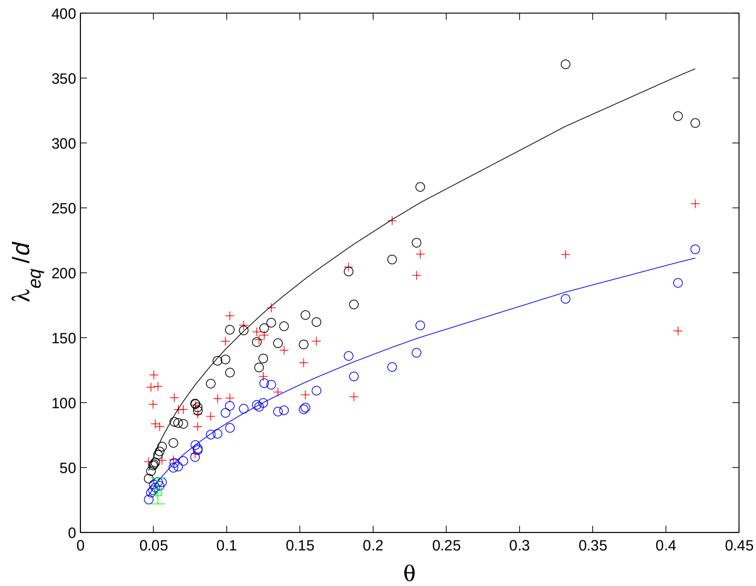

Figure 3.10: Comparison between the measured wave lengths of rolling grain ripples (red crosses), results from the model (circles), and from (3.9) (full lines). The blue lines and circles correspond to $\alpha_s = 10$, the black ones to $\alpha_s = 13$. The critical Shields parameter is 0.04 and $\mu_D = 0.65$. The green square corresponds to the result from the linear stability analysis in as made by Blondeaux (1990)

In 1976, Sleath made a series of experiments, measuring the wave length of rolling grain ripples (Sleath, 1976). The ripples were formed on a flat tray oscillating in still water using sand of two different grain sizes: 0.4 mm and 1.14 mm. The shear stress on the flat bed for the experiments can be found using Jonssons friction factor (1976), and from this the Shields parameter can be found. The range of Shields parameters was from the critical Shields parameter to $\theta' = 0.42$. For the high Shields parameters the rolling grain ripples were very unstable, and they quickly developed into vortex ripples. The measured wave length then reflects the length of the rolling grain ripples before they developed into vortex ripples.

In figure 3.10 the experimental results are compared with equ. 3.9 for $\alpha_s = 10$ and 13. The results using equ. (3.9) are shown with lines together with runs from the full model. The correspondence between the model and the experiments is quite good, but there are some discrepancies. There are a few points with small wavelengths for which the model does not fit the measurements. These measurements are taken very near the critical Shields parameter, which implies some additional complications. The grains used in the experiment are not of a uniform size; rather are they a part of a distribution of grain sizes, and the grain size reported is then the median of the distribution, d_{50}. The Shields parameter is calculated using the median of the distribution, but actually one could calculate a Shields parameter for different fractions of the distribution, thus creating a θ_{10} a θ_{50} etc.. When θ_{50} is smaller than then the critical Shields parameter, θ_{10} might still be higher than the critical Shields parameter. This implies that grains with a diameter smaller than d_{50} will be in motion, while the larger grains will stay in the bed. As only d_{50} is used in the calculation of the equilibrium wave length, the distance between the grains λ_f will be overestimated near the critical Shields parameter, where the effect of the poly-dispersity is expected to be strongest. An overestimation of λ_f will lead an under-prediction of the ripple length, which is exactly what is seen in figure 3.10

The weak assumption in the model is that the length of the shadow zone is proportional to the height of the ripple. For very small ripples this approximation is good, but as the ripples grow larger, the condition $\alpha_s h \ll a$ is no longer valid, and the length of the shadow zone will be shorter. The result is that the wave length for large ripples is overestimated, which is also apparent from figure 3.10.

3.3 Linear stability analysis

In this section the linear stability analysis of the boundary layer created by an oscillatory motion will be presented. The analytical results are compared with the numerical solution of the Navier-Stokes equations, and a sensitivity analysis of the model is performed.

In 1976 Sleath showed that the laminar flow over a flat bed with a sinusoidal perturbation creates circulation cells on average (see figure 3.12)(Sleath, 1976). This is quite easy to understand intuitively. When the flow is from left to right, there will be a stronger flow near the bed on the left side of the perturbation than on the lee side because of the converging flow. The same will happen on the other side when the flow reverses. Averaging the flow in the first and the second half of the wave period produces a net flow towards the crest. Due to continuity, a reverse flow will have to be created higher up, leading to the closed circulating cells. This net flow near the bed leads to a net transport of sand towards the crest, giving a net growth of the perturbation. The only stabilising factor is the gravity pulling downwards, and it is this competition between the flow trying to destabilise the bed and the gravity acting to stabilise which determines the stability/instability of a given wave length.

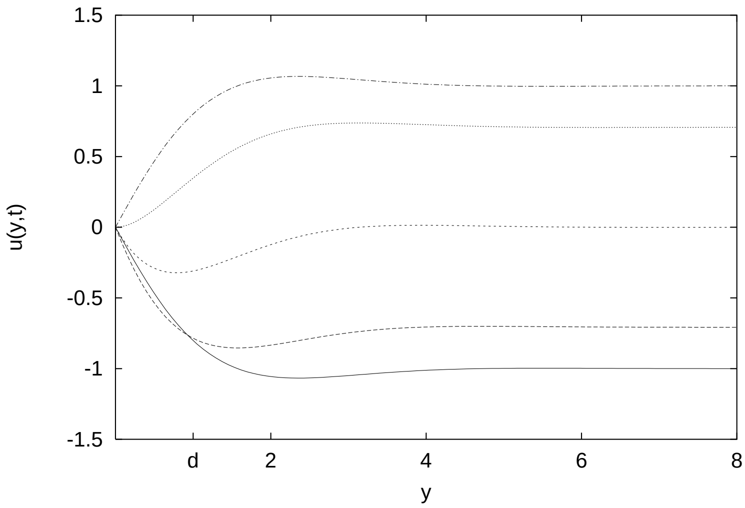

Figure 3.11: The zero order solution at $\omega t = 0$ (bottom) to π (top). The grain diameter is shown on the horizontal axis for $Re_d/Re_\delta = 1$.

3.3.1 Mathematical formulation of the problem

The linear stability analysis can be split into four parts: 1) the basic flow over a flat bed, 2) the flow over the perturbation, linearised around the basic solution, 3) the sediment motion and 4) the coupling between the sediment motion and the change of the perturbation. In this chapter the flow problem will be solved fully numerically, and thus the approximations used in the linearisations can be validated.

The flow problem

Consider a flat plate in water oscillating with a angular frequency ω' and velocity U'_m (in this section a prime denotes a dimensional variable). The flat bed is perturbed with a sinusoidal perturbation with amplitude ϵ', wave number α' and growing in time as $C(t)$:

$$h'(x', t') = \epsilon' C(t') \cos(\alpha' x'). \tag{3.10}$$

For now, only the flow problem over a fixed bed is examined, so $C(t') = 1$. The flow is forced by an outer oscillating flow:

$$u'(t') = -U'_m \cos(\omega' t'). \tag{3.11}$$

All variables are non-dimensionalised with the characteristic length scale in the Stokes flow, $\delta' = \sqrt{2\nu'/\omega'}$ and the maximum velocity of the outer flow U'_m.

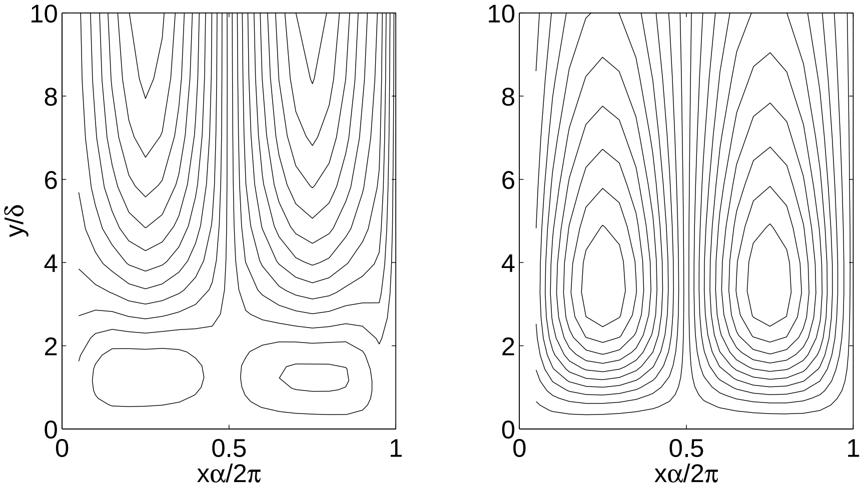

Figure 3.12: The time-averaged flow over perturbations with $\alpha = 0.025$ (left) and $\alpha = 0.15$ (right) and $Re_\delta = 80$.

The Navier-Stokes equations are expanded to first order in ϵ, and the resulting equation is an Orr-Sommerfeld equation, which can be solved numerically. For details of the derivation and the numerical solution, see the papers by Vittori (1989) and Blondeaux (1990).

To zero order the classic Stokes solution is obtained (see e.g. Landau and Lifshitz (1959), §24):

$$u(y,t) = (\cos(y)e^{-y} - 1)\cos(\omega t); \tag{3.12}$$

an oscillatory flow with strong gradients near the bed and a phase that varies with y (figure 3.11). This solution is supposed to be valid for flow over a bed with sand as long as the grain diameter $d' < \delta'$, or $d < 1$. The average shear stress on the bed produced by the zero-order solution is zero, so the grains just move back and forth, without any net motion.

The flow at first order is influenced by the bottom perturbation. When the flow is averaged over one wave-period, steady recirculating cells are formed (figure 3.12). These cells create a shear stress on the bottom directed towards the crest of the perturbation. The flow in figure 3.12 is calculated using a full numerical solution of the Navier-Stokes equations. The spatial Fourier transform of the numerical solution can be used to validate the assumption behind the linearisation of the flow. It was found that up to a steepness of the perturbation of about 0.1, only the first component was relevant. This means that the first order solution is actually a very accurate description of the flow.

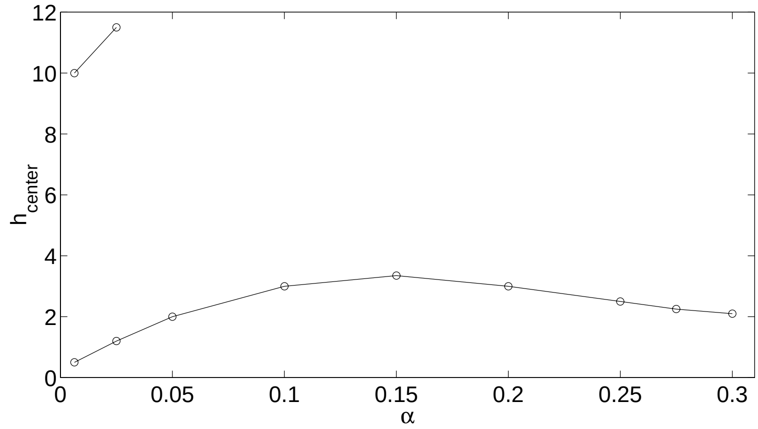

Figure 3.13: The height of the centre of the circulation zones as a function of the wave number. $Re_\delta = 80$. The upper curve shows the height of centre for the cases where there is another set of rolls.

The centre-points of the lower pair of recirculating cells are quite close to the bed, and the height of the centre is a function of the wave number of the perturbation α (figure 3.13). The shorter the perturbation, the closer the cells come to the bed. When the perturbations become longer, the cells move closer to the bed again. This effect is accompanied by the creation of another set of rolls on top of the lower set, which is now squeezed closer to the bottom (as in figure 3.12, left).

Imagine now a grain with a diameter $d = 1$. For the long wave lengths ($\alpha < 0.05$), this grain will be of the size of the whole circulation zone, and the strength of the net force moving it towards the crest will be small, or the net force might even move the grain towards the trough. This is the mechanism setting the upper wave length of the ripples. For the lower wave length, the action of gravity on the grains is important.

The sediment transport problem

As described in chapter 5, the Shields parameter is used to find the flux of sand on the bed. As the Shields parameters where rolling grain ripples are created is small, the Meyer-Peter formula equ. (2.35) is well suited for this study. Furthermore, the slopes are small in the perturbation theory, so the linear gravity correction is sufficient to account for the effect of the sloping bed (2.36).

In the laminar boundary layer under a wave, the vertical gradient of u' varies quite rapidly, and it can be more convenient to use the velocity at some point, y_0', away from the bottom instead of the shear stress. To first order the shear stress on the bed can be written:

$$\tau' \approx \rho'\nu' \frac{u'(y_0')}{y_0'}, \tag{3.13}$$

where y_0' is taken at some fraction of the grain diameter, typically $y_0' = 1/2d'$. Again, lengths are non-dimensionalised with δ', and then the Shields parameter can be written as:

$$\theta = u(y_0)\frac{F_d^2}{Re_d}\frac{d}{y_0} \tag{3.14}$$

where $Re_d = d'U_0'/\nu'$ and $F_d = U_0'/\sqrt{(s-1)g'd'}$. The bed load is:

$$\begin{aligned} \phi_b &= 8(\theta - \theta_c - \beta\frac{\partial\eta}{\partial x})^{1.5} \text{ for } \theta > \theta_c \\ \phi_b &= 0 \text{ for } \theta \leq \theta_c. && (3.15) \\ & && (3.16) \end{aligned}$$

The addition of the gravity correction to the sediment transport provides a stabilising mechanism to counterbalance the destabilising effect of the flow. The gravity becomes stronger the shorter the wavelengths, as it goes like $\epsilon\alpha$.

The formula for calculation of the sediment flux used by Blondeaux is a rarely used one, made by Grass & Ayoub (1982). It can be written as:

$$\phi_{GA} = a(s-1)\theta^{1/2+b}R^{0.64b}, \tag{3.17}$$

with $R = U_f d/\nu$ and a and b are parameters. This formula was derived on the basis experiments made with just one grain size (140 microns), and includes four different regimes, with four different coefficients for a and b. For the regime coming closest to the present calculations $a = 3.24$ and $b = 3.40$. The Grass & Ayoub formula has been used here only for comparison with the results of Blondeaux and co-workers.

Coupling between sediment transport and bottom evolution

The evolution of the bed is found using the continuity equation for the sand (2.48), which in non-dimensional form reads:

$$\frac{\partial h(x,t)}{\partial t} = -\frac{1}{u'\delta'(1-n)}\sqrt{(s-1)g'd'^3}\frac{\partial\phi_b}{\partial x}. \tag{3.18}$$

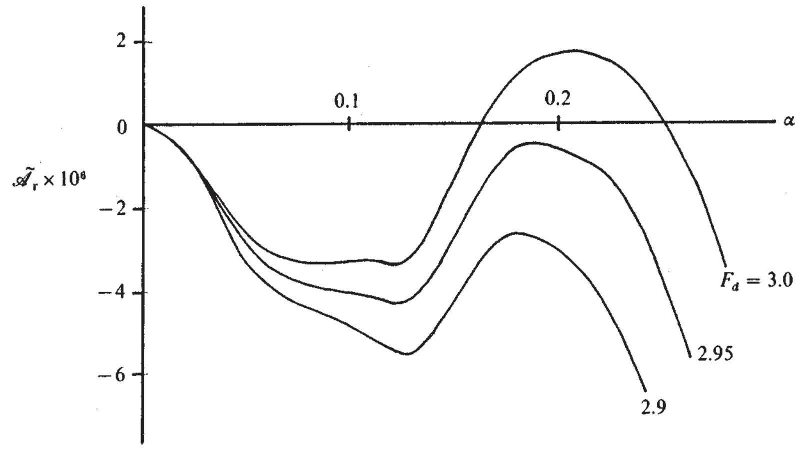

Figure 3.14: The growth rate from the stability analysis for different values of F_d ($Re_\delta = 80$, $Re_d = 80$ and $\beta = 0.15$, figure taken from Blondeaux (1990)).

To find the average growth/decay-rate of the bottom perturbation, only the first component of the Fourier transform of $\partial h(x,t)/\partial t$ is used. A generalised growth-rate can then be defined as:

$$c = -\frac{1}{\epsilon}\left\langle \int_0^{2\pi/\alpha} \frac{\partial h(x,t)}{\partial t} \cos(\alpha x) dx \right\rangle, \tag{3.19}$$

where $\langle \cdot \rangle$ denote average over one wave period.

3.3.2 Results

The results shown are from one example with $Re_d = Re_\delta = 80$ and $F_d = 3.0$ (figure 3.14 and 3.15). This means that the diameter of the grains are equal to the thickness of the boundary layer; $d' = \delta'$, which is on the borderline of the validity of the Stokes boundary layer. When $d' > \delta'$ the grains are larger than the boundary layer thickness, and then the boundary layer becomes turbulent (see figure 2.13 in (Fredsøe and Deigaard, 1992) for a nice overview of laminar versus smooth and rough boundary layers).

In figure 3.14 the growth rate as calculated by the linear stability analysis of Blondeaux (1990) is shown. This analysis is performed with $\theta_c = 0$. Long waves are neutrally stable, and there is a band of unstable wavelengths around $\alpha = 0.2$.

The results from the numerical, fully non-linear analysis with the same set of parameters as in 3.14 is shown in figure 3.15. This analysis has been performed with the two different sediment transport formulas, and for $\theta_c = 0$

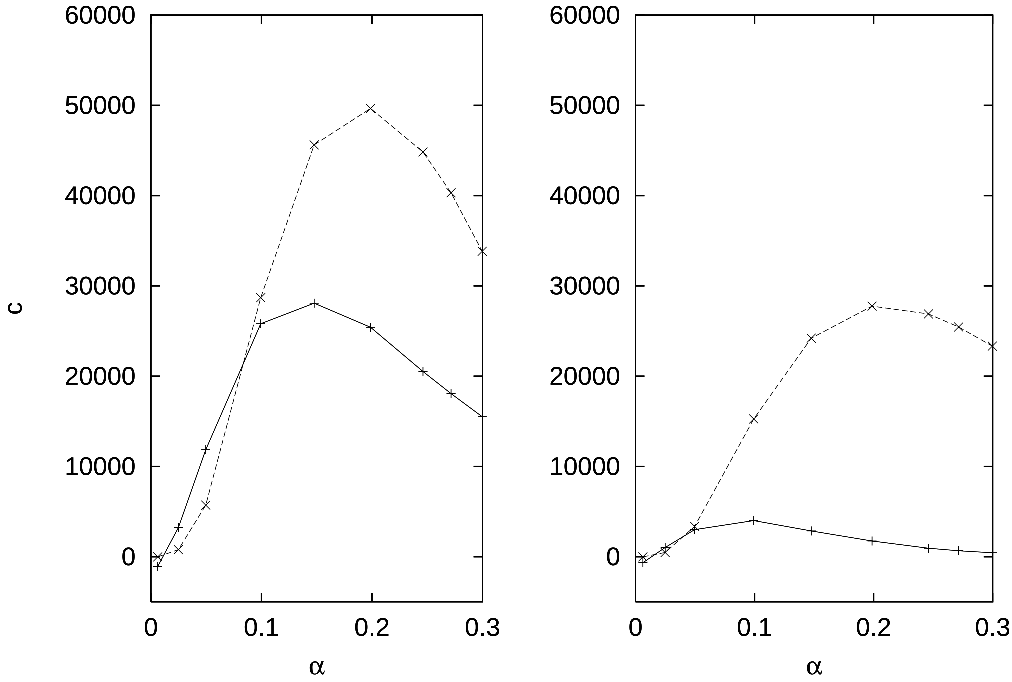

Figure 3.15: The growth rate from the numerics. The full line is the results using Grass and Ayoub's sediment transport formula (3.17), and the dashed line is computed using the Meyer-Peter formula (3.16). $Re_\delta = 80$, $Re_d = 80$, $F_d = 3.0$ and $\beta = 0.15$. To the left $\theta_c = 0$ and to the right $\theta_c = 0.05$.

and $\theta_c = 0.05$. Here, again, a band of unstable wave lengths is observed, but this time the band is much wider than in the linear stability case, and there is only a narrow band of stable wave lengths in the long range limit. The wave length of the maximally unstable wave length is of the same order as in the analysis by Blondeaux.

3.3.3 Dependence on parameters

Several parameters affect the results of the stability analysis. These are: y_0/d, β and θ_c. In figure 3.16 the growth rate is shown for a range of β and y_0/d. Increasing the gravity β makes the profiles more stable. At $\beta = 0.50$ there are no unstable wave lengths (except for $y_0/d = 0.5$). Varying y_0/d reveals a maximum of the growth rate at $y_0/d = 0.5$.

The maximally unstable wave length, appears to become longer when the gravity is increased (figure 3.17). This is no surprise, as the gravity is strongest for small wave lengths. The results for the two different sediment

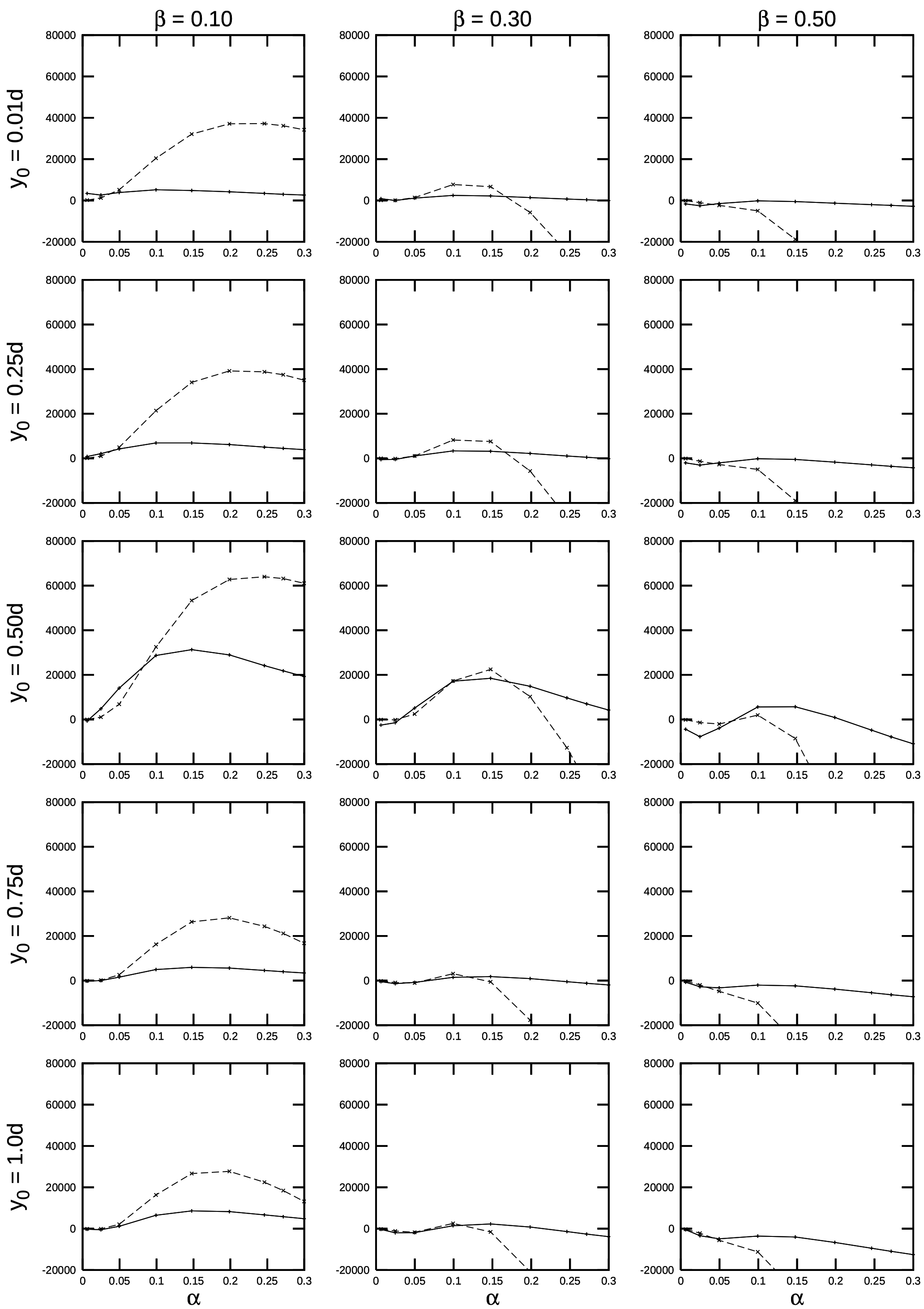

Figure 3.16: The growth rate as a function of α for different values of β and y_0. $\theta_c = 0$ (the symbols are same as in figure 3.15).

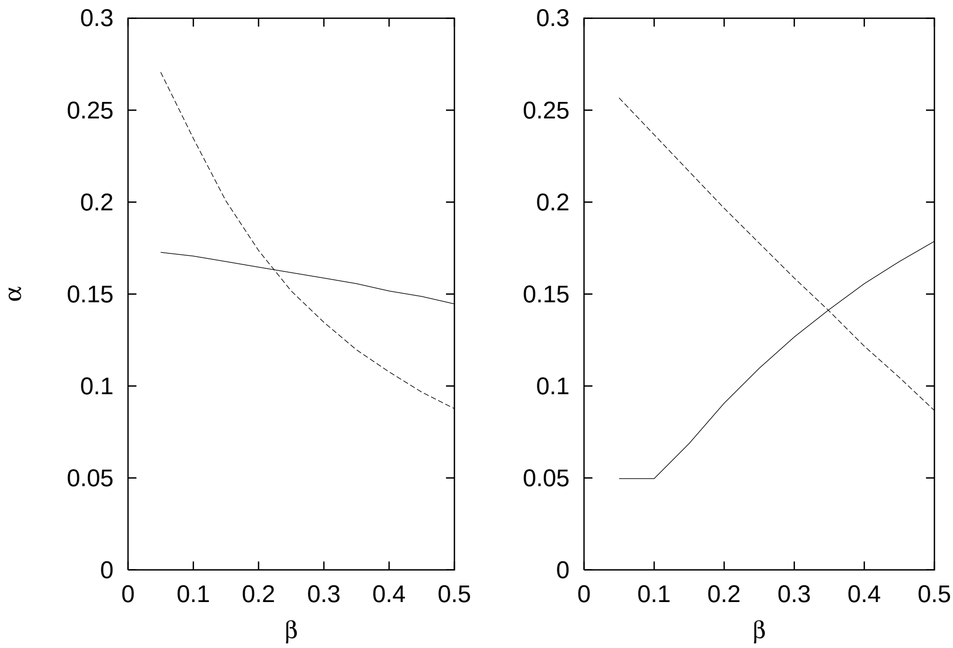

Figure 3.17: The maximally unstable wave length as a function β for $y_0/d = 0.5$. Left: $\theta_c = 0$, right $\theta_c = 0.05$.

transport formulas are not too far from each other. Turning on the critical shear-stress changes the results quite drastically for the results obtained by using the Grass & Ayoub formula. Now the critical wave length appears to be shorter. The results found by using the Meyer-Peter formula are also affected, but not as much.

The results of the stability analysis can briefly be summarised as follows:

- Due to the competition between the gravity which tries to stabilise perturbations and the drag which tries to destabilise perturbations, a maximally unstable wave length is found.
- For a short wave length the growth is limited by the action of gravity.
- For large wave lengths the growth is limited by the presence of a second set of recirculating cells.
- For most parameter values a broad band of wave lengths is unstable.
- The model is generally very robust. Changing the values of the parameters does not change the value of the maximally unstable wave length considerably.

Extensive comparison with experiments has not been carried out, but the case that has been studied in this section is marked in figure 3.10. The theory seems to under-predict the selected wave length even more than the simple model, a fact that was also noted by Blondeaux (1990).

It is interesting to note that without a threshold for grain motion, the stability theory would actually make the first bifurcation a supercritical pitchfork bifurcation. This makes it (at least in principle) possible to derive an amplitude equation from the theory.

Finally, the broad band of unstable wave lengths deserves a comment. Often in pattern forming systems, the non-linearities will make the many unstable wave lengths interact, creating rich pattern dynamics (e.g. Cross & Hohenberg (1993)). In rolling grain ripples this dynamics is not seen, in fact the rolling grain ripple pattern does not show any dynamics. The ripples just line up in parallel ridges, and real dynamics first start when they begin to grow to vortex ripples.

3.4 Creation of vortex ripples via nucleation

The flat bed is a theoretical abstraction which is hard to realize in an experimental situation, and which is rarely found in nature. In practice there will always be some finite perturbation present on the bed: a bump, a relict ripple or a boundary. On this perturbation the maximum Shields parameter θ_p will be larger than the maximum Shields parameter on a flat bed (θ'), and therefore there can be grain motion even though there is no grain motion on the flat bed, i.e. $\theta' < \theta_c < \theta_p$. This grain motion will create a ripple, which again will create a new perturbation on either side, and so ripples will spread into the flat bed as a propagating front. This way of ripple creation I have called *nucleation*, because new ripples nucleate around a perturbation. The velocity of the propagating front of ripples has been measured by Carstens (1969) and Nielsen (1979). In figure 3.18 the creation via nucleation is illustrated by the simulation of the flow and sediment transport over a small triangular ripple on a flat bed. Around the ripple the average bed load is directed towards the ripple, which in effect will make the ripple grow. The area where the new ripple will be nucleated is the area where the average change in height $\langle \partial h/\partial t \rangle$ is positive. From the continuity equation (2.48) of the sediment these are the areas where $\langle \partial \phi_b/\partial x \rangle$ is negative, which is marked on the figure as "deposition".

The fact that ripples can form and exist under conditions where the flat bed is stable is important, because it means that the initial bifurcation, that is the formation of ripples from the flat bed, is sub-critical (as was also

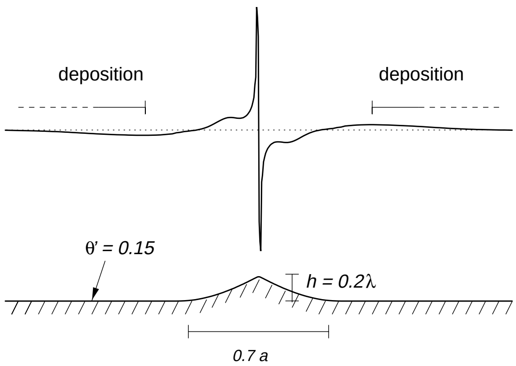

Figure 3.18: The bed load averaged over one period ($\langle \phi_b \rangle$). The areas where $\partial \langle \phi_b \rangle / \partial x$ is negative are areas of deposition where a new ripple is being nucleated.

realized by Scherer *et al.* (1999)).

A second implication of the nucleation of ripples is that it is experimentally quite difficult to study the first bifurcation, because the initial patterns do not saturate at a small height, but instead grow to vortex ripples. Another problem is the boundary effects: it is very hard to maintain a flat bed without perturbations intruding from the boundaries.

3.5 Concluding remarks

The simple granular model, based on the motion of the individual grains, shows quite good agreement with the measurements by Sleath (1976). The model predicts that the selected wave length is just a function of the Shields parameter, with the wave length divided by the grain diameter $\simeq \sqrt{\theta - \theta_c}$.

While the granular model is simplistic and heuristic, the linear stability analysis is based on a full solution of the flow around a perturbation on the bed. Still, several parameters enter the model, the gravity parameter β and the height above the bed where the fluid flow is "measured", y_0. The actual growth rates predicted are quite sensitive to the values of these parameters, but fortunately not the maximally unstable wave length. The broad band of unstable wave numbers found in the linear stability might suggest a rich dynamic of the pattern, a thing that is not seen in the real rolling grain ripples.

Which of the two models describes the true nature of the rolling grains ripples best is not a simple question to answer. To examine that, more careful experiments on the rolling grain ripples are be needed. One simple test would be to observe the dynamics of established rolling grain ripples, by changing the conditions such that the equilibrium wave length is changed. In the granular model the rolling grain ripples are not able to split up and make shorter ripple once a wave length is selected. They are able to form longer ripples, though. In the model based on the linear stability the ripples would be able to change in both directions, especially if the established wave length has a negative growth under the changed conditions. However, such experiments are a complicated business, mostly because of invasion of vortex ripples, and because the rolling grain ripples do not seem to be stable.

Before using more time and energy on this question, one also have to consider if rolling grain ripples are really important. As a pattern forming system they are boring. The ripples are very one-dimensional, that is the patterns have no defects and no dynamics. The selected wave length of the rolling grain ripples has no relevance to the selected wave length of the vortex ripples. These are created by a completely different dynamics, which has nothing in common with the rolling grain ripples. As the rolling grain ripples are only created from a flat bed and are very sensitive to a perturbation nucleating vortex ripples, they also have no relevance for the coastal engineer – they are practically non-existing in the coastal zone.

Chapter 4

The flow around vortex ripples

The study of the dynamics of the vortex ripples is to a first approximation a flow problem. This is in contrast to, for example, the creation of ripples in air, which is believed to be dominated by the granular dynamics (Anderson (1990), Hoyle & Woods (1997), Terzidis *et al.* (1998), Nishimori & Ouchi (1993) and Csahók *et al.* (1998). It is quite easy to realize that the flow is important, because the selected wave length is mainly a function of a, with the grain diameter entering as a second parameter through the Shields parameter. Had the problem been a problem of granular dynamics, the grain size would certainly have been more important. The granular properties enter mainly through the settling velocity, which together with the Shields parameter determines the amount of suspension present.

The complexity of the flow around vortex ripples has been a major obstacle for the development of an understanding of the dynamics of the ripples. The main difficulties, which makes a simple description of even the qualitative features of the flow difficult, are listed below:

1. The flow is fully turbulent.

2. Because of the constant oscillatory forcing from the wave, the flow never reaches a steady state.

3. The flow involves regions of separation, and even advection of detached separation bubbles (the vortices).

The first two points do not exclude a qualitative description. The turbulent flow over a flat bed can be resolved to some degree of accuracy if the profile is assumed to be logarithmic in the boundary layer:

$$u(y,t) = \frac{U_f(t)}{\kappa} \ln\left(\frac{30y}{k_N}\right), \tag{4.1}$$

where U_f is the friction velocity, $U_f \simeq \sqrt{\tau_b/\rho}$, and the shear stress can be found using Jonsson's friction factor, equ. (1.4) and (1.5). The Nikuradse equivalent roughness is just the grain diameter for a rough wall and $\approx 2.5d_{50}$ for a bed with loose sand (Fredsøe and Deigaard, 1992). This description of the flow using the "averaged" flow quantities, the friction f_w and the roughness k_N is valid for $\lambda/a \gg 1$, but for ripples where $\lambda/a = O(1)$ the averaged quantities are furthermore a function of both the geometry of the ripple and the flow parameters. The problem of finding k_N and f_w for a rippled bed is addressed in section 4.4.

To understand the flow around the ripples in detail, the problem in the point no. three on the previous page is encountered, which is the largest barrier for a mathematical flow description. Even in steady flow it is very difficult to resolve separation zones, due to the break-down of the boundary layer approximation at the point of separation. This breakdown can be circumvented to some degree by using an averaged version of the boundary layer equations (Bohr *et al.*, 1997; Putkaradze, 1997), but this description is not currently able to resolve the flow around ripples.

Due to these problems the only way to study the flow has been through experiments and, more recently, with numerics.

4.1 Previous efforts (and some more recent)

The first to systematically study the vortex ripples was Mrs. Hertha Ayrton (1910)[1] . She studied ripples in a small tank which was tilted in an oscillatory manner to create a standing wave. It was obvious to Ayrton that the vortex created by the ripple crest was important for the ripples (figure 4.1). Even though this setup is not the most convenient for the study of ripples, because the wave length of the ripples constantly changes throughout the length of the tank, her observations are remarkably detailed. Using ground pepper as tracer, she described the creation and the motion of the vortices.

Detailed measurements of the flow over a ripple bed have been made with laser-doppler by Du Toit & Sleath in 1981 (1981), and in 1985 by Hedegaard (1985). Using micro-propellers she made very detailed measurements of the velocity close to the bed over a fixed smooth or rough ripple. Among other things she found that the vortex exercised quite a strong shear stress on the ripple surface.

[1] Mrs. Ayrton was the first woman to present a paper before the Royal Society of London in 1910. The present paper was actually written in 1904, but the publication postponed until 1910.

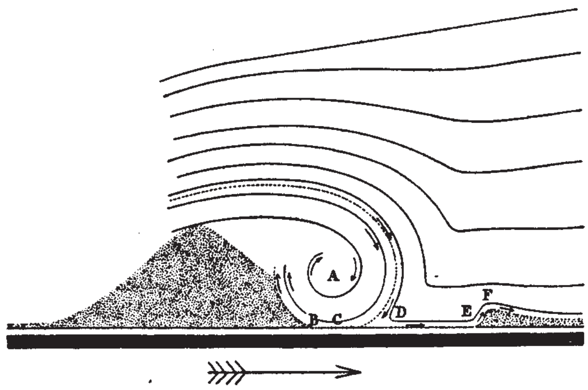

Figure 4.1: The formation of the lee vortex (A), as seen by H. Ayrton (1910). The figure also illustrate the formation of a new ripple by nucleation (see chapter 3).

Most of the effort in recent years has been focused on obtaining a numerical solution to the flow over vortex ripples. The first efforts were made using the discrete vortex (DV) method. To be very brief, the idea of the method is to advect a number of point vortices in a potential flow, which in turn is influenced by the presence of the vorticity carried by the point vortices. For a detailed description of the method in relation to the flow over ripples see Perrier (1996). The method has turned out to be quite effective in some flows, and it seemed obvious to try it on the flow over ripples. This have been done by Longuet-Higgins (1981), by Blondeaux and Vittori (Blondeaux and Vittori, 1990; Blondeaux and Vittori, 1991), by Hansen, Fredsøe and Deigaard (1994) and very thoroughly by Perrier (Perrier *et al.*, 1994; Perrier, 1996). This method resolves many of the qualitative features of the flow, but for quantitative work it does not perform so well – it has problems even making a logarithmic profile over a flat bed.

The alternative is to use turbulence modelling. Many have tried this as well: Sato *et al.* (1986), Aydin using k-ϵ modeling (1987), Tsujimoto *et al.* using a k-ϵ model (1991), Hyoseob *et al.* using a mixing length model (1994), Perrier using k-ϵ and Reynolds Stress turbulence modeling (1996). Where the DV method calculates the full velocity field, the turbulence models only captures the averaged velocities. This makes it easy to create a nicely converged flow, suitable for i.g. morphological calculations.

Common for all numerical solutions of the flow over the ripples is that it is quite easy to make a solution that looks like the "real thing". It is hard not to form a vortex in the lee side, and have it ejected and advected when the flow reverses. What is much more difficult, and what has taken up quite a large bit of the time for the present Thesis, is to obtain a solution that compares quantitatively with measurements.

4.1.1 Comparison with experiments

In the attached article ("Wave plus current over a ripple-covered bed") high quality laser-doppler measurements of the flow over fixed ripples were performed. The measurements were made under both wave-only and wave plus current conditions. The measurements were compared with the simulations of the computational model.

The comparison was not without complications. The measurements were made in a wave flume with relatively shallow water. Thus the waves were not linear, and the orbital motion had a vertical component, which was significant even quite close to the ripples. Still the comparisons were quite favourable for the model for wave conditions.

For the wave plus current case, the problems with the real waves were even harder, as in this case the waves were interacting with the current. This comparison was harder because it was not simple to establish the same flow conditions in the simulations as in the measurements. The main problem here was finding the right pressure signal for driving the flow. The agreement was consequently not as good as in the wave-only case. This does not necessarily mean that the model performs badly in a wave plus current situation, just that the experiments were not optimal for comparing with this model. The optimal set of experiments would be measurements of velocity profiles over ripples in a U-tube, which is exactly the same condition as is reproduced in the model.

A comparison between measurements of the flow over a trench in a U-tube and the results from a model based upon the same code as the present model was performed by Jensen (1998). This experimental setup was much better suited for a comparison with the simulations, and the correspondence between the measurements and the simulations was very good.

4.1.2 Live vs. fixed ripples

A very common simplification in the study of ripples is to assume that the flow over fixed ripples is the same as that over real "live" ripples. All numerical work to date has been conducted over fixed ripples, whereas there are measurements over both fixed and live ripples. As the real ripple performs some movement during the wave period, especially around the crest, it is not obvious that the flow is exactly the same as over the fixed ripple.

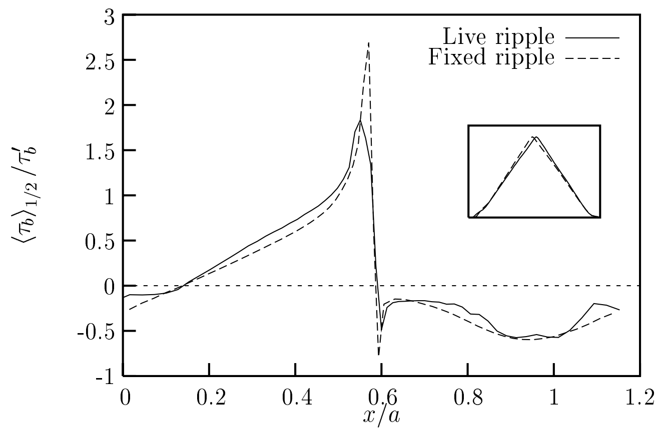

Figure 4.2: The friction velocity averaged over one half period, using both a fixed and a moving ripple. The inset shows the crest of the moving ripple in the two outermost positions ($\lambda/a = 1.2,\ h/\lambda \simeq 0.25$).

A comparison between the shear stress on a fixed and a live ripple has been performed. The fixed ripple had approximately the same dimensions as the live ripple, namely $\lambda/a = 1.2$ and $h/\lambda = 0.25$. As can be seen in figure 4.2, the difference between the shear stress on the bed between the two simulations is remarkably small. Of course the shear stress in the simulation with the movable bed is not as smooth as in the fixed bed case, but this is to be expected as the crest moves back and forth (see the inset).

The same comparison has been made with a wave plus current flow (figure 4.3). Here the used profile for the fixed ripple was exactly the same as for the morphological calculation, and than is why even better agreement is achieved. This also means that some instabilities caused by small ripples in the morphological profile is seen in the run with the fixed profile. In the morphological calculation these would be swept out by an avalanche.

4.2 Wave-only flows

In this section the flow governed by waves without a superposed current is treated.

4.2.1 Vortex dynamics

The most characteristic feature of the flow over vortex ripples are the dynamics of the vortices formed by the ripple. To visualise the vortices it is

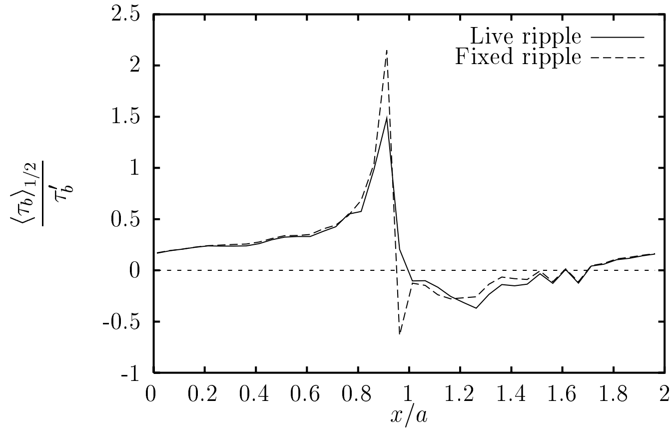

Figure 4.3: The friction velocity averaged over one half period, using both a fixed and a moving ripple for a wave plus current situation with $U_c/U_m = 0.5$ and $D/a = 5.0$.

convenient to look at the curl of the velocity field. Since the turbulence model only operates with the averaged velocity field, this is not the true vorticity, but rather the vorticity of the averaged velocity field. Nevertheless, this quantity is excellent for visualising the vortices in the flow.

The snapshots in figure 4.4 clearly reveal the formation of the separation bubble very early in the wave period. The bubble posses a very strong rotation, with velocities near the bed reaching values comparable to the free stream velocity. The bubble grows quickly from the crest of the ripple, and reaches the maximum length shortly after the outer flow begins to decelerate, around $\omega t = 150\,°$. At this point the length of the bubble is a little less than a. When the flow decelerates, the bubble is "curling up" into the main flow, but still maintaining the strong rotation. Shortly after the main flow has reversed, the bubble is lifted over the crest and ejected into the flow, thus becoming a free vortex ($\omega t = 30\,°$). It is hard to see the ejected vortex in the vector plots, where it just manifests itself as a fluctuation in the velocity field, but on the plots of the average vorticity it is evident. The vortex travels far over the ripple, and when the flow reverses again it has travelled almost

Figure 4.4: (facing page) The flow over a fixed ripple at six instants during the first half of the wave period. To the right is shown a vector plot of the velocity field, and to the left the curl of the velocity field. Clockwise rotation is red and anti clockwise rotation is blue. The contours have been cut short in areas of very high "vorticity", and these are the blank areas in the middle of the separation bubble.

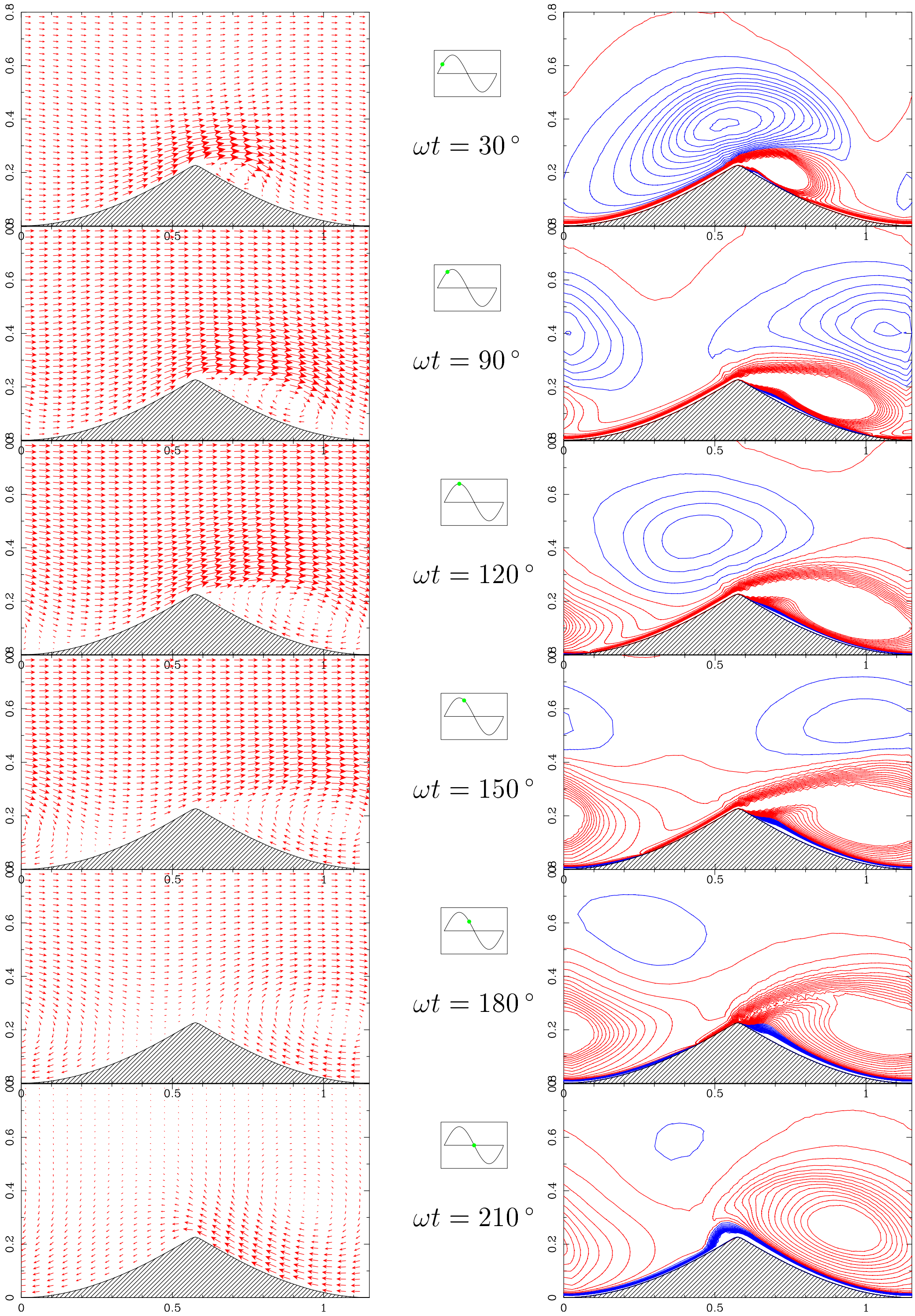
ωt = 30 °
ωt = 90 °
ωt = 120 °
ωt = 150 °
ωt = 180 °
ωt = 210 °

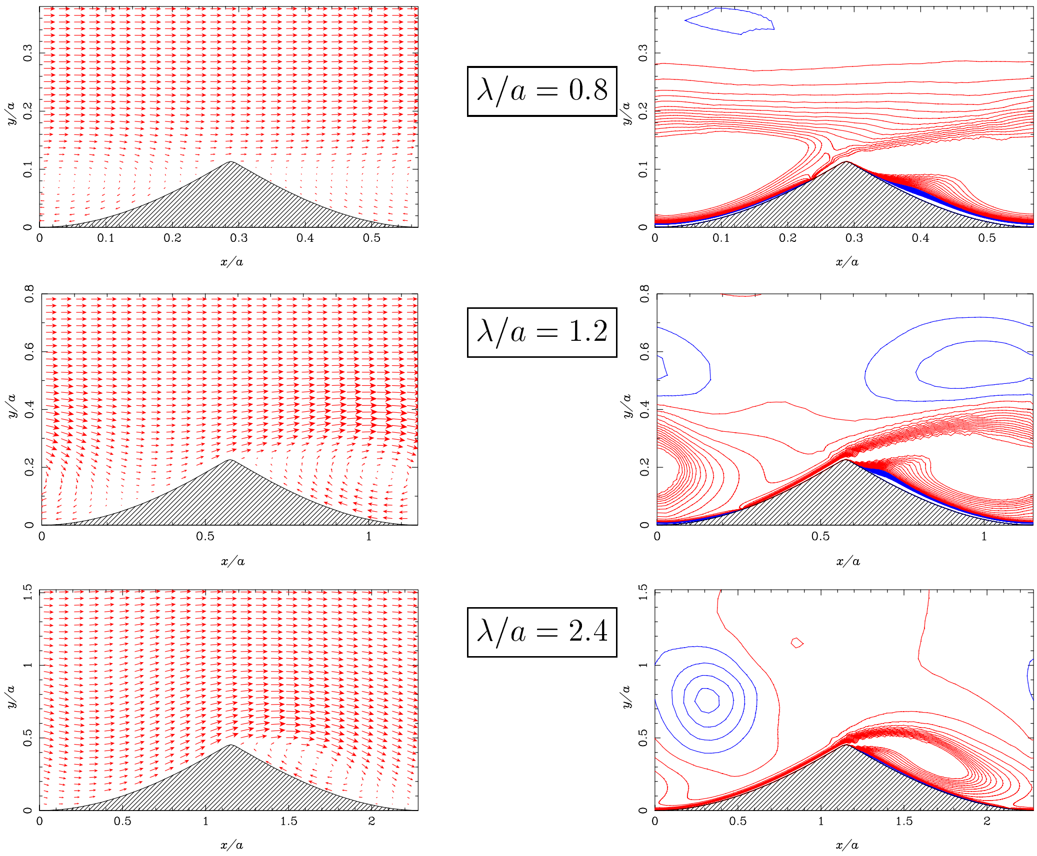

Figure 4.5: The flow at $\omega t = 120^\circ$ for a the wave only situation, but with $\lambda/a = 0.6$ (top), $\lambda/a = 1.2$ (middle) and $\lambda/a = 2.4$ (bottom). The legend is as in figure 4.4.

two ripple lengths, or more than two times a. When the next vortex is shed into the flow, the previously ejected vortex is almost dissipated.

The maximum extent of the separation bubble is quite an important topic, because the vortex is responsible for eroding the neighbouring ripples. If the separation bubble does not extend far enough to reach the neighbouring ripple, there is not much interaction. On the other hand if the separation bubble reaches over most of the next ripple, a lot of sediment will be eroded away. The dynamics of the sediment transport will be further elaborated in chapter 5 and 6. In figure 4.5 a snapshot is shown at the time of the maximum extent of the separation bubble for three different ripple lengths, $\lambda/a = 0.6$, 1.2 and 2.4. The intermediate length is the same as has already been shown in figure 4.4. For the shorter ripple, the separation bubble extends over the full length of the ripple and almost reaches the crest of the next ripple. Furthermore the rotation of the bubble is not nearly as strong as for the longer ripples. This is similar to the situation in steady flow, which does not lead to strong rotation in the separation bubble. It can then be concluded that the separation bubble for the very short ripple has finished the first transient stage where it grows, and has reached a steady state.

For the very long ripple ($\lambda/a = 2.4$) the separation bubble does not even reach the trough of the ripple. It is still as strong as the bubble created for the medium-length ripple.

4.2.2 The evolution of the separation bubble

For the sediment transport a most important quantity is the shear stress on the bed. The bed load transport is a function of the shear stress and the bed slope only, and the shear stress also determines the bed boundary condition for the suspended load. The shear stress on the bed can be seen as the "finger-print" of the flow above the bed. Especially the separation bubble is clearly visible in the shear stress profile. The shear stress is not everything, though, for instance the advected vortices are only dimly visible in the shear stress, and they too have some importance for the suspended load.

In figure 4.6 space-time plots of the shear stress on the bed are shown for a short ripple ($\lambda/a = 0.6$), a medium length ripple ($\lambda/a = 1.2$) and a long ripple ($\lambda/a = 2.0$). It is clear how the separation bubble is created at $\omega t = 0^\circ$ moves away from the crest with time. For the short ripple, the bubble extends all over the ripple at the end of the first half period ($\omega t = 150^\circ$), while for the long ripple, the bubble covers at most half of the ripple. The bubble being thrown over the crest around $\omega t \approx 200^\circ$ is seen as an increase in the shear stress (the points marked with an "A" in figure 4.6). Later, when the vortex has travelled one ripple length, and passes the crest again, a similar increase is seen ("B"). This is not seen for the longest ripple because the vortex does not travel far enough to reach the crest a second time.

Another important characteristic of the separation bubble is that there is a pronounced maximum in the shear stress, approximately halfway between the separation point and the reattachment point. The shear stress here is strong, around two times the shear stress on a flat bed. For the short ripple this maximum becomes much less pronounced at the end of the half period, while it is still evident for the medium and the long ripple.

More insight into the effective shear stress on the bed can be gained by averaging over a half or a whole wave period (figure 4.7). On average there is a very strong shear stress directed towards the crest of the ripple. This stress produces a net current of bed load towards the crest, and is responsible for the creation and the maintenance of the ripple. From both the averages over the half and the whole period the previous observation about the short

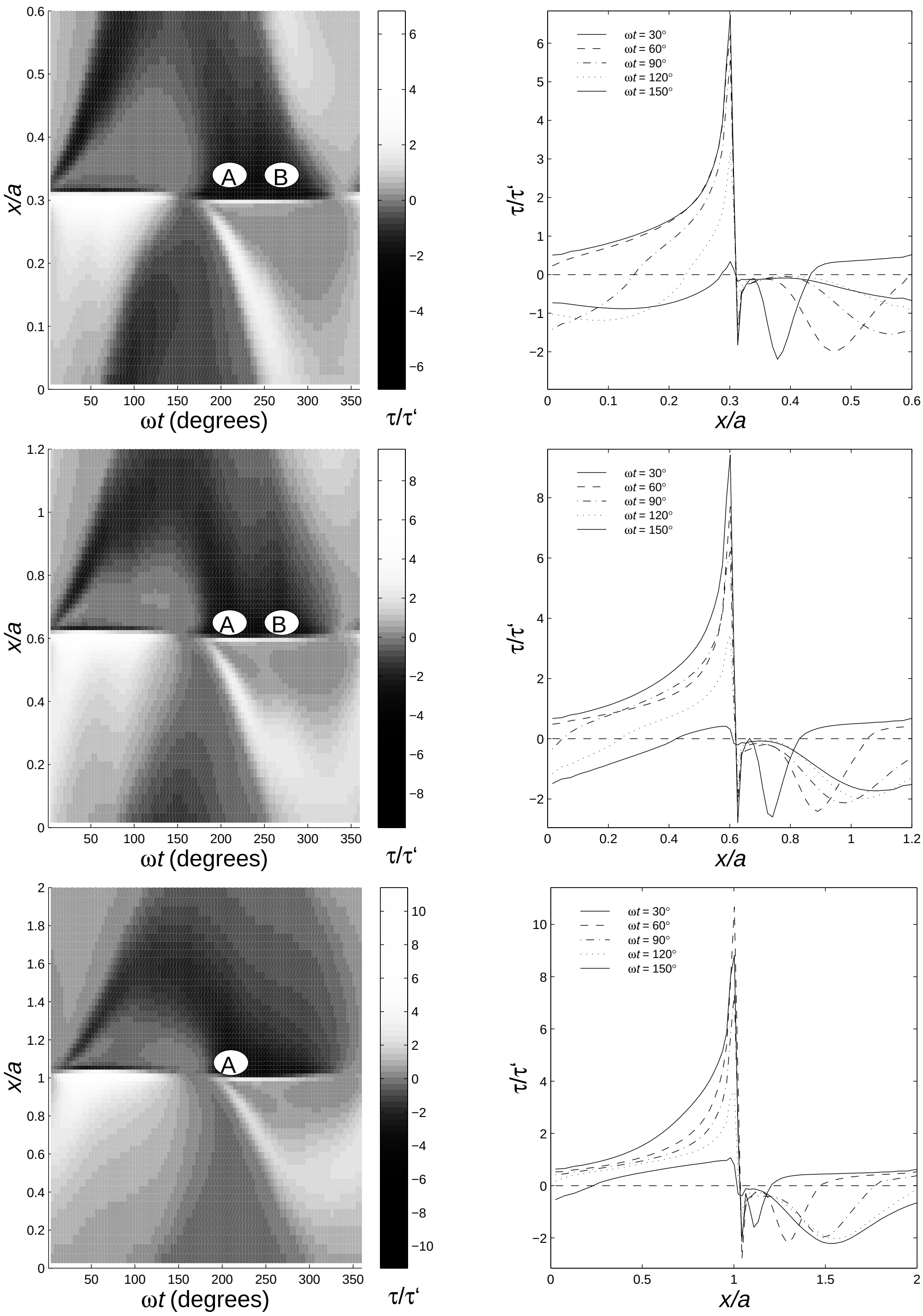

Figure 4.6: The shear stress on the bed divided by the maximum shear stress on a flat bed τ' for different lengths of the ripple: $\lambda/a = 0.6$ (top), $\lambda/a = 1.2$ (middle) and $\lambda/a = 2.0$ (bottom).

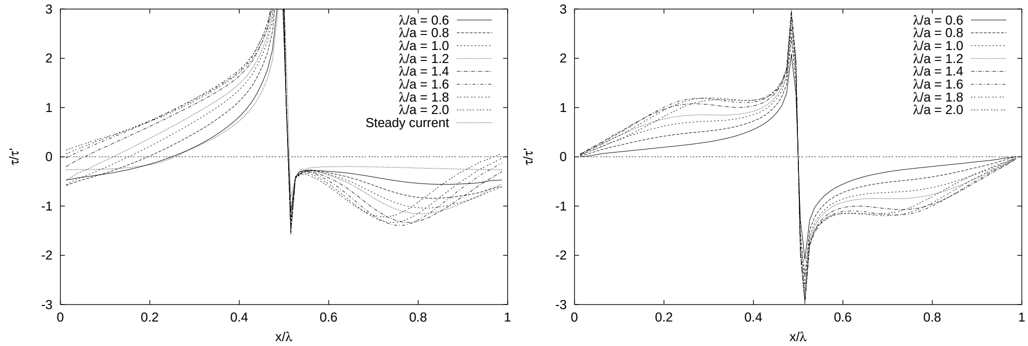

Figure 4.7: The shear stress on the bed averaged over the first half period (left) and the whole period (right) for λ/a ranging from 0.6 to 2.0. The crest is located at $x/a = 0.5$. The profile for steady current included on the left plot is made using $D = 12.5h$ $(h/\lambda = 0.2)$.

ripple having a smaller and weaker separation bubble is evident.

For the short ripples the expansion of the separation bubble is blocked by the neighbouring ripple. This blocks the evolution of the separation bubble, and the separation bubble then behaves more like the separation bubble in steady current (see figure 4.7). The steady current separation bubble is much weaker than the separation bubble in the transient regime when it is still expanding. It can be concluded that the maximum length of the separation bubble is the length of the separation bubble in the steady current regime, which is seen from the figure to be approximately 0.75λ.

The ripples longer than $1.4a$ seem to have the strongest separation bubbles. Only for $\lambda/a \leq 1.6$ does the separation bubble extend onto the neighbouring ripple. Then the bubbles seems to have grown to their maximum extent, but without reaching the next ripple. This means that the separation bubble will not be able to get any sediment from the neighbouring ripple using bed load. Consequently no interaction between the ripples takes place.

The results from the calculation of ripples with lengths between $\lambda/a = 0.3$ to 3.0, are summed up in figure 4.8. For the very short ripples $(\lambda/a < 0.6)$ the length of the separation bubble is equal to the length of the separation bubble in steady flow. The maximum extent of the separation bubble is reached at $\lambda/a \geq 2$, and corresponds to $\lambda_{sep} = a$. The point where the separation bubble is not able to cross the bottom of the trough is reached as seen before at $\lambda/a \geq 1.6$.

A final point is the shear stress in the trough between the two ripples (figure 4.9). There is a maximum in the shear stress in the trough when the

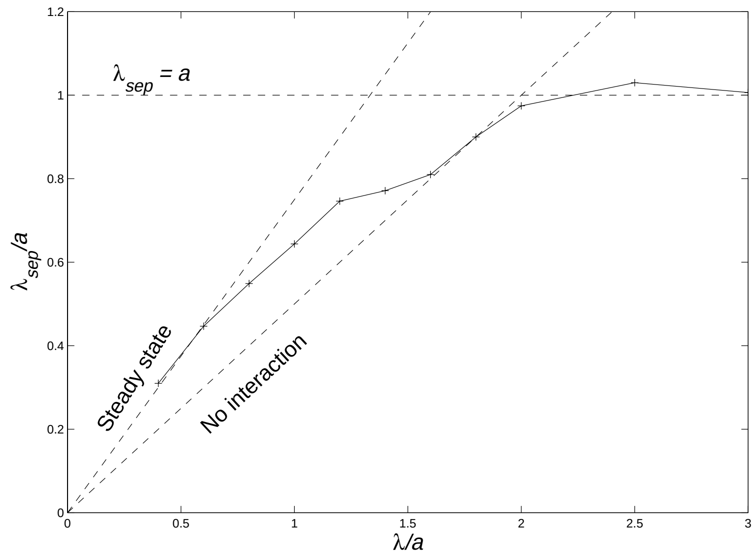

Figure 4.8: The position of the "reattachment point" in the shear stress averaged over one half wave period.The line labelled "steady state" corresponds to the length of the separation bubble in steady flow ($\approx 0.75\lambda$). The "no interaction" line is the position of the trough ($h/\lambda = 0.2$).

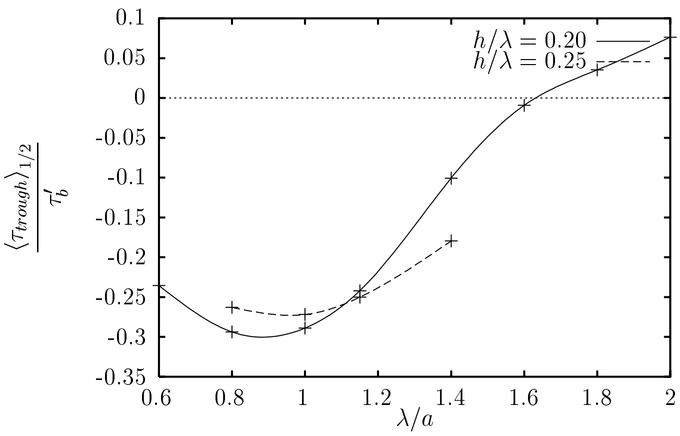

Figure 4.9: The shear stress in the trough averaged over a half period as a function of the ripple length. The line is an interpolation using cubic splines.

ripple length is around $\lambda/a = 1.1$. This has implications for the selection of wave length, a topic which will be elaborated upon later. The no-interaction limit is again found around $\lambda/a \simeq 1.75$.

4.3 Wave plus current flow conditions

The situation in the wave plus current case is somewhat more complicated, see figure 4.10 and 4.11. The flow here is similar to the basic simulations in the article, with the current vs. wave ratio (U_c/U_m) equal to one, i.e. a quite strong current. The amplitude of the motion can be split into two parts, one for each half period (a^+ and a^-). For this case a rough estimate gives $a^+ = 2a$ and $a^- = 0$. In the first half period, there is as expected a very strong free stream flow. The bubble which is created is very similar to the bubble created in the wave-only case, and the maximum extent is also the same. The last point is interesting, as the amplitude of motion for the positive half period a^+ is $2a$, and one could then expect the bubble to travel farther than in the wave-only case. In the second half period, the free stream flow is almost zero, but there is still a flow over the crest, partly created by the advected vortex from the first half period. This flow creates a separation bubble, but it does not extend as far as the bubble from the first half period.

In figure 4.12 a wave plus current situation with $U_c/U_m = 0.5$ is shown at the instant in each half period with maximum extent of the separation bubble. In this case, where the current is still quite strong, the situation is already much more symmetric, with the two bubbles having an almost equal maximum size. This indicates that the current probably has to be stronger than half the wave strength before any major reshaping of the ripples due to the current takes place.

As for the wave-only case, the maximum extent of the separation bubble has been examined. The extent in the first half period is labelled λ_{sep}^+ and in the second half period λ_{sep}^-. For a positive current it is clear that $\lambda_{sep}^+ > \lambda_{sep}^-$. A naive assumption for the extension of the separation bubble is

$$\lambda_{sep}^+ = \lambda_{sep}\left(1 + \frac{U_c}{U_m}\right) \tag{4.2}$$

$$\lambda_{sep}^- = \lambda_{sep}\left(1 - \frac{U_c}{U_m}\right), \tag{4.3}$$

where λ_{sep} is the length of the separation bubble in the wave-only case. That this assumption fails severely is seen in figure 4.13. In the positive half period the vortex is not able to grow much longer than in the wave-only case – for $U_c/U_m = 1$ the bubble is less than 20 % longer, and in the current-only case

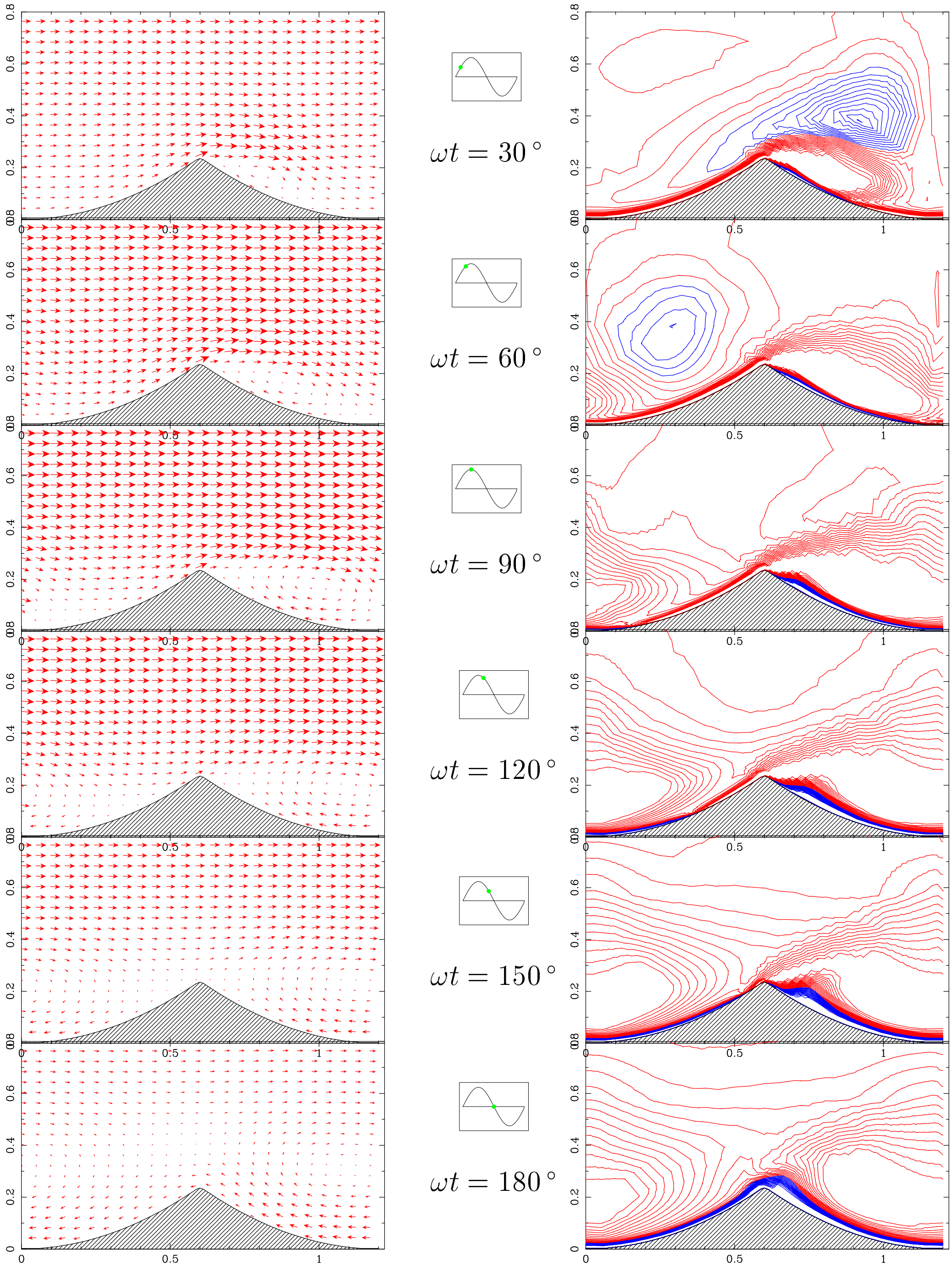

Figure 4.10: The flow in the first half period over a fixed ripples in wave plus current flow. The ratio between the wave- and the current strength is $U_c/U_m = 1$, and the depth over a is $D/a = 5.0$. The legend is as in figure 4.4.

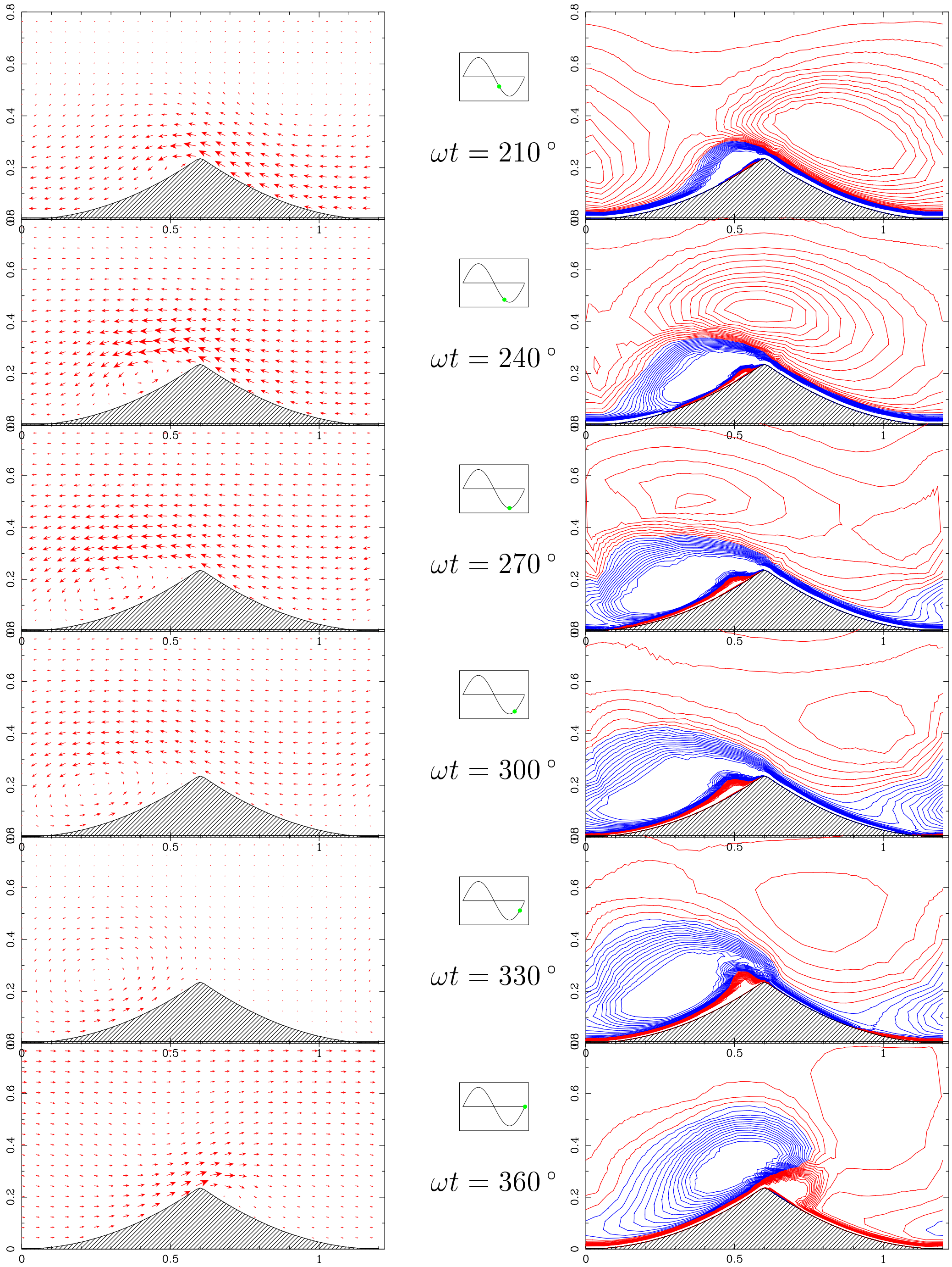

Figure 4.11: The flow in the second half period over a fixed ripple in wave plus current flow. The ratio between the wave- and the current strength is $U_c/U_m = 1$, and the depth over a is $D/a = 5.0$. The legend is as in figure 4.4.

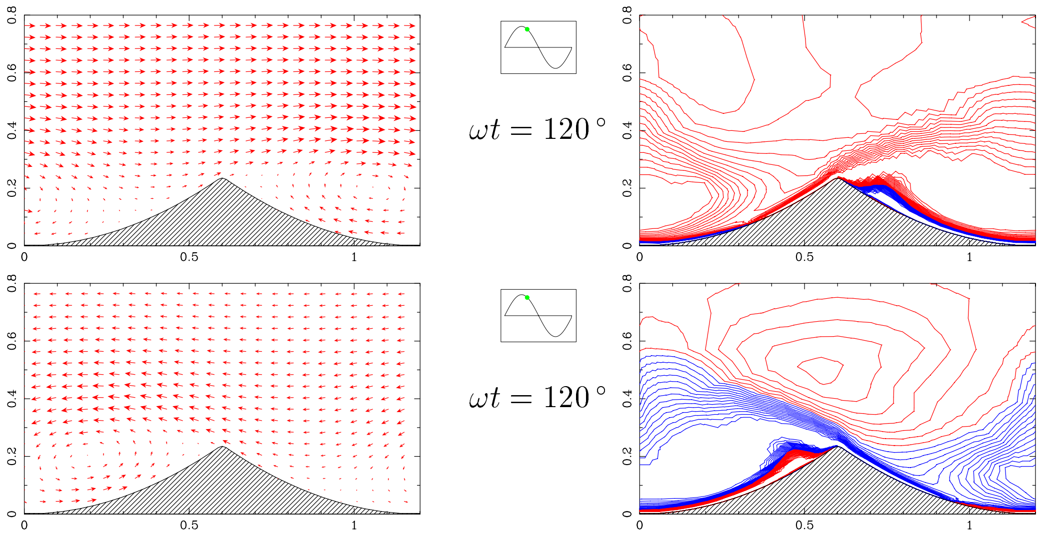

Figure 4.12: The flow at the two instants with the maximum extent of the separation bubble, for a wave plus current situation with $U_c/U_m = 0.5$ and $D/a = 5.0$. The legend is as in figure 4.4.

it is 25 % longer. This is because the expansion of the bubble is barred by the neighbouring ripple rather than by a. In the negative half period the bubble is shortened more than the bubble is lengthened in the positive half period. Still, for $U_c/U_m = 1$ where the naive assumption predicted that the bubble should disappear entirely, it is only 30 % shorter than in the wave only case.

These observation shows that the boundary layer generated by the ripple is very wave-dominated even though the depth-averaged current is strong. The reason is that even though the velocity averaged over the depth might be large compared to U_m, it is still small near the bed due to the logarithmic profile (figure 4.14).

4.4 Integrated flow quantities

In the wave plus current case the flow averaged over one period can be considered as an ordinary current flow having a logarithmic velocity profile

$$\frac{\langle U(y)\rangle_{x,t}}{\langle U_f\rangle_{x,t}} = \frac{1}{\kappa}\ln\left(\frac{30y}{k_{wc}}\right) \tag{4.4}$$

where k_{wc} is the Nikuradse equivalent roughness in a wave plus current flow. The averaged friction velocity (defined as $\langle U_f\rangle_{x,t} \equiv \sqrt{\langle \tau_b\rangle_{x,t}/\rho)}$ is usually

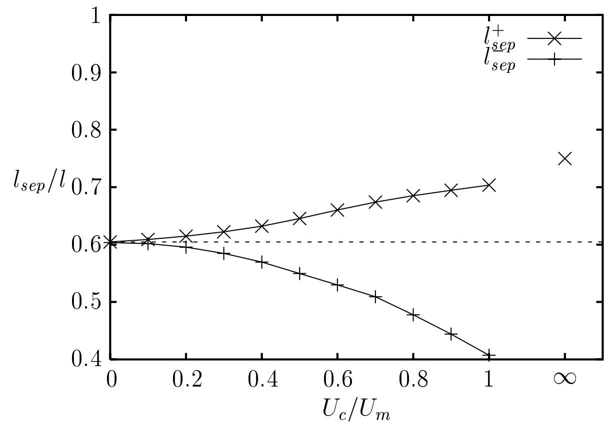

Figure 4.13: The length of the right separation bubble (λ_{sep}^+) and the left separation bubble (λ_{sep}^-) vs. the current strength. The point at $U_c/U_m = \int$ corresponds to the current-only case. ($\lambda/a = 1.2,\ h/\lambda = 0.2,\ D/a = 5.$). The runs have been made with a symmetric profile with $h/\lambda = 0.2$ and $D/a = 5$.

described via a constant friction factor defined as:

$$f_{wc} = 2\left(\frac{\langle U_f\rangle_{x,t}\, D}{Q}\right)^2 \tag{4.5}$$

with Q being the average flux.

That there really is a logarithmic profile is clearly seen in figure 4.14. Also shown is the variation of the profile which is suppressed due to the average over the ripple. This variation extends up to around $y = 5h$, and shows how far into the flow the influence from the ripples extends.

Finding the wave plus current friction factor f_{wc} and the roughness k_{wc} is one of the main objectives of the attached article ("Wave plus current over a ripple-covered bed"). In the following some work which was performed together with the article will be presented. This is some extra remarks concerning the friction over the ripples and calculations of the dissipation of surface waves due to the presence of ripples on the bed.

Finding the friction velocity

The friction induced by the ripples is composed of two parts: skin friction τ_s and form drag induced by the pressure. If $p(x,t)$ is the pressure on the bed and $\vec{t} = (t_x, t_y)$ is a unit vector tangential to the surface, the total friction is

$$\tau_b(x,t) = p(x,t)t_y + \tau_s(x,t)t_x, \tag{4.6}$$

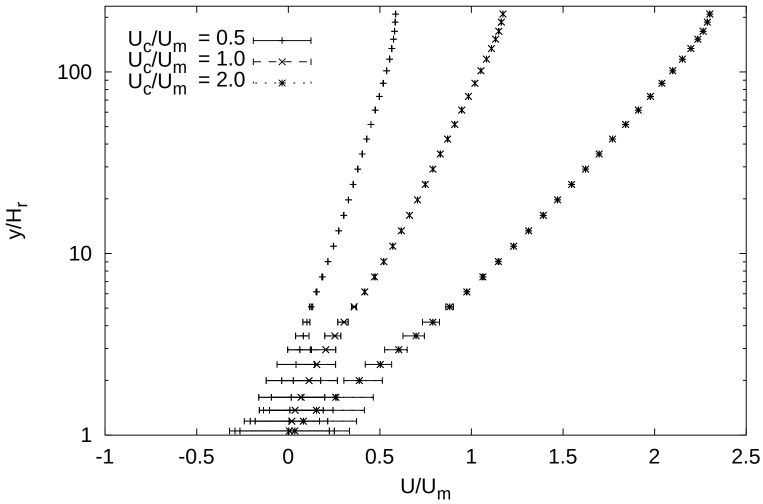

Figure 4.14: Profiles of the time and horizontally averaged velocity for simulations with $D = 250h$, $h/\lambda = 0.2$ and $\lambda/a = 1.2$. The error-bars show the min and max values of the time-averaged velocities, thus showing the amount of variation of the time-averaged velocity over the ripple. The lower edge of the plot is at the crest of the ripple.

which is averaged in space and time to give the total friction. As an alternative the total friction can be found from the driving pressure gradient:

$$\langle \tau_b \rangle_{x,t} = D \left\langle \frac{\partial p}{\partial x} \right\rangle_t . \tag{4.7}$$

The two estimates should be equal when the simulations have converged.

Because of the under-pressure created by the separation bubble, most of the friction is carried by the form drag (figure 4.15). This shall be seen in contrast to the friction over e.g. dunes in rivers, where the friction is partitioned approximately fifty-fifty between the skin friction and the form drag (Fredsøe and Deigaard, 1992). In the dune case the separation bubble is only a small fraction of the ripple length, and it is furthermore a steady separation bubble which is not nearly as strong as the separation bubble over the ripples (figure 4.8).

4.4.1 The dissipation

Another integrated flow quantity for the wave plus current case is the dissipation of the wave:

$$\epsilon_d = -\left\langle \langle \tau_b \rangle_x \langle U \rangle_{x,y} \right\rangle_t . \tag{4.8}$$

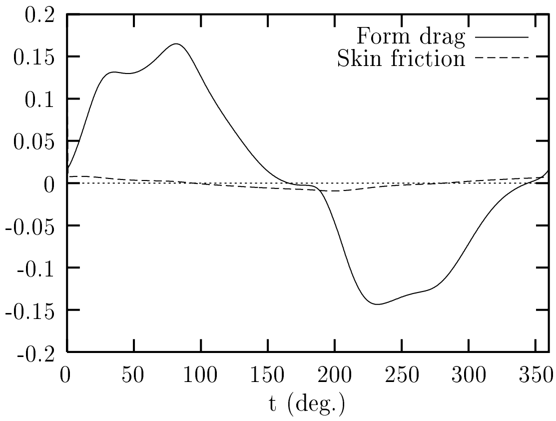

Figure 4.15: The skin friction and the form drag as a function of time over a ripple ($U_c/U_m = 0.5,\ D/a = 5.0,\ h/\lambda = 0.2,\ \lambda/a = 1.2$).

The dissipation is usually described via the dissipation factor f_e defined as[2]:

$$\epsilon_d = -\frac{2}{3\pi}\rho f_e U m^3. \tag{4.9}$$

A basic run has been chosen for the calculations. The length and the steepness of the ripples are $\lambda/a = 1.2$ and $h/\lambda = 0.2$. This is motivated by measurements of the ripple sizes. The depth is $25h$. From this basic run, each of the parameters is changed one at a time, while the others remain fixed. The steepness is varied from $h/\lambda = 0.05$ to 0.20, the length from $\lambda = 0.8$ to 1.8 and a run is made with a much larger depth, $D = 250h$. The results from the calculation of the dissipation are scaled with the wave-only dissipation f_{ew}, and are plotted in figure 4.16a-d.

The results are more scattered than the results for the friction, but one trend stands clear: for $U_c/U_m < 0.5$ the dissipation does not differ much from the wave-only dissipation, and if the steepness is 0.2 (which is the case for most fully developed vortex ripples), the dissipation is the wave-only dissipation up to $U_c/U_m \approx 1.0$. Changing the height produces drastic changes in the dissipation, which are more pronounced the lower the steepness. The reason is that the wave-only dissipation is very small for the small steepnesses (table 4.1), whereas the dissipation is less dependent upon steepness the stronger the current.

[2]Note that there exist different ways to define the dissipation factor in the literature, but the difference is only in the pre-factor.

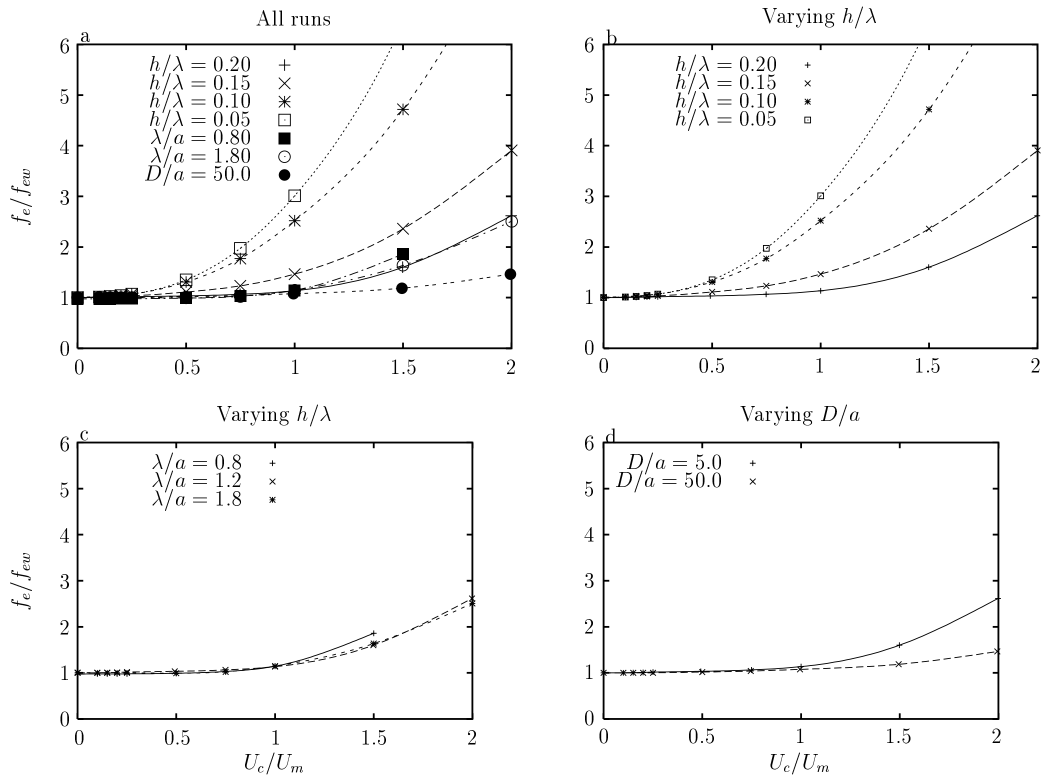

Figure 4.16: Variation of the wave plus current dissipation scaled by the wave-only dissipation (f_{ew}) as a function of U_c/U_m. a) all simulation data plotted together, b) varying h/λ, c) varying λ/a and d) varying D.

4.4.2 Comparison with "live" ripple

The results reported in the article and in the above section were made solely using fixed symmetric profiles. To examine the validity of the results of the calculations of f_c and f_e a comparison was made between a live ripple, a fixed asymmetric ripple and a symmetric ripple. The length of the ripple was $2a$ (figure 4.17). The results from the three runs are shown in table 4.2. Using the fit formula which was found in the article:

$$\frac{f_c}{f_{c0}} = \left(\frac{U_c}{U_m}\right)^{-0.66} + 0.73 \tag{4.10}$$

the relative friction f_c/f_{c0} where f_{c0} is the current-only friction can be found. The current-only friction for a steepness of $h/\lambda = 0.188$ (which was the steepness of the profile for the live ripple) can be estimated by an interpolation in figure A1.23 to be $f_{c0} = 0.0215$. To estimate the dissipation it was realized

Table 4.1: The wave-only dissipation.

Depth D/a	steepness H_r/L_r	length L_r/a	dissipation f_e
5.0	0.20	1.2	0.33293
	0.15		0.18556
	0.10		0.05492
	0.05		0.01975
	0.20	0.8	0.23377
	0.20	1.8	0.39508
50.0	0.20	1.2	0.32918

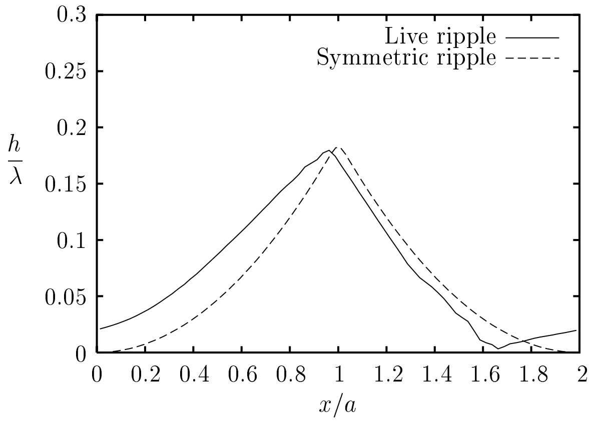

Figure 4.17: The shape of the ripple from the morphological calculation compared with a symmetric profile with the same steepness ($U_c/U_m = 0.5,\ \theta' = 0.15,\ w_s/U_m = 0.185$).

that for U_c/U_m the wave-current dissipation is similar to the wave-only friction (figure 4.16). The wave-only friction was then found from interpolations using the values in table 4.1.

For the friction the three different simulations are remarkably close. This is a very important result, as it adds of credibility to the results presented in the article, at least for current velocities smaller than $0.5U_m$. The value found by using formula (4.10) is slightly under-predicted. This has to be expected, though, as the steepness of the were less than 0.2, and it was shown in the article that the friction for steepnesses smaller than 0.20 were under-predicted by the formula.

The correspondence between the dissipation calculations seems to be se-

Table 4.2: The wave plus current friction factor f_c and the wave plus current dissipation f_e for three different types of simulations and using fits to the results presented in the article and in section 4.4.1.

	f_c	f_e
Live:	0.0069	0.082
Fixed:	0.0062	0.077
Symmetric:	0.0065	0.30
Fit:	0.0050	0.35

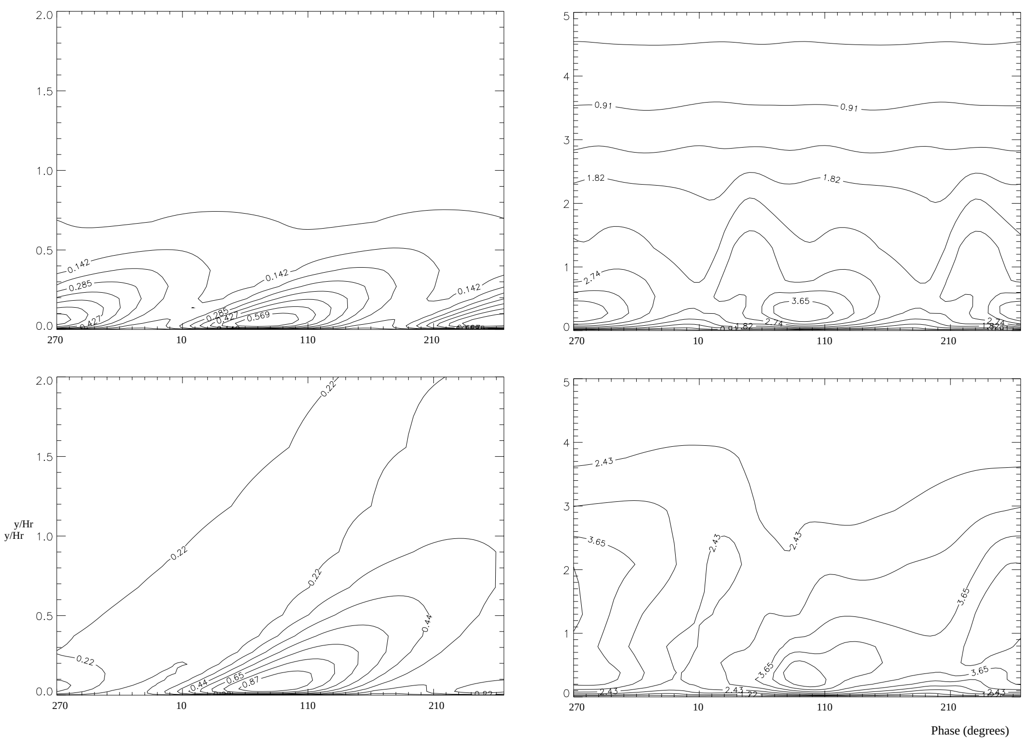

Figure 4.18: t-y diagrams of the space-averaged turbulent kinetic energy for pure waves (top) and waves plus current (bottom), with $U_c/U_m = 1$. To the left the calculation has been made on a flat bed, while on the right with ripples. On the flat bed the roughness has been arbitrarily set to $k_N = h$.

riously dependent upon the shape of the profile. There is a factor of four difference between the calculations on the asymmetric profile (live and fixed ripple) and the symmetric ripple. This means that the calculations of the dissipation should be used with care in an engineering situation.

4.5 Turbulent kinetic energy

As a post scriptum to the article where the friction and the roughness of a ripple bed are calculated, some of the limitations of such a description will here be shown. The idea behind using a roughness to represent the ripples is to be able to parameterise the effect of the ripples and just use a flat bed for the calculations. This is very desirable in calculations where the exact near-bed flow is of less importance.

That the near bed flow over a flat bed with a parameterised roughness is quite different from the near bed flow over a rippled bed is illustrated in figure 4.18. Here a spatial average of the turbulent kinetic energy k is presented and compared with the results from a simulation over a flat bed. The situation on the flat bed is dominated by turbulent diffusion. $\langle k \rangle_x$ forms a maximum near the bed when the wave crest passes (at $0\,°$and $90\,°$), which then diffuses outwards, seen as the tongue from left to right on figure 4.18, top left. For the ripple case, the situation is dominated by the advection of the vortices. The same maximum near the bed as in the flat bed case is seen, but this does not spread diffusively away from the bed, rather the primary vortex creating this maximum in $\langle k \rangle_x$ is thrown into the flow which makes the maximum away from the bed to be located in time exactly at the time where there was a minimum in the flat bed case.

The same thing is seen in the wave plus current case, only with the difference that there is no symmetry between the two halves of the wave period. It is also seen that the action of the vortices disappears a few ripple-heights away from the bottom, in consistency with what was seen on figure 4.14.

4.6 Summing up

The main results from this chapter can be summed up briefly:

- The flow over a live ripple is very similar to the flow over a fixed ripple.
- For $u_c/U_m < 0.5$ the flow is wave-only like.
- The transient separation bubble seen in the ripples is very strong compared to the separation bubble in steady current flow (a factor of 5 to 10 stronger).
- For $\lambda/a > 1.6$ the bubble does not extend over the trough.
- The maximum extent of the separation bubble can be approximated as $\lambda_{sep.max} \simeq \min(0.75\lambda, a)$.

- The main part of the friction on a ripple is carried by the pressure drag, and not by the skin friction.

Chapter 5

Sediment transport over ripples

The addition of sediment transport to the ripple problem introduces two new non-dimensional parameters: the Shields parameter and the settling velocity (see section 1.2). This makes a complete description of the whole phase space much more demanding. Another complicating fact is that the sediment transport is split into two partitions, bed load and suspended load, which have to be treated separately, because they are driven by different mechanisms.

The bed load is mainly a function of the local shear stress, and therefore a lot of the results from the analysis of the flow and the shear stress on the bed from section 4.2.2 directly gives the behaviour of the bed load.

For many cases, the suspended load carries the largest volume of sand, but a lot of this volume just stays in suspension and is advected back and forth. Therefore the horizontal gradients of the suspension are not very large, so the suspension does not contribute as much to the erosion/deposition of the ripple as could be expected from the volume of the transport.

In section 4.1.2 it was shown that the flow was the same over a fixed ripple and a live ripple. The same comparison is shown in figure 5.1, focusing on the sediment transport. Some difference is seen in the transport over the live and the fixed ripple, but the general pattern is the same, especially is the concentration of suspended sediment over the crest (5.1, right) the same for the live and the fixed ripple.

5.1 Four test cases

For the bed load the Shields parameter is the most important parameter. To illustrate the bed load under different conditions, two examples have been chosen: medium bed load rate, $\theta' = 0.15 \simeq 3\theta_c$ and high bed load rate,

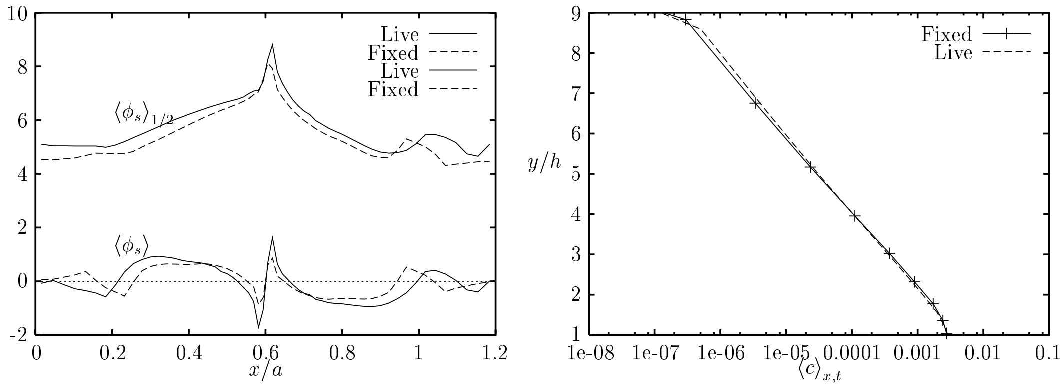

Figure 5.1: Comparison between the suspended sediment over a live and a fixed ripple. To the left is shown the averaged transport over one half period (top lines) and the whole period (bottom lines). The right figure shows the concentration of suspended sediment averaged over one wave period. ($\lambda/a = 1.2$, $\theta' = 0.15$, $w_s/U_m = 0.079$).

$\theta' = 0.50 \simeq 10\theta_c$.

The suspended transport is both a function of the Shields parameter and the settling velocity. The Shields parameter determines how much sediment is thrown into suspension via the bed boundary condition $c_b(\theta, \beta)$ (2.47). The settling velocity can roughly be said to determine how much sediment stays in suspension, and how far the suspended sediment is transported. Usually the Rouse parameter is used as a dimensionless parameter characterising the settling velocity:

$$R = \frac{w_s}{\kappa U_f}, \tag{5.1}$$

where κ is von Kármán's constant. The Rouse parameter enters naturally in the Vanoni distribution of suspended sediment over a flat bed in steady current:

$$c(z) = c_b(\theta)\left(\frac{D-z}{z}\frac{b}{D-b}\right)^R, \tag{5.2}$$

where b is the point where the matching of the bed boundary condition is made, usually $b = 2d$. It is seen that the larger the Rouse parameter, the more rapidly the concentration of sediment diminishes as the distance from the bed is increased. A small settling velocity then means that the sediment will reach further away from the bed. The shear stress enters two places in the expression for the Vanoni distribution: in the exponent, where higher shear stress has a the same effect as a small settling velocity, and in the bed

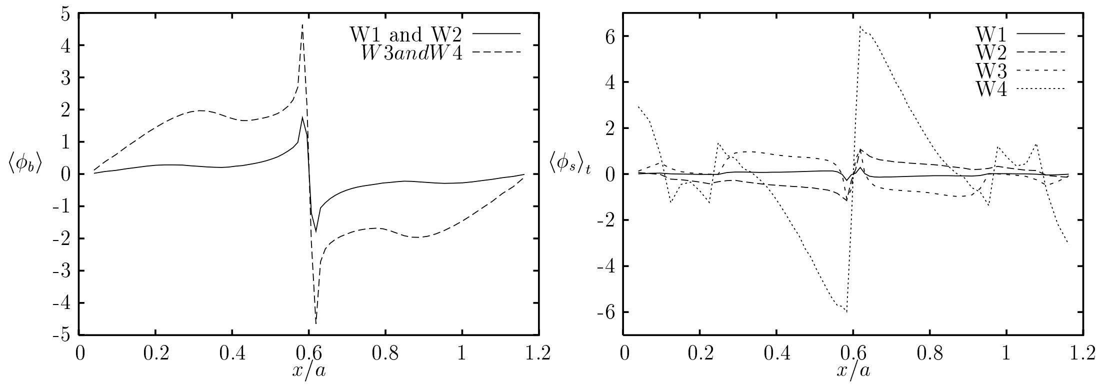

Figure 5.2: The sediment transport averaged over one wave period for the four test cases. Left: bed load, right: suspended load.

boundary condition, where a high shear stress will put more sediment into suspension. All in all, a small Rouse parameter gives more suspension.

In a wave flow there is not a log profile in average, and the Vanoni profile does not apply. Furthermore the averaged shear stress is zero, so another formulation than the one used in steady flow has to be used. One option is to use the maximum shear stress on the bed during the wave period (e.g. Fredsøe and Deigaard (1992)). This works fine on a flat bed, but for a rippled bed this is not obvious. The maximum shear stress will occur around the crest and is very sensitive towards the exact shape of the crest. It is therefore a "fragile" parameter, which should be avoided. The spatially averaged shear stress could be used instead, $U_{f.max} = \max(| \langle U_f \rangle_x |)$. The wave Rouse parameter is then:

$$R_w = \frac{w_s}{\kappa U_{f.max}}. \tag{5.3}$$

The problem is that it is hard to know before a simulation what $U_{f.max}$ will be, and it will depend on the geometry of the ripple. Therefore a simpler non-dimensional parameter, namely w_s/U_m is used to specify the settling velocity, and only after the simulation can R_w be calculated.

Two different settling velocities have been chosen to illustrate the effect of changing this parameter on the suspended transport, namely $w_s/U_m = 0.185$ and $w_s/U_m = 0.065$. As will be shown in chapter 6 this corresponds to two different regimes of ripples. The large settling velocity correspond to coarse sediment, on the order of 1 mm for realistic conditions.

With the two different values of the Shields parameter and the two different settling velocities, four different test cases have been constructed (table 5.1). For all four cases a fixed ripple profile is used with $\lambda/a = 1.2$ and

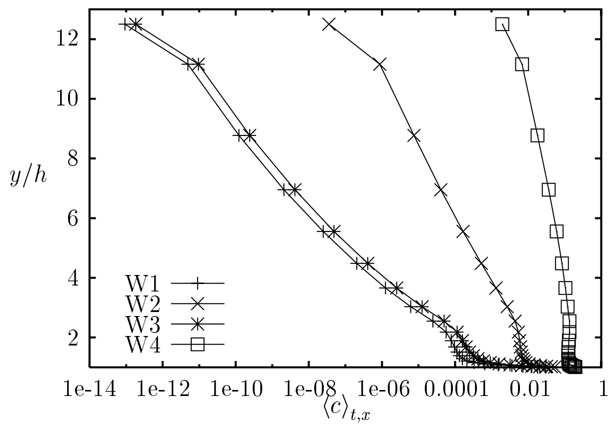

Figure 5.3: The time and space averaged concentration of suspended sediment.

$h/\lambda = 0.2$.

Table 5.1: The four test cases used for calculation of the sediment transport.

Test case	θ'	w_s/U_m	R_w
W1	0.15	0.185	0.82
W2	0.15	0.065	0.29
W3	0.50	0.185	0.82
W4	0.50	0.065	0.29

The time averaged bed load (figure 5.2, left) is qualitative similar for the two cases, although the amount of sediment transport is quite different. In general the bed load causes a transport which is directed towards the crest, i.e. maintaining and building up the ripple profile.

While interpreting the bed load transport it has to be remembered that in reality most of the ripple profile is at the angle of repose. This mean that the bed load in effect will be determined by avalanches, so that be bed load on a mature ripple will be directed down slope instead of up slope as seen here. In the trough, however, the bed load will be similar to the one shown here.

For test case W1 and W2 snapshots of the suspended sediment in the first half period (figure 5.4 and 5.5) show the large effect of changing the settling velocity. Even though the total amount of sediment in suspension is markedly different (see also figure 5.3) the general features are similar. A strong jet of sediment is thrown over the crest of the ripple, on top of the separation bubble. When the flow turns this jet follows the separation

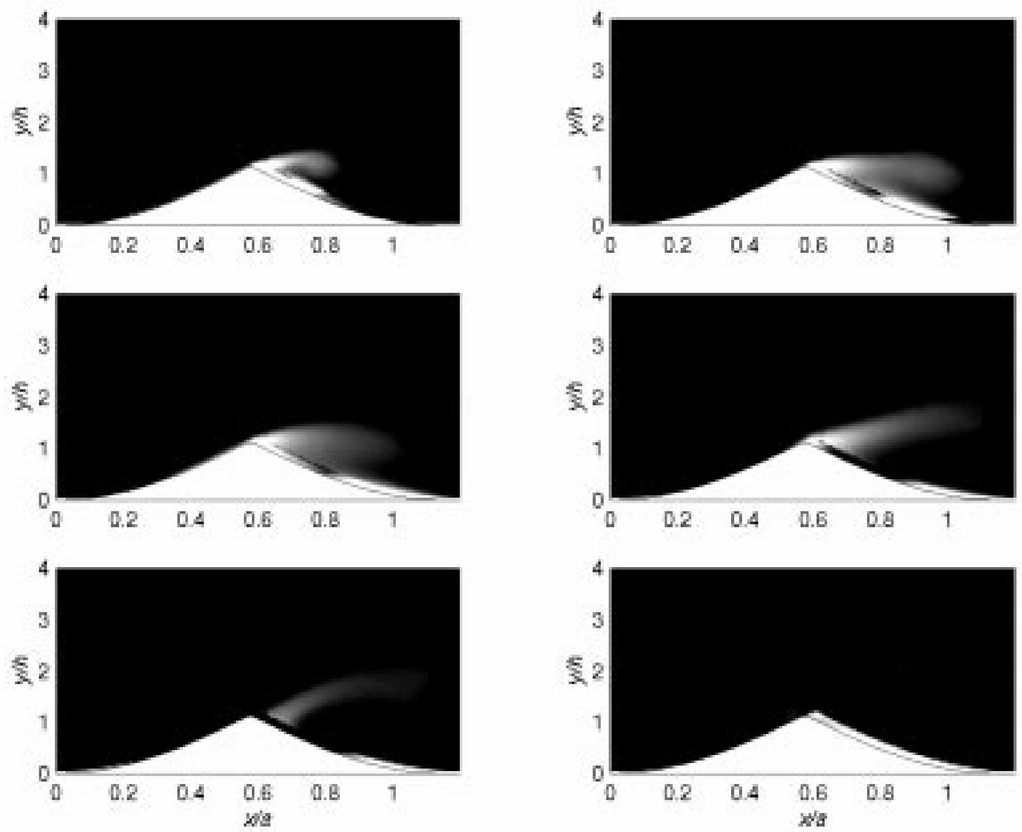

Figure 5.4: The transport of suspended sediment over a ripple at six snapshots ($\omega t = 30\,^\circ$ to $210\,^\circ$). The flow is the same as in figure 4.4. The scale show the log of the concentration of suspended sediment, the lighter the higher concentration of sediment (test case W2, $\lambda/a = 1.2$, $\theta' = 0.15$, $w_s/U_m = 0.185$).

bubble over the crest. In test case W1 the settling velocity is so large that the sediment settles almost immediately after this, while in test case W2 the cloud of sediment can be followed as it is advected with the flow. Another feature which is similar in both cases is the large concentrations of sediment which is seen close to the bed, particularly inside the separation bubble. This transport is dominating the total suspended load in test case W1, while the suspension in the jet dominates in test case W2. The suspended sediment in test case W1 can then be said to be more dominated by the local shear stress, almost like an extended bed load, while the transport is dominated by advection in test case W2. The two modes of suspension have been labelled the near-bed suspension and the advected suspension, respectively.

Another representation of the suspended sediment transport is to look at

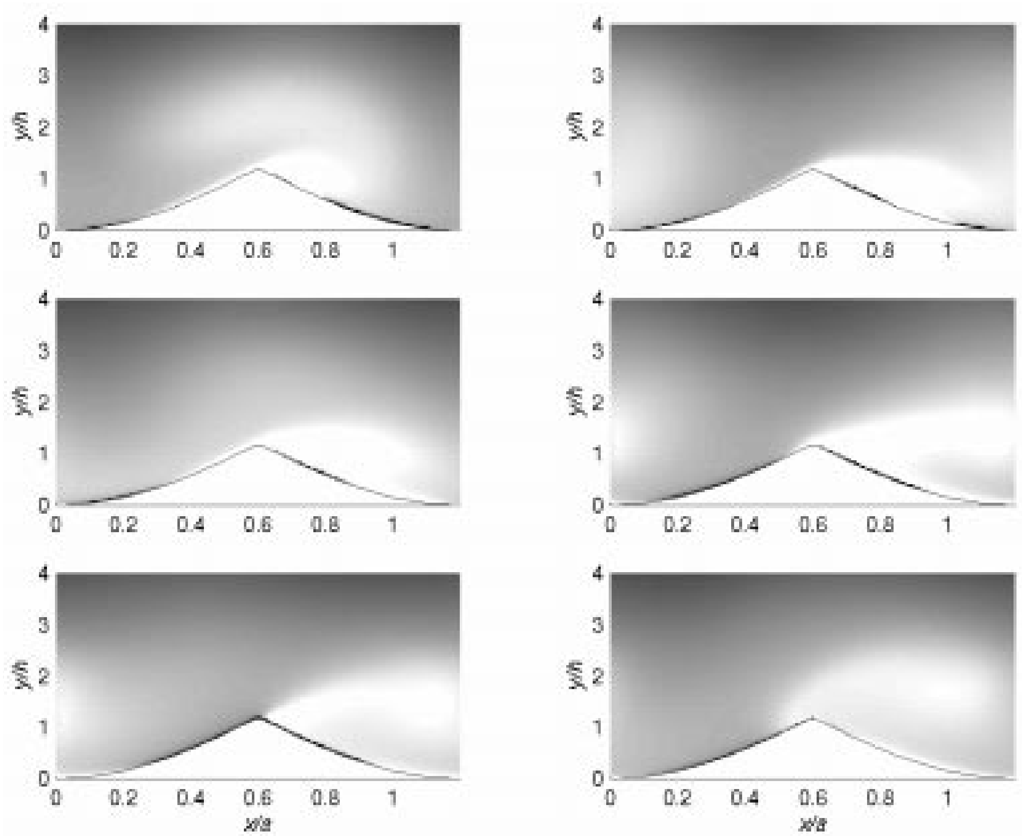

Figure 5.5: As figure 5.4, but with $w_s/U_m = 0.065$ (test case W1).

t-y plots of the transport through cross-sections at the trough and the crest (figure 5.6). Over the crest two maxima are observed, and when the figure is compared with figure 5.4 the events causing the maxima can be identified. The first maximum at $\omega t = 20\,^\circ$ occurs because the vortex from the previous half period is shed and advected over the crest. The second maximum is when the remains of this vortex return, after having been advected one ripple length. Near the bed high concentrations are evident at all times, except just near the point where the flow turns and c_b becomes zero. Two maxima are also seen over the trough. The first, around $\omega t = 60\,^\circ$, is mainly due to the advected vortex. The second maximum, at $\omega t \approx 125\,^\circ$, does not extend all the way to the bed. This maximum is due to the jet of sediment formed at the crest and thrown into suspension.

In the trough very low concentrations are seen until $\omega t = 100\,^\circ$, after which the bed concentration is generally high. The low concentrations occur before the separation bubble reaches the trough, where the shear stresses at

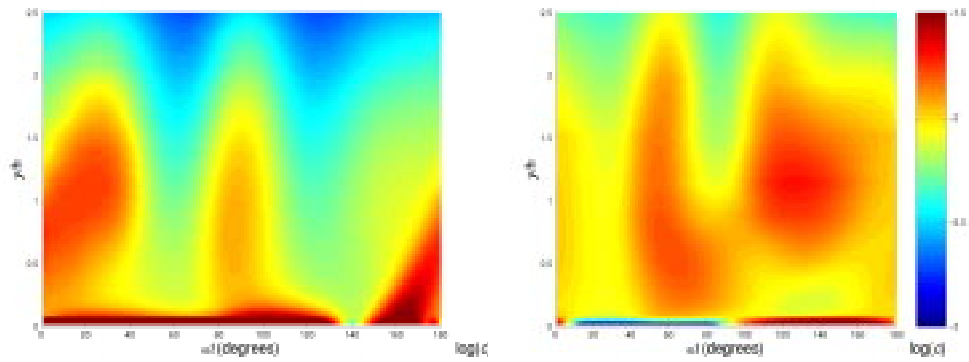

Figure 5.6: A t-y plot of the concentration of the suspended sediment over the crest (left) and the trough (right). The colour coding is made on $\log(c)$, (test case W2).

the bed are small giving rise to low bed concentrations. When the separation bubble has reached the trough it gives rise to negative shear stresses, and some sediment is diffusing into suspension. The layer of high concentrations is very thin, because the sediment has not had time to diffuse far away from the bed.

The suspended transport is markedly different for the test cases with different settling velocities. For W1 and W3 there is a high settling velocity, and the suspended sediment is confined to the area just above the bed, and is thus dominated by near-bed suspension. That is, the transport is directed towards the crest. Just around the crest the suspended load is directed away from the crest, which is due to the strong influence of the jet of sediment being throw over the crest just here. For the two test cases with small settling velocity (W2 and W4), the suspension is more dominated by the sediment in the jet, and is therefore mostly advected suspension. Here the time averaged suspended load is in general directed *away* from the crest, in contrast to the bed load, and there is only a small zone where the sediment is transported towards the crest.

5.2 Sediment transport in wave plus current situations

The sediment transport in wave plus current situation is even richer than the sediment transport under wave-only conditions. In waves alone the total transport is zero, but in wave plus current there is a net transport of sediment.

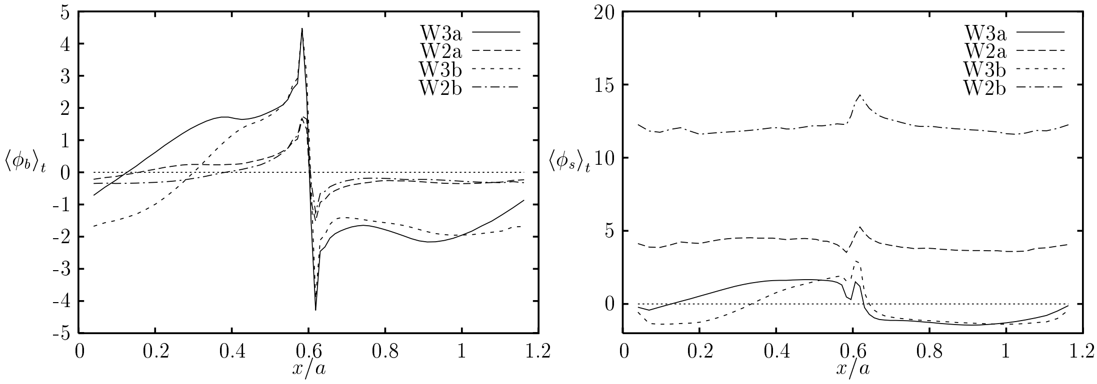

Figure 5.7: The sediment transport averaged over one wave period for the four test cases. Left: bed load, right: suspended load.

This can be either positive or negative, even when the superposed current is only positive.

In the wave only case the symbol θ' referred to the maximum Shields parameter on a flat bed. To be consistent this could be extended to the wave plus current situations, so that $\theta'_{wc} = \max(\theta'(t))$. This choice of definition of θ' is complicated by the absence of a simple way to determine the shear stress on a flat bed in wave plus current conditions. Therefore, for wave plus current situations, θ' will refer to the maximum shear stress on a flat bed in the corresponding wave case, where the simple method of the constant friction factor can be used.

First the sediment transport will be examined in detail for two of the test cases from the previous section with two different current velocities; $U_c/U_m =$ 0.5 and 1.0 for test case W2 and W3. Test case W3 has a high Shields parameter and a low settling velocity – this means a bed load dominated regime. Test case W2 has a low Shields parameter, and a small settling velocity – a suspension dominated regime. The flow in the two different situations is the same as the two wave plus current flow cases examined in detail in section 4.2.1 (see figure 4.10 and 4.11). Together with the two current velocities four test cases are again constructed (table 5.2).

At the low current velocity ($U_c/U_m = 0.5$), the profile of the time averaged bed load is almost symmetric (figure 5.7) for both test cases. For the high current velocity there is a considerable asymmetry in the bed load profile, reflecting the fact that the separation bubble at the lee side of the ripple extend much further than the separation bubble on the upstream side of the ripple. As a result of this, the ripple in the low current strength is expected to have only a slightly asymmetric profile, while there will be a considerable

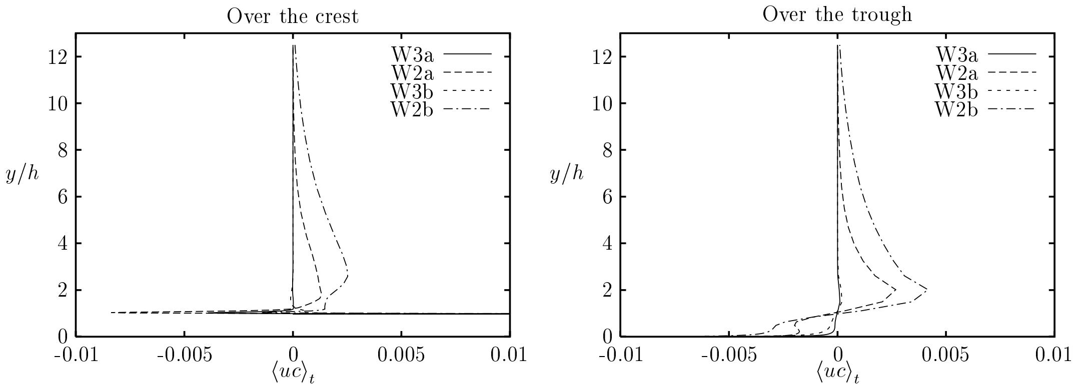

Figure 5.8: The flux of suspended sediment averaged over one wave period; $\langle uc \rangle_t$, over the crest (left) and the trough (right).

asymmetry at $U_c/U_m = 1.0$.

As seen in the previous section, the time-averaged suspended transport follows that of the bed load for test cases W3a and W3b. For test cases W2a and W2b there is seen to be a strong positive transport, around a factor of three larger for the strong current than for the low current strength. This transport is mainly because of the large amount of sediment being in constant suspension due to the low settling velocity. Where this sediment was “passive” in the wave-only case, it is now advected with the current, and contributes significantly to the total transport.

Looking at the time-averaged flux of suspended sediment over the crest and the trough (figure 5.8), an interesting detail is revealed. In the trough the flux of suspended transport is negative up to $y/h = 1$. This is not surprising, as the suspended transport here is dominated by the separation bubble. In a wave current situation (with positive current) the strength of the separation bubble in the positive half period will be stronger than the separation bubble in the negative half period. Thus there will be a net negative transport over the trough. This is similar for bed load which also gives rise to a negative transport over the trough. Above $y/h = 1$ the transport of suspended sediment is positive. For test cases W3a and W3b the transport here is almost zero, reflecting that no sediment extends very far away from the trough. Above the crest there is not surprisingly seen a strong positive transport just above the crest. What is more interesting is the negative transport seen just above the crest for the low current strength. This negative transport is made when the jet of sediment extending over the crest is thrown over the crest as the flow reverses.

The total transport rates are summed up in table 5.2. They show the

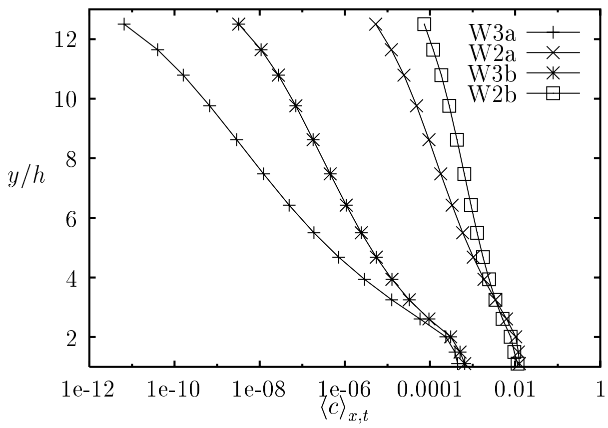

Figure 5.9: The time averaged concentration over the crest for the wave plus current test cases.

Table 5.2: The parameters for the four test cases for wave plus current flows, together with the resulting net transport rates. R_{fit} is the Rouse parameter calculated by fitting a Vanoni profile to the profile of the suspended sediment averaged over a wave period. The Rouse number R is calculated as $R = w_s/\kappa \langle U_f \rangle_{t,x}$

test	U_c/U_m	θ'	w_s/U_m	R	R_{fit}	$\langle \phi_b \rangle_{x,t}$	$\langle \phi_s \rangle_{x,t}$	$\langle \phi_{tot} \rangle_{x,t}$
W2a	0.5	0.15	0.065	1.6	1.8	-0.04	4.18	4.13
W3a	0.5	0.50	0.185	4.5	4.1	-0.23	0.06	-0.18
W2b	1.0	0.15	0.065	0.9	1.0	-0.07	12.28	12.19
W3b	1.0	0.50	0.185	2.6	2.5	-0.53	-0.20	-0.73

surprising fact that for all cases the total bed load is negative. For test case three the suspended transport is very small, and thus the bed load dominates, giving rise to a net negative sediment transport, even for a current strength of $U_c/U_m = 1$!. In test case two, on the other hand, the suspended sediment dominates clearly, and there is a strong positive sediment transport.

Away from the bed the flow develops a logarithmic layer (see figure 4.14), and the profile of the suspended sediment here behaves as in the current-only situation giving rise to a Vanoni-like profile with the difference that the bed boundary condition is different. The Rouse parameter is $R_{wc} = w_s/\kappa \langle U_f \rangle_{t,x}$. The profiles of suspended sediment can be seen in figure 5.9, and a comparison between the Rouse parameter calculated from the settling velocity and the mean friction velocity on the ripple with a Rouse parameter obtained by fitting the Vanoni profile in the region $3.75 < y/h < 10$ is seen in table 5.2.

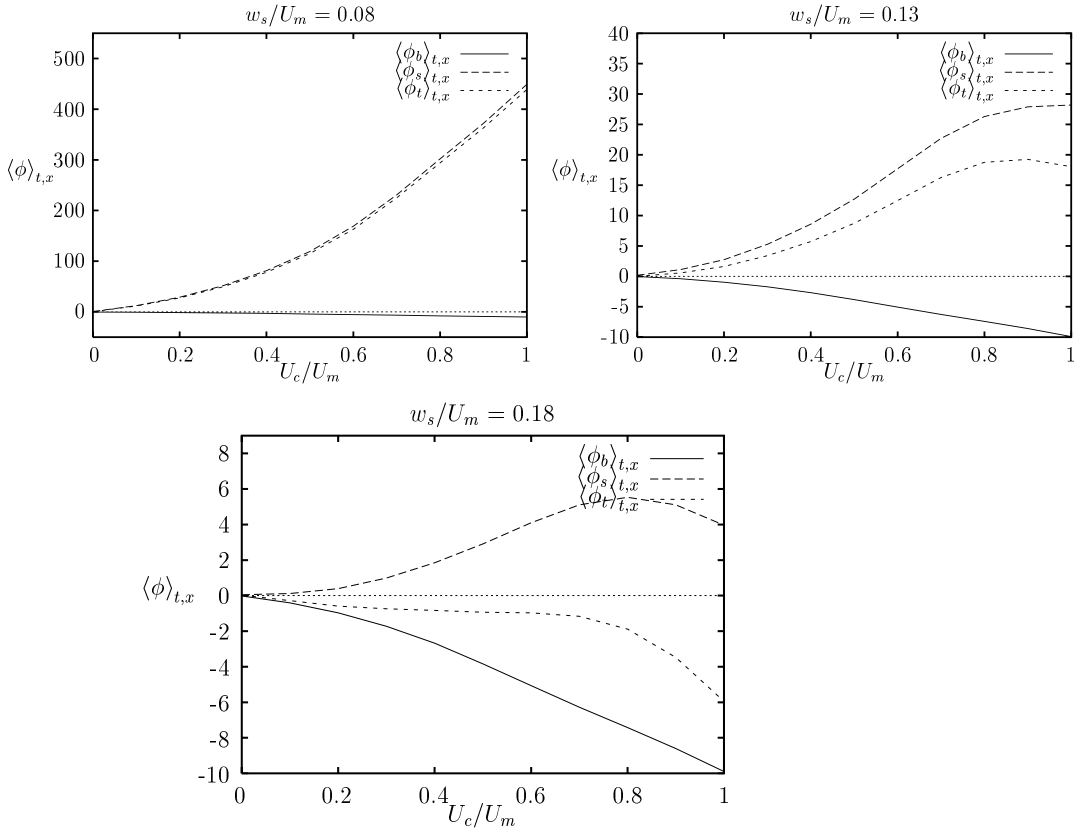

Figure 5.10: The time and space averaged sediment transport over ripples vs. the current strength, for three different settling velocities: $w_s/U_m = 0.08$ (top left), $w_s/U_m = 0.13$ (top right) and $w_s/U_m = 0.18$ (bottom left) ($\lambda/a = 1.2,\ h/\lambda = 0.20,\ \theta' = 0.23,\ D/a = 5.0$).

The agreement between the calculated and the fitted value is remarkably good, when the short range of logarithmic profile for this small depth is taken into account.

The same series of wave plus current runs as were examined in section 4.3 have been run with sediment transport. The Shields parameter is $\theta' = 0.23$ i.e. moderate bed load, and three settling velocities were used: $w_s/U_m = 0.08, 0.13$ and 0.18 (figure 5.10). The average bed load is negative, and almost linearly proportional to the current strength. The suspended transport on the other hand, is always positive. There seems to be a maximum in the suspended transport, located at $U_c/U_m = 0.8$ for $w_s/Um = 0.18$, at 1.0 for $w_s/U_m = 0.13$, and at a even higher current strength for the lowest settling velocity. With negative bed load and positive suspended load, the total load

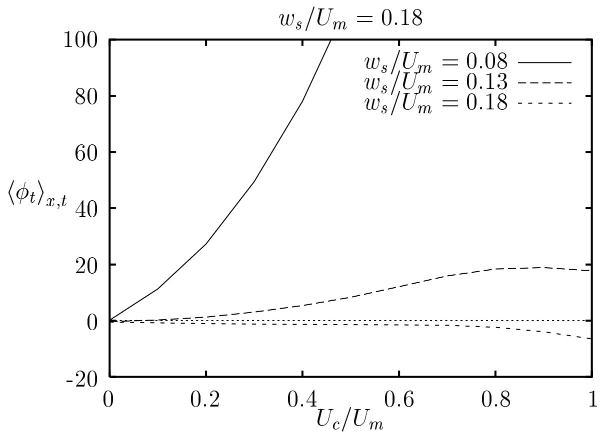

Figure 5.11: The total sediment transport for the three different settling velocities.

is determined by a balance between bed load and suspended load. For the highest settling velocity the negative bed load wins, and the total load is negative. For the lower settling velocities the suspension is stronger, and the total transport is positive.

5.3 Summing up

- The time-averaged bed load is directed from the trough towards the crest.
- The suspended load is much larger than the bed load (for most cases), but the time-averaged suspended load is generally smaller than the bed load.
- The time-averaged suspended load is dominated by the near-bed transport, except around the crest, where the time averaged bed load and suspended load are opposing each other.
- The net bed load is predominantly negative in wave plus current situations, while the suspended transport is positive.
- For small Rouse parameters the total sediment transport can be negative, even for $U_c/U_m = 1.0$.

Chapter 6

The dynamics of vortex ripples

Having dealt with the flow and sediment transport over predominantly fixed ripples in quite some detail, the attention will now be turned towards how the flow and the sediment transport shapes the rippled bed. Of particular interest is the question of the equilibrium length and shape of the ripples.

An outline of the chapter is as follows. After a review of existing measurements of the ripple geometry (section 6.1), the qualitative dynamics of the ripple profile will be illustrated using some long simulations of several ripples (section 6.2). The important processes here are the annihilation of ripples and the creation of new ripples. Hereafter a stability analysis of the fully developed profiles will be performed (section 6.3). This way it is possible to find the minimal wave length of the ripples (λ_m). It is shown that the important quantity in the dynamics of the ripples is the transfer of sediment over the trough of the ripples. This way it is argued that it is possible to calculate the minimal wave length using the sediment transport over just one fixed ripple by determining the transport over the trough as a function of the ripple length (section 6.4). This insight is used to construct a very simple model of the ripples, which shows the dynamics of a one dimensional ripple profile (section 6.5). Finally the shape of the ripples for different values of the Shields parameter and the settling velocity is calculated in section 6.6.

6.1 Measurements of ripple geometry

The first measurements of the length of the ripples was performed by Bagnold (1946) (he called the equilibrium wave length "the natural pitch"). Bagnolds major finding was that the ripple length was proportional to a for most cases, a result which has been confirmed several times since (for a compilation of measurements, see Nielsen (1979)). Most of these measurements are per-

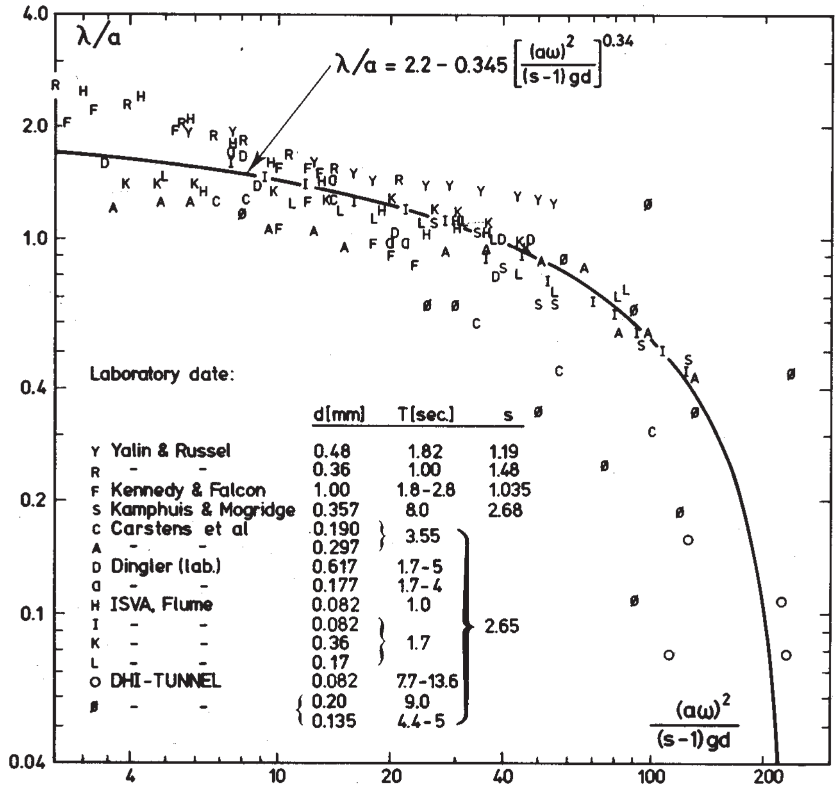

Figure 6.1: The average wavelength for a number of experiments, collected by Nielsen (1979).

formed in wave flumes or, as in Bagnolds case, in oscillated trays where the pattern is two-dimensional and defects are moving around.

The measurements of ripple lengths are not unambiguous, however. When a transect from a two-dimensional ripple pattern is extracted, it might cover a part of one or more defects, which will turn up as small ripples in the transect. If the ripple wave length is calculated as the number of ripples divided by the length of the transect, the defect(s) effectively make the apparent wave length shorter. Thus the wave length quoted by most authors is in fact a combined measurement of the *local* wave length and the density of defects. When they report that the wave length becomes shorter when the shear stress is increased, it is therefore not clear if the ripples actually become shorter, or if there are an increased number of defects. A simple way to circumvent this problem is to measure the distribution of local wave lengths, and define the ripple wave length as the most probable wave length. It is important to bear these points in mind, when experimental data are interpreted.

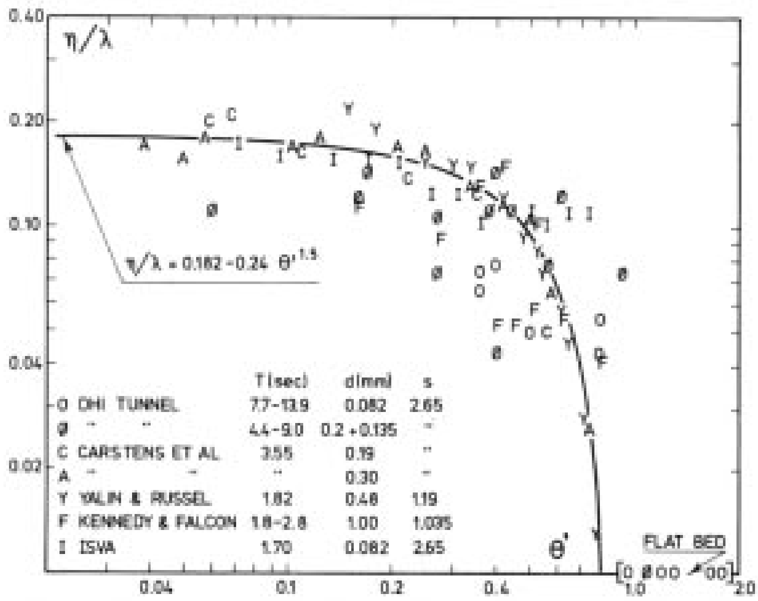

Figure 6.2: The average steepness for a number of experiments, collected by Nielsen (1979).

An important part of many of the studies of the ripple geometry was to identify the relevant non-dimensional parameters which described the experimental conditions best. As there was not a consensus on the parameter(s) to use, this lead to a situation where the results were reported using different phase spaces. Nielsen (1979, 1981) made a thorough compilation of all the measurements and transformed them to the same set of non-dimensional parameters. For laboratory waves he described the wave length as being a function of the mobility number:

$$\psi \equiv \frac{U_m^2}{(s-1)gd}. \tag{6.1}$$

Note that the mobility number is similar to the Shields parameter on a flat bed. The difference is that the Shields parameter takes the friction of the bed into account through the use of the friction velocity U_f instead of U_m. The results are not without a considerable scatter (figure 6.1), but they also compromise a large set of conditions. For mobility number less than approximately 30, the wave length is more or less proportional to a with a proportionality constant close to the commonly cited range between 1.2 and 1.4. For higher mobility numbers there is a considerable scatter in the data as the flat bed limit is approached. Whether this is a modification of the

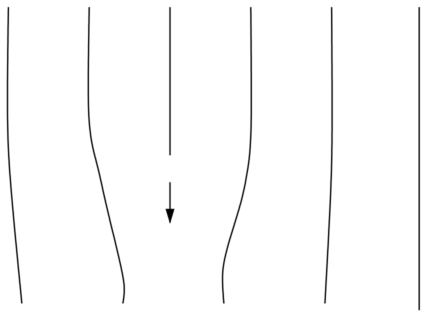

Figure 6.3: An example of the motion of a defect in a two-dimensional ripple pattern.

most probable wave length or it is due to an increase in the density of defects is not clear.

The steepness of the ripples (figure 6.2) were plotted as a function of the Shields parameter, θ'. similar pattern. For small values of θ', the steepness is slightly smaller than 0.20, and above $\theta' \approx 0.5$ it declines rapidly towards the flat bed limit.

It is not obvious that the is possible to use a one dimensional phase space to describe the wave length of the ripples as done by Nielsen. As it was argued earlier (section 1.2), the settling velocity should also be considered w_s/U_m.

Recently, a novel experimental setup has been employed to measure the wave length of the ripples (Stegner and Wesfreid, 1998; Scherer *et al.*, 1999). This consists of a circular channel which is driven by an AC motor. In this way a one-dimensional pattern is created, without end-effects and with conservation of the sand. Using this setup Stegner (1998) found the wave length to be proportional to a up to $\theta' = 0.23$ and $\psi = 26$. The minimal settling velocity was $w_s/U_m = 0.07$. For larger shear stresses the wave length became longer, a result which was attributed to the effect of inertial forces on the grains. These measurements have another problem, namely that there is an uncertainty on the measurements associated with the periodic nature of the bed. The uncertainty is $\Delta\lambda = \lambda/N$ where N is the number of ripples. As this experiment was rather small, the uncertainty was 20 % for the largest shear stress.

6.2 Qualitative dynamics of the ripples

The main limitation of the present model is that it is only handles one-dimensional ripple profiles. The one-dimensional case differs from the two-dimensional case in one important aspect, namely by the rôle of the defects. In most cases a two-dimensional profile has defects which are responsible for the wave length adjustment of the ripples (see e.g. figure 1.2). Consider a ripple profile where the wave length is a bit longer than the minimal wave length. Then there is in principle room for another ripple if the ripples squeeze a bit closer together (the “Tokyo metro”-effect). In that case a defect can move into that particular region of the bed and thereby adjust the wave length towards the equilibrium wave length (figure 6.3).

In the one-dimensional case the ripples have to create the new ripples themselves, so to speak. If the profile is homogeneous, i.e., all the ripples have the same length, a creation of a new ripple can only happen by a spatial period-doubling where all the ripples nucleate a new ripple simultaneously. After the period-doubling there can be some dynamics which in the end might lead to a state closer to equilibrium. However, the period-doubling only happens when the profile is quite far away from its equilibrium length, depending on the Shields parameter and the settling velocity. Thus the one-dimensional profile may be locked in a state of frustration from which it can not escape. In two-dimensions the wave length may be adjusted with the aid of defects.

A major problem with morphological calculations is that they can only be made with an integer number of ripples in the computational domain. As the calculations are very demanding in terms of CPU time, it is only possible to have a few ripples in the domain. Therefore the selected wave length can not just be found by making one big calculation and see what wave length is selected in the end – more elaborate arguments will have to be developed.

Before moving to the more detailed treatment some results from the morphological runs of the model are presented. The aim is to illustrate some of the basic dynamical phenomena occurring in the ripple profiles.

Creation

In figure 6.4 an example of the creation of ripples is shown. The simulation has been initiated with two ripples, which are obviously too long and too high. A period-doubling takes place in both troughs. In fact one trough is so wide that there is room for one extra new ripple in addition to the one created by the period-doubling. The initial dynamics is fast, but as the profile becomes more homogeneous the dynamics slow down.

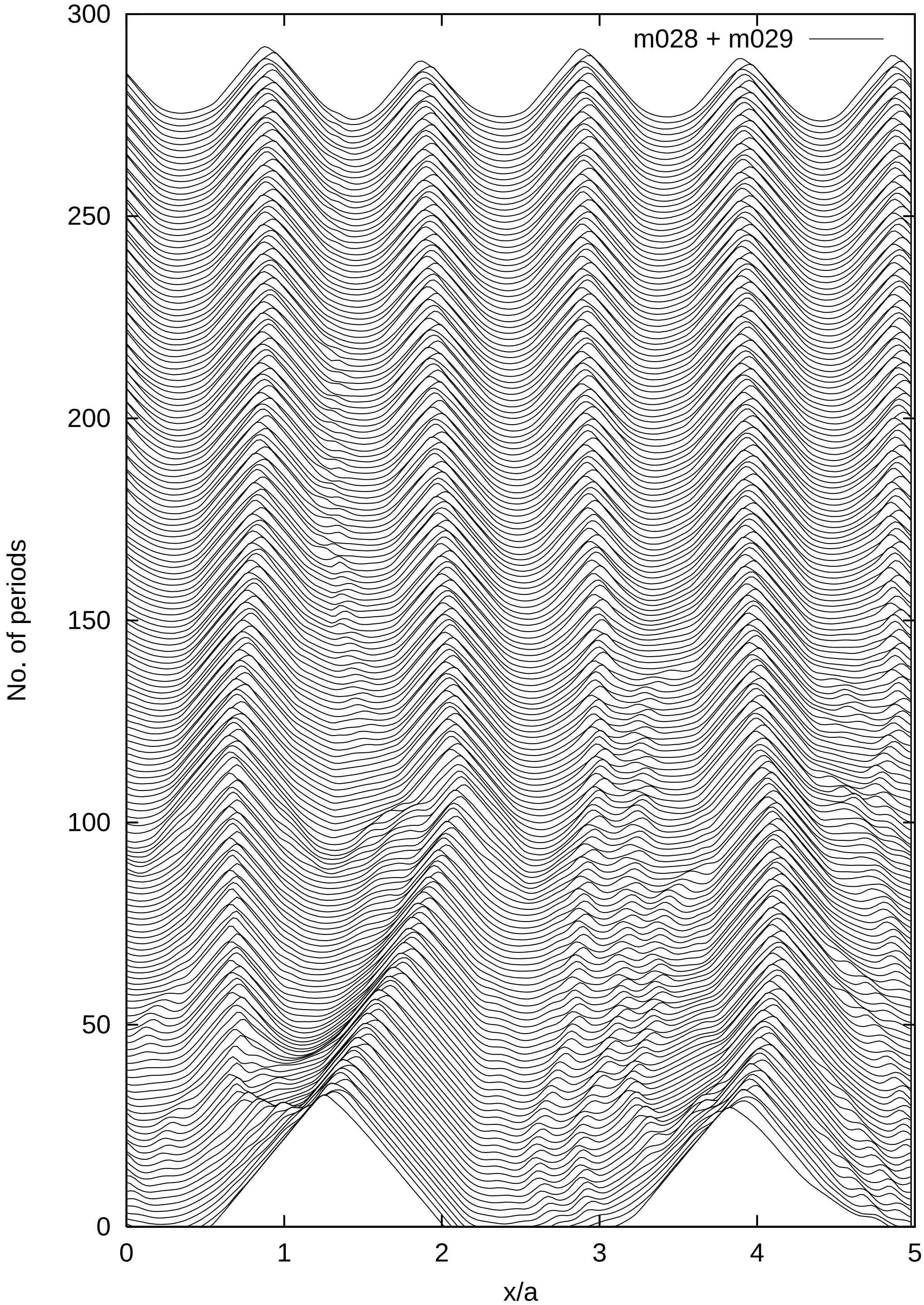

Figure 6.4: The evolution of a ripple profile over long time, showing the creation of new ripples. The profile is drawn several time each period so the movement of the crest is visible ($\theta' = 0.15,\ w_s/U_m = 0.070$).

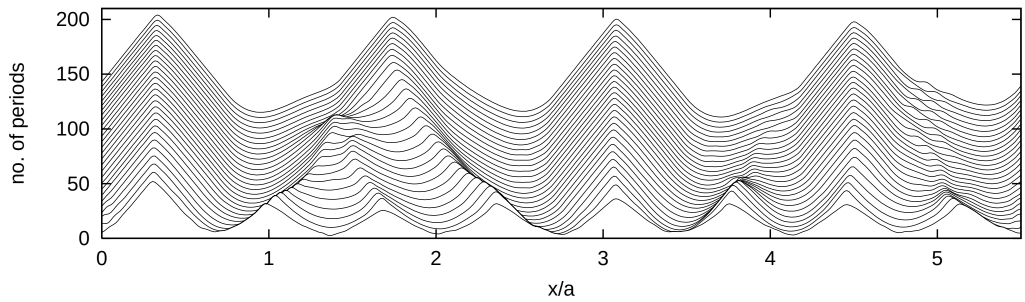

Figure 6.5: The evolution of a ripple profile showing the process of annihilation ($\theta' = 0.15,\ w_s/U_m = 0.070$).

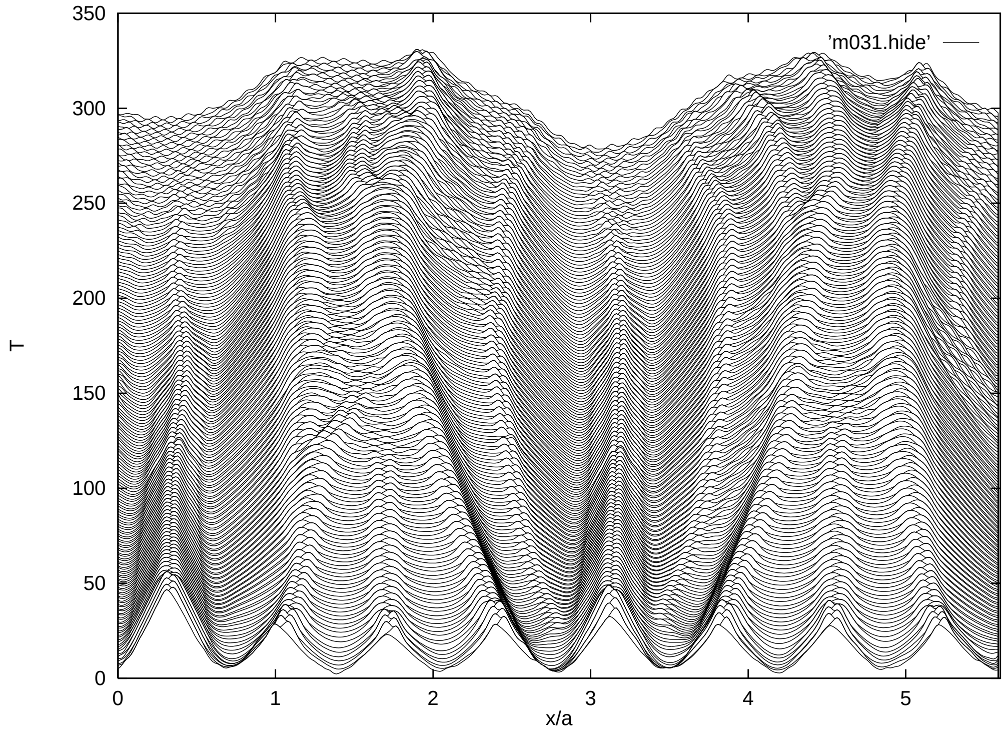

Figure 6.6: The evolution of a ripple profile showing the dynamics for a case with a small settling velocity. The profiles are drawn every half period ($\theta' = 0.15,\ w_s/U_m = 0.030$).

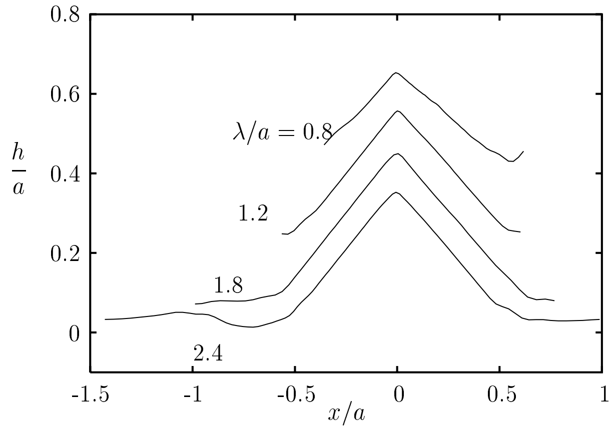

Figure 6.7: The equilibrium profiles for ripples varying lengths. The profile with $\lambda/a = 2.4$ is not in equilibrium – the flat piece develops into a new ripple (test case W1).

Annihilation

An example of annihilation is shown in figure 6.5. Generally every second ripple is just annihilated, but during the creation of the second of the final ripples (as counted from the left side) some interesting dynamics occur. Here three small ripples are competing to become the final, big ripple. Due to symmetry the middle ripple should have the best chances to win, but eventually it is dominated by its neighbour, which moves in to become the final ripple.

Small settling velocity

As will be shown later a transition between long and short ripples exists around a settling velocity of $w_s/U_m = 0.070$, where the dynamics are dominated by the advected suspension (figure 6.6). The run is started as before with many small ripples. The ripples merge to form two large sinusoidal ripples with smaller ripples on top.

Strained ripples

If the ripple profile is one-dimensional, or if there is no defects in the two-dimensional profiles, which can happen for small Shields parameters, the ripple profile can be strained; the ripples are either shorter or longer than their equilibrium length. This can be observed when the ripples are confined to a limited domain, where there is only room for an integer number of ripple. Strained ripples were first described in the measurements by Lofquist

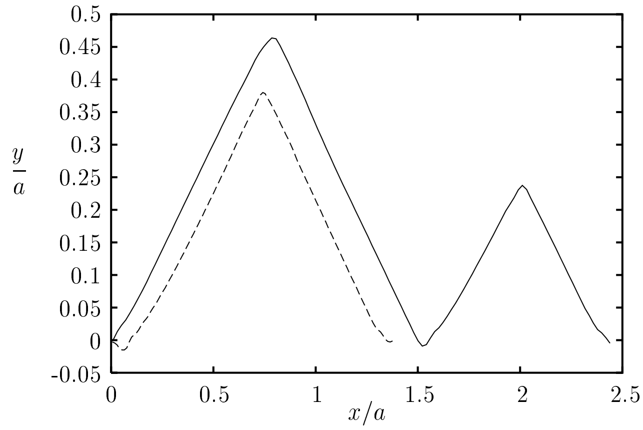

Figure 6.8: An example of the appearance of a period-two profile when the domain is larger than the equilibrium wave length, but smaller than two times the marginal wave length ($\theta' = 0.50,\ w_s/U_m = 0.10$).

(1980) (in an almost one-dimensional setup), who found that the lengths of the ripples could be varied between $\lambda/a = 1.1$ and 1.3. The straining of a profile with one ripple is seen in figure 6.7. In this case, where the Shields parameter is rather small, the profiles can be strained quite a lot, before a spatial period-doubling appears. For higher Shields parameters and lower settling velocities the doubling happens earlier as shown in figure 6.8. Here a profile with one big and one small ripple is in fact stable. This was also shown in the one-dimensional experiments of Scherer *et al.* (1999).

6.3 Stability analysis

The dynamics of the ripples and the mechanics behind the selection of wave length has been analysed in more detail using a stability analysis of the fully developed profiles. The idea is to have two identical fully developed ripples in a periodic domain, except that one of the ripples is perturbed. When the morphological model is run with these initial conditions two things can happen; either the ripples are unstable and the smaller ripple will be taken over by the larger ripple and diminish, or the ripples are stable such that the smaller ripple can grow and the two ripples will end up with equal size. The wave length where there is a cross over between stability and instability is the marginally stable wave length.

An example of such an analysis is shown in figure 6.9. Here the ripple lengths are $\lambda/a = 1.15$ and 1.35. The flow conditions are the ones of test

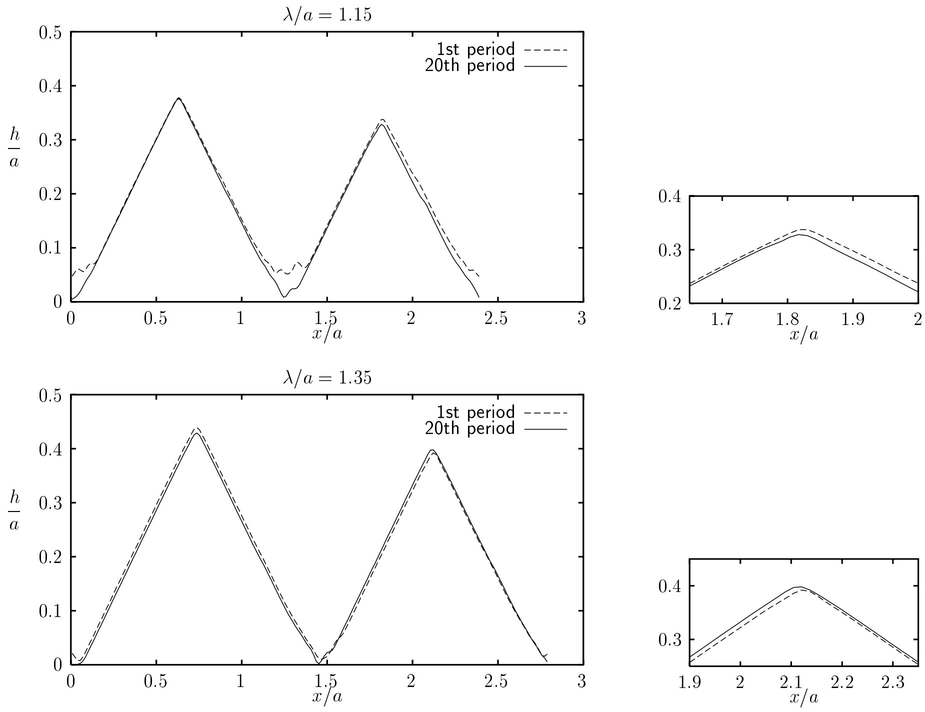

Figure 6.9: The evolution of two non-equal ripples from morphological calculations. The small plots on the right show a zoom of the crest region on the right-most ripple (test case W3).

case W3, i.e., $\theta' = 0.50$ and $w_s/U_m = 0.185$ – a bed load dominated regime. The right ripple is perturbed by making it 10 % smaller than the left ripple. Two different behaviours are observed: in the case where $\lambda/a = 1.15$, the smaller ripple is slowly being eaten by the larger ripple. In the other case the two ripples are stable, and the smaller ripple slowly grows. The marginal wave length is therefore to be found in between the wave length of the short ripples in the examples, so $\lambda_m \simeq 1.25$. In practice the stability analysis is done for many wave lengths to find the wave lengths with cross-over between stability and instability.

6.3.1 The exchange of sediment between ripples

It is interesting to examine the mechanisms underlying the stability properties of the ripples. To this end the exchange of sediment between the two ripples is studied. Again focus on the case of the two ripples where the right ripple is the smaller ripple. If the net transport across the trough between the left and the right ripple is positive, sediment will be transfered from the

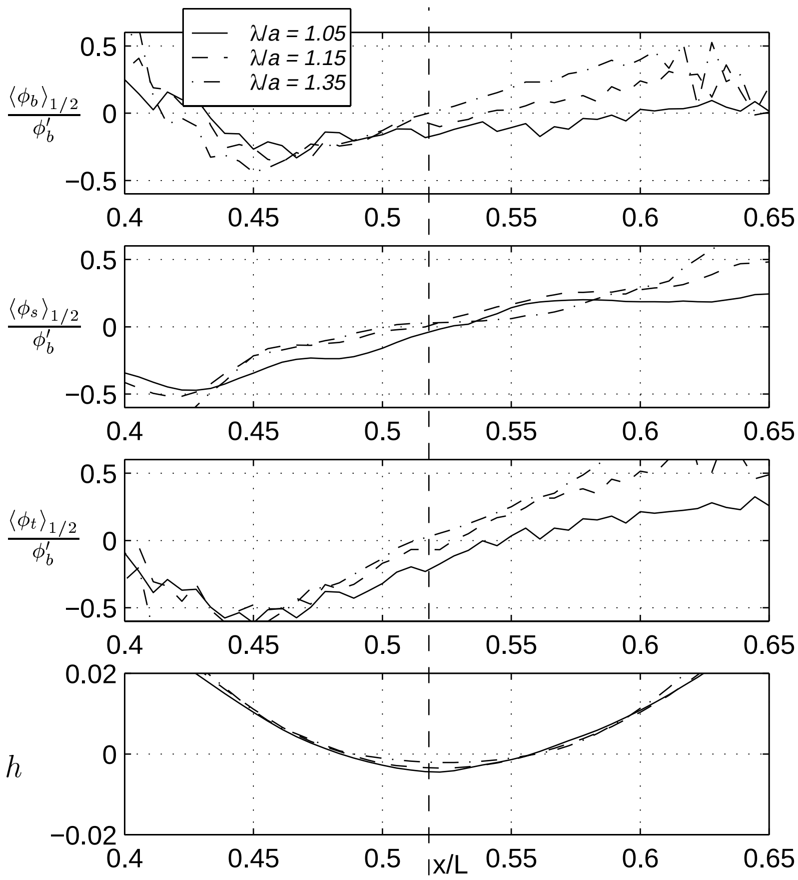

Figure 6.10: The time-averaged sediment transport over the trough region between two ripples for three different ripples lengths. The sediment transport is divided by the maximum bed load on a flat bed, ϕ_b'. ϕ_t is the total sediment transport. The vertical line marks the trough point. The average is performed over period no. 2 to 10. (test case W1).

Table 6.1: The time- and space-averaged sediment transport rates in the trough between two ripples (test case W1).

	$\lambda/a = 1.1$	$\lambda/a = 1.2$	$\lambda/a = 1.4$
$\langle\phi_b\rangle_{x,t}$	-0.0296	-0.0164	0.0093
$\langle\phi_s\rangle_{x,t}$	-0.0065	-0.0017	-0.0088
$\langle\phi_t\rangle_{x,t}$	-0.0362	-0.0147	0.0004

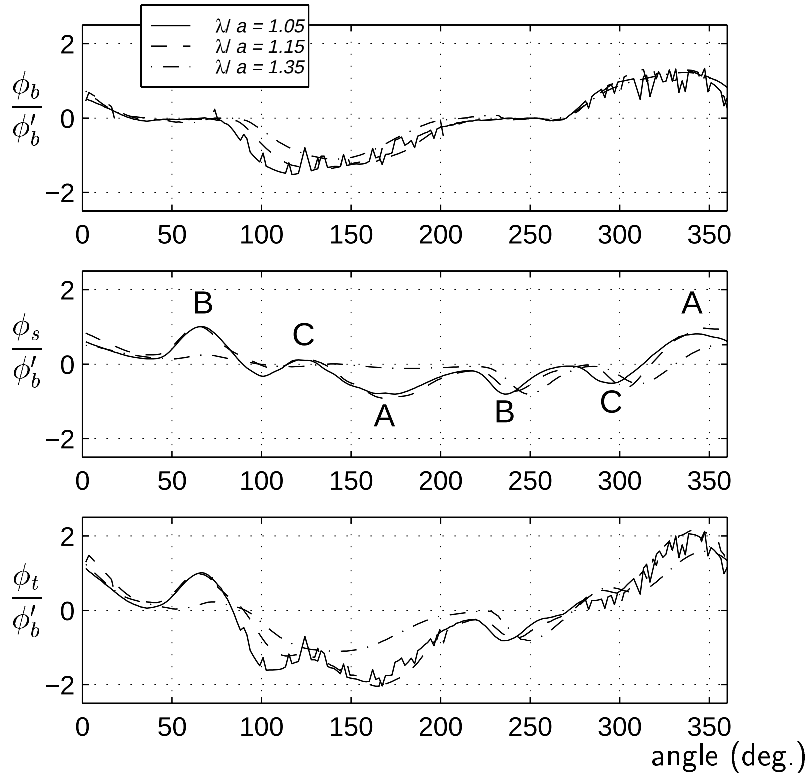

Figure 6.11: The sediment transport over the trough region between two ripples as a function of time. The wiggles in the bed load are due to avalanches in the trough region (test case W1).

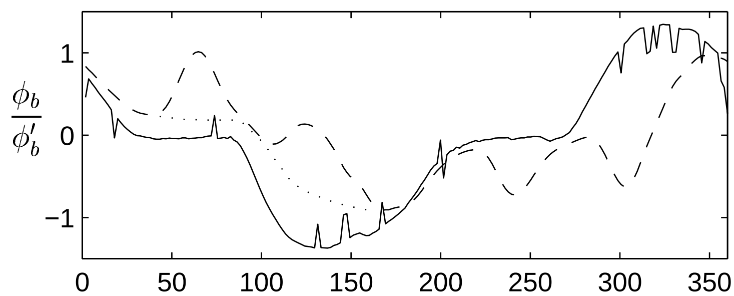

Figure 6.12: The sediment transport over the trough region between two ripples as a function of time for $\lambda/a = 1.15$. The dotted line is an estimation of the suspended transport without the advected part (test case W1).

left profile to the right, i.e., the profile is stable and vice versa.

For such a configuration the sediment transport from the second to the tenth period has been averaged (figure 6.10). The first period was discarded to avoid effects due to the initial reshaping of the profile used as start condition. The time averaged bed load in the trough (figure 6.10, top) is determined by the strength and the extension of the separation bubbles from the large and the small ripples. For the two smaller profiles ($\lambda/a = 1.05$ and 1.15) the separation bubble from the large ripple dominates, and sediment is transfered from the small to the large ripple. For $\lambda/a = 1.35$ the relative strengths of the two bubbles changes, and a small amount of sand is transported to the smaller ripple from the large ripple.

For this case (W1) the suspension (figure 6.10, second from the top) is dominated by the near-bed suspension, and a somewhat similar transport patterns as for the bed load is seen.

A time series of the sediment transport in the trough between the two ripples has been extracted (figure 6.11). To obtain a reasonably smooth signal the transport in ten points around the trough point were averaged to make the time series. A first observation shows quite a lot of sediment going back and forth over the trough, even in the case where the two ripples are stable. The marginal wave length is therefore not the no-interaction limit as was the case for the rolling grain ripples (section 3.2.2); the equilibrium situation for the vortex ripples is rather dynamical. If the wave length were determined by the no-interaction limit, the wave length could be found from an examination of the length of the separation bubbles in figure 4.8.

The bed load in the trough is mainly created by the separation bubbles moving back and forth over the trough. The small wiggles in the bed load are the fingerprint of small avalanches occurring in the vicinity of the trough. The bed load created by the smaller ripple ($\omega t = 275\,^\circ$ to $15\,^\circ$) is almost identical for the three cases. The same is the case for the separation bubble created by the longer ripple, except for the case with $\lambda/a = 1.4$ where the bed load created by the longer ripple becomes smaller than the one created by the smaller ripple. Thus the longer ripple is not able to regain as much sediment as the smaller ripple gain from the longer ripple.

In the time series of the suspended sediment three maxima can be observed (figure 6.11, middle and figure 6.12). The suspended sediment can be split into two parts: the near bed suspension and the advected suspension (see also section 5.1). The two maxima “B” and “C” are created by the advected suspension, and if they are ignored (the dotted line in figure 6.12) the near bed suspension, which follow the bed load signal, can be estimated. It is then clear that maximum “A” is created by the near bed suspension. The maximum “B” is created when the cloud of sediment in the vortex from

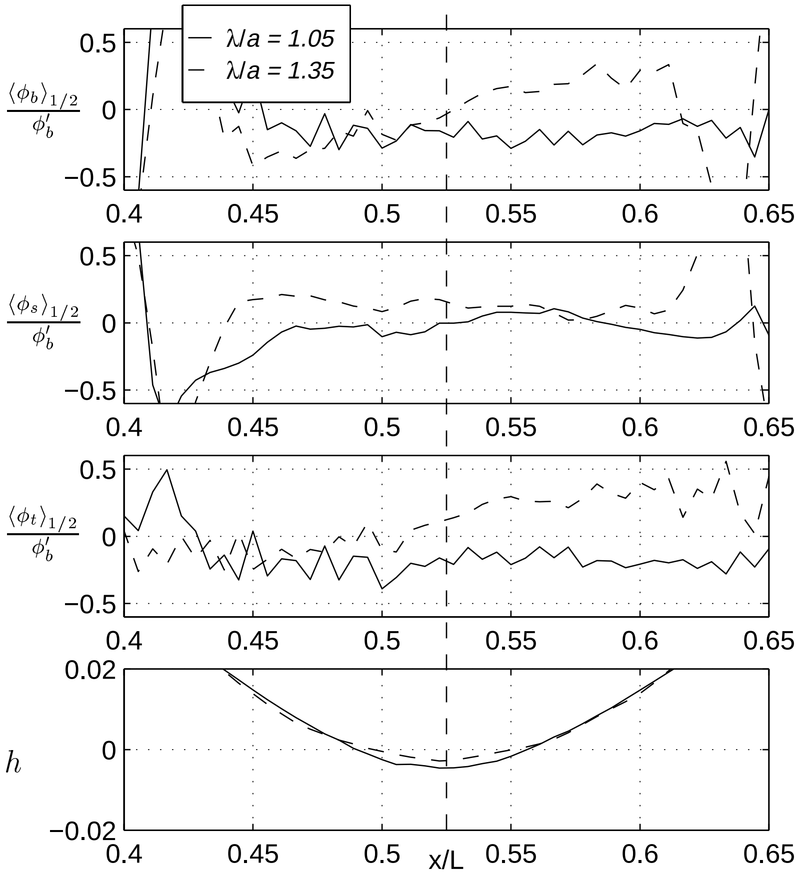

Figure 6.13: As figure 6.10, but with $w_s/U_m = 0.09$.

the second half period is advected over the trough (see also figures 5.5 and 5.6, $\omega t = 60\,°$). The maximum "C" is created when the vortex returns a second time. This time the bubble does not carry any sediment, but as it crosses the crest it triggers an extra discharge of sediment as a jet on top of the separation bubble (the return of the vortex can be seen on figure 4.4, $\omega t = 120\,°$ to $150\,°$). For $\lambda/a = 1.35$ the "B" and "C" maxima disappears because the sediment has been deposited before it reaches the trough. For smaller settling velocities the "B" maximum will still be present. The "C" maximum, however, disappears because the vortex never reaches the trough a second time.

In the above example the bed load was dominating, and the suspension only played a very minor rôle. The same procedure has been repeated, but to add more suspension, the settling velocity has been lowered to $w_s/U_m = 0.09$

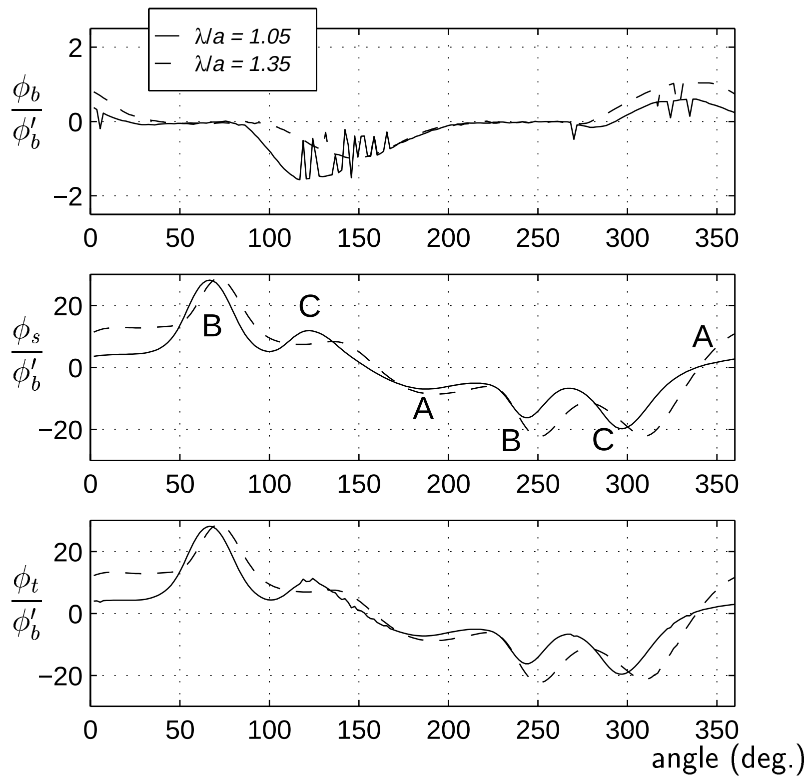

Figure 6.14: As figure 6.11, but with $w_s/U_m = 0.09$.

(figures 6.13 and 6.14). The bed load is similar to the previous case, which is to be expected as the Shields parameter have not been changed. Even though the levels of suspension is in general much higher in this case compared to before (on the order of $30\phi'_b$ compared to $1\phi'_b$ before, see figure 6.14, middle), there is not any major changes in the net transport of sand between the ripples, and the marginal wave length is not affected. For even lower settling velocities down until $w_s/U_m \simeq 0.070$ the selection of wave length is not affected by the large amount of sediment present. It thus seems as if the selection is still governed by the bed load and the near-bed suspension in the trough.

When the settling velocity becomes smaller than $0.070U_m$ the marginal wave length suddenly changes from around $1.25a$ to $0.8a$ (figure 6.15 and 6.16). The average bed load in the trough is seen to be negative for both the long and the short set of ripples. This is of course to be expected as the separation bubble now will be fully developed and cover most of the neighbouring ripple. If the bed load over the trough is almost the same for

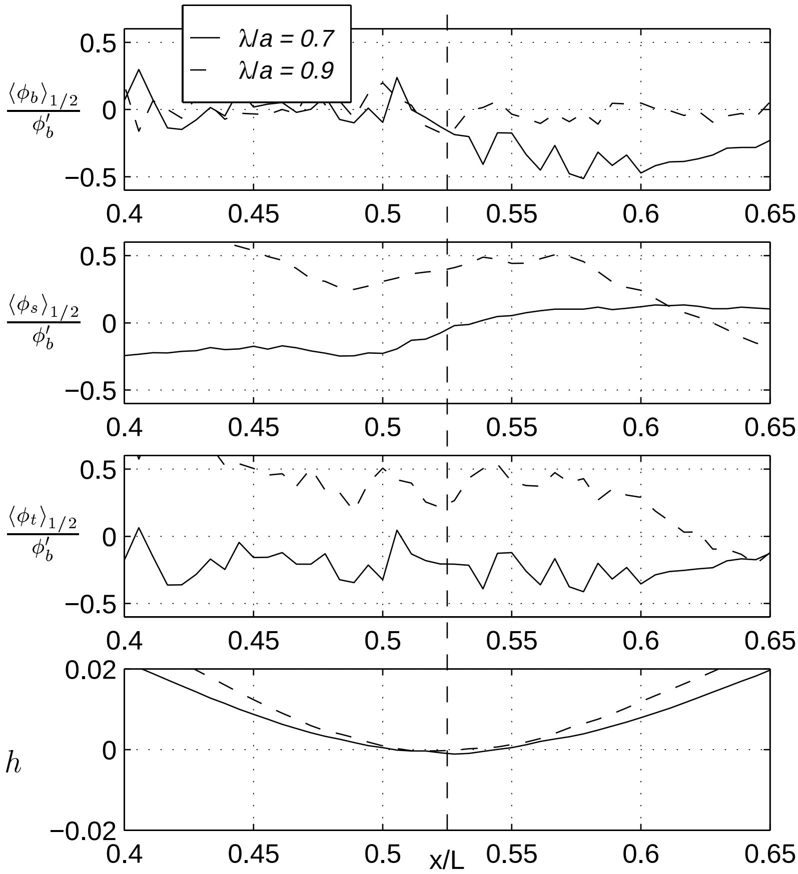

Figure 6.15: As figure 6.10, but with $w_s/U_m = 0.065$.

both ripple lengths, there is a big difference in the suspension, and it is the suspension which governs the selection of the marginal wave length.

6.3.2 Results

The morphological stability analysis have been conducted for Shields parameters 0.15 and 0.50, and settling velocities in the range from 0.03 to 0.185 (figure 6.17). The marginal wave length seems to be completely independent on the Shields parameter. Furthermore the wave length is also independent upon the settling velocity, except at the transition from the near bed dominated regime to the regime dominated by advected suspension.

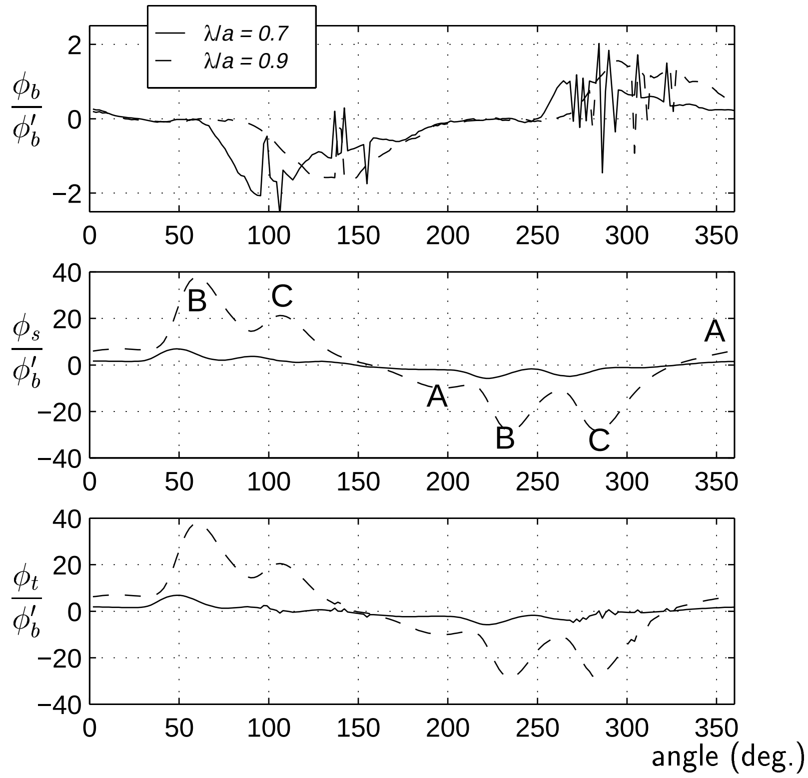

Figure 6.16: As figure 6.11, but with $w_s/U_m = 0.065$.

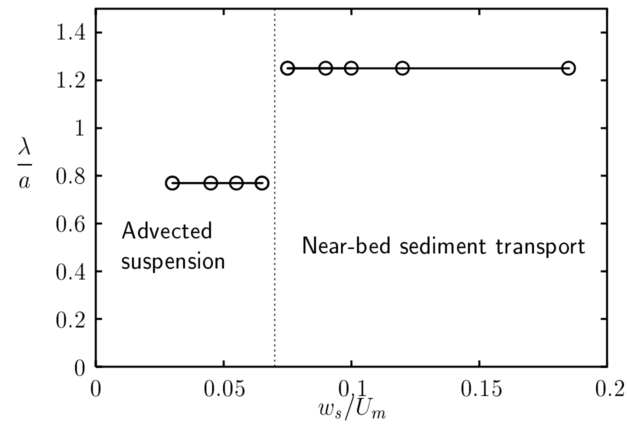

Figure 6.17: The variation of the marginal wave length as a function of the settling velocity.

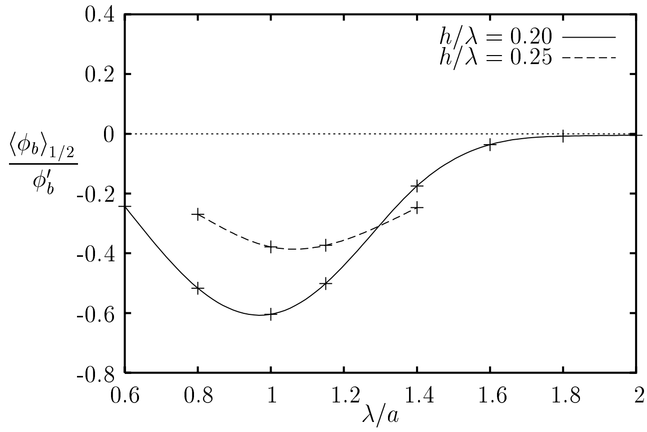

Figure 6.18: The bed load in the trough averaged over one half wave period for two steepnesses as a function of the wave length. The lines interpolating the points are drawn using cubic splines (test case W1).

6.4 The stability analysis using fixed profiles

In the previous section a method was devised to find the marginal wave length using a stability analysis of two almost equal-sized ripples. It was furthermore elucidated that the stability/instability of the smaller of the two ripples could be deducted by looking at the sediment transport over the trough. This method is computationally rather demanding as morphological calculations are involved and many periods of iterations might be needed before a clean trend shows up near the marginal stability point. It would therefore be very convenient if the calculations could be done using fixed profiles thus avoiding the morphological calculations. A method to accomplish this is outlined in the following.

If the two ripples considered are very close to being equally sized, the small difference between them can probably ignored when the transport over the trough is considered. It will therefore be enough to examine the transport in the trough of just one single ripple. This was already done to some extent in section 4.2.2, where the shear stress averaged over one half period in the trough were described as a function of the wave length of the ripple. As the sediment transport is a non-linear function of the shear stress, the average shear stress in the trough will not give the right information. Therefore the average bed load in the trough has been calculated (figure 6.18). It was found that the trough bed load was dependent upon the steepness of the ripple so therefore two different steepnesses were used. The bed load is predominantly negative, reflecting the fact that the separation bubble causes sediment to

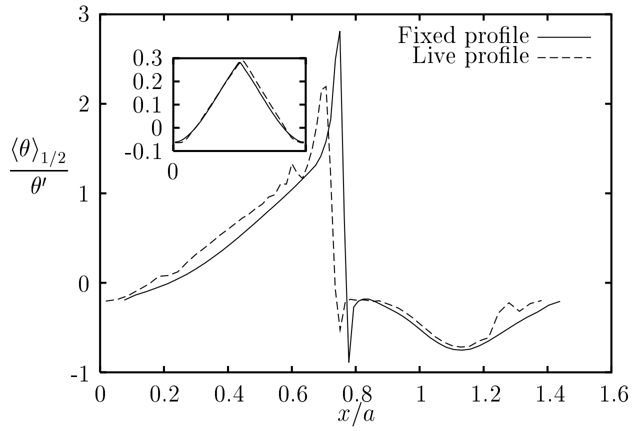

Figure 6.19: A comparison between the Shields parameter on a fixed and a moving profile. Due to the movement of the crest (see inset), the result from the fixed profile have been moved 4 % to the right to obtain a good agreement between the two. The inset shows the fixed profile and the live profile at the end of one the half period with flow from the left to the right.

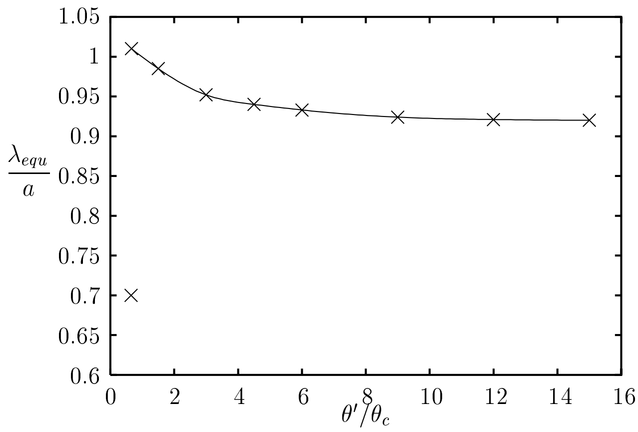

Figure 6.20: The marginal wave length for different values of the Shields parameter using fixed profiles and considering only bed load. This is made for $h/\lambda = 0.20$. The full line is an interpolation using cubic splines.

be moved over the trough from the neighbouring ripple. A clear minimum in the trough bed load is evident around $\lambda/a = 1.0$ for $h/\lambda = 0.20$ and around $\lambda/a = 1.07$ for the steeper ripple. It can easily be argued that the minimum of these curves are exactly at the marginal wave length: imagine two ripples with slightly different wave lengths. The net transport over the trough can

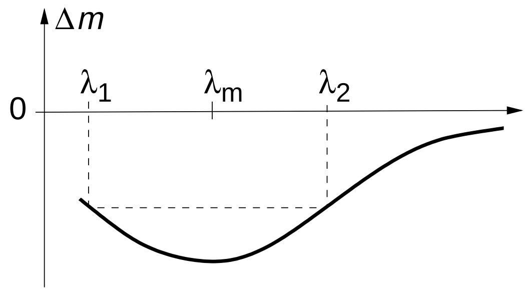

Figure 6.21: Illustration of period-two stable profiles.

now be calculated using the curves shown in figure 6.18. The one ripple with the largest (negative) transport over the trough will gain sediment from the other ripple, and this ripple will then dominate. The most dominant ripple is the ripple with the largest (negative) transport over the trough, which has a wave length corresponding to the position of the minimum in figure 6.18.

The marginal wave length which is calculated this way is somewhat smaller than what is to be expected. The reason for this is that the movement of the crest has not been taken into account. For this example (W1), the crest moves approximately $0.1a$ back and forth. This means that the separation bubble will be pushed a little bit further away from the crest than is the case for the fixed profile. This is illustrated in figure 6.19 where the Shields parameter averaged over one half period is compared for a live ripple and the fixed ripple ($h/\lambda = 0.25$) used in the calculation to construct figure 6.18. As is expected, the graph of the Shields parameter has to be shifted to the right to obtain a good correspondence. This shows that the wave length calculated with fixed profiles should be adjusted with approximately 8 % to account for the moving crest. The wave length calculated before, $\lambda_{equ} = 1.07a$ now becomes $\lambda_{equ} = 1.14a$, a result which is in better correspondence with the stability analysis in the previous section.

This method of calculating the marginal wave length can be tried for different values of the Shields parameter. It was found that changing the Shields parameter does not lead to any change in the marginal wave length, unless the Shields parameter is very small (figure 6.20). Here the non-linearity caused by the critical Shields parameter becomes strong and makes a limitation of the wave length. The smallest Shields parameter shown in the figure is $\theta' = 0.033$. If the Shields parameter is made just slightly below that value, the length quickly dips to around 0.7, and then there is no more motion of sand in the trough. This means that for $\theta' < 0.033$ the profiles are frozen, and no more dynamics between the ripples takes place. There might still be some motion of sand on the crests of the ripples, but the ripples will not

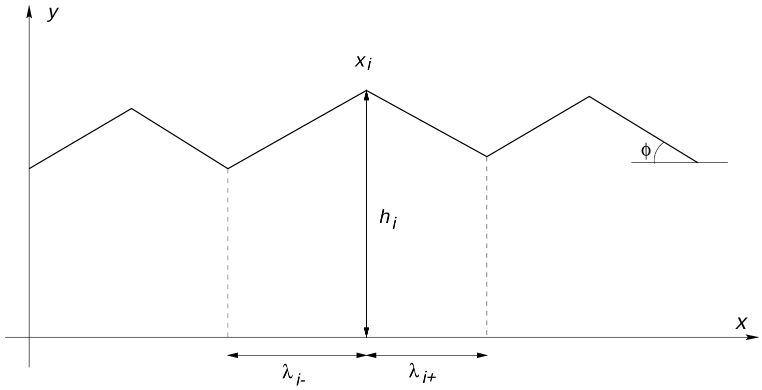

Figure 6.22: The geometry of the ripples in the simple model. Note that the ripples does not have to be symmetric.

be able to affect the neighbours. The description of the transport of sand over the trough also help explaining the period-two profile seen in figure 6.8. Define the transport over the trough averaged over one half period as

$$\Delta m(\lambda) \equiv \langle \phi_b \rangle_{1/2} |_{trough}. \tag{6.2}$$

If the length of the domain is smaller than $2\lambda_m$ there might exist an equilibrium situation where

$$\Delta m(\lambda_1) = \Delta m(\lambda_2) \quad \text{and} \quad \lambda_1 + \lambda_2 < 2\lambda_m \tag{6.3}$$

– this is illustrated in figure 6.21. This is the situation in figure 6.8. This also gives a method of obtaining two points on the curve $\Delta m(\lambda)$.

6.5 A simple model of the dynamics of ripples

In this section a simple model for the dynamics of the ripples, based on the exchange of sediment between neighbouring ripples, is constructed.

Similar to the model of the rolling grain ripples the ripples are here considered as single "particles". Each ripple consist of a left and a right side with lengths λ_{i-} and λ_{i+} respectively. The ripples are triangular with a fixed angle of repose ϕ. Each ripple is characterised by a position x_i and a height h_i (figure 6.22). Using the positions and the heights of the neighbouring ripples, the lengths of each side can be found:

$$\lambda_{i-} = \frac{1}{2}\left[x_i - x_{i-1} + \frac{1}{\tan\phi}(h_i - h_{i-1})\right] \tag{6.4}$$

$$\lambda_{i+} = \frac{1}{2}\left[x_{i+1} - x_i + \frac{1}{\tan\phi}(h_i - h_{i+1})\right] \tag{6.5}$$

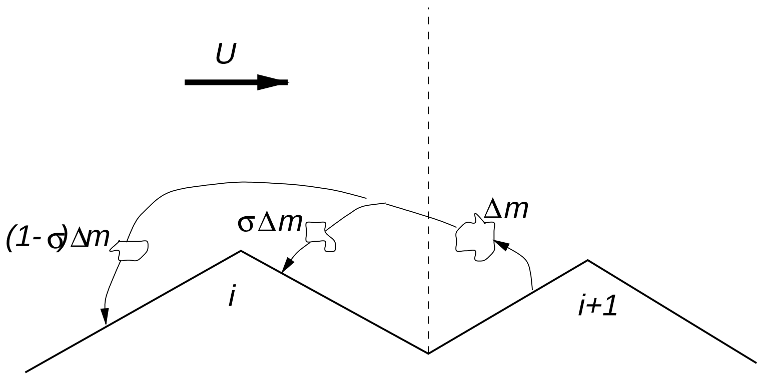

Figure 6.23: The exchange of sediment between a ripple and the neighbour in the first half period. The ripple i exchanges sediment with the ripple $i+1$. Note that the mass Δm does not have to be positive – a negative mass corresponds to the arrows pointing the other way.

and the masses:

$$m_{i-1} = l_{i-}(h_i - \frac{1}{2}\lambda_{i-} \tan\phi) \tag{6.6}$$

$$m_{i+1} = l_{i+}(h_i - \frac{1}{2}\lambda_{i+} \tan\phi). \tag{6.7}$$

The total length of the ripple is $\lambda_i = \lambda_{i-} + \lambda_{i+}$. The dynamics enters when mass is exchanged between neighbouring ripples. Each half period some mass Δm is taken from the neighbouring ripple (the right ripple in the first half period and the left ripple in the second half period). This mass is distributed on the two sides of the ripple; for the first half period:

$$\Delta m_- = (1-\sigma)\Delta m \tag{6.8}$$

$$\Delta m_+ = \sigma \Delta m \tag{6.9}$$

and vice versa for the second half period (figure 6.23). If $\sigma = 1$ all the sediment is deposited on the side next to the neighbour from which the sediment is taken, and if $\sigma = 0$ the sediment is deposited on the other side. In both these cases there is only a weak coupling between the two sides of the ripple, which will result in very asymmetric ripples. To get a stronger coupling σ should have a value between 0 and 1. Here is used $\sigma = 1/2$.

The crucial point is the amount of sediment exchanged each half period Δm. Following the findings in the previous section, this is a function of the length of the ripple $\Delta m(\lambda_\pm)$, where $\lambda_\pm$ is λ_+ for the first half period (with positive flow) and λ_- in the second half period. Δm has been modelled as a

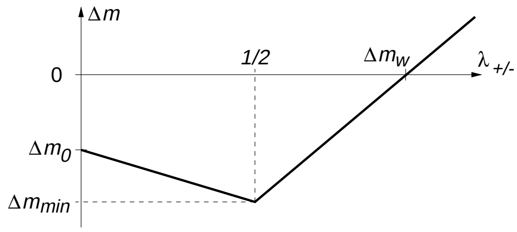

Figure 6.24: The function Δm as a function of the length of one side of the ripple $\lambda_\pm$.

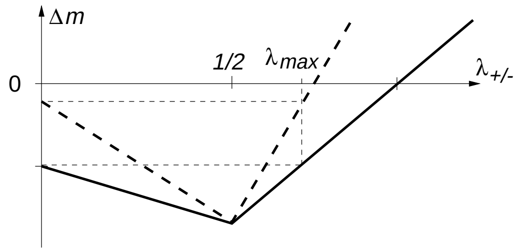

Figure 6.25: An example of two different shapes of the interaction function having the same value of λ_{max}.

bi-linear function, defined by the three parameters Δm_0, Δm_{min} and Δm_w (figure 6.24):

$$\Delta m(\lambda_\pm) = \begin{cases} \Delta m_0 + 2(\Delta m_{min} - \Delta m_0)\lambda_\pm & \text{for } \lambda_\pm < \frac{1}{2} \\ \Delta m_{min}\left(1 - \dfrac{\lambda_\pm - \frac{1}{2}}{\Delta m_w - \frac{1}{2}}\right) & \text{for } \lambda_\pm \geq \frac{1}{2} \end{cases} \tag{6.10}$$

The minimum point of Δm is now at one half, which means that all lengths are made non-dimensional with the (total) ripple length at the minimum.

The parameters entering the model are the initial length of the ripples λ_0, the length of the domain L and the three parameters characterising the interaction function Δm. These three parameters can be reduced to only one important parameter.

Firstly, Δm_{min} is seen to be of minor importance. It has to be remembered that the interaction function describes the transfer of mass over one half period, while the important quantity is actually the transfer of mass averaged over one whole period:

$$\langle \Delta m_i \rangle_t = \Delta m_i(\lambda_{i,+}) - \Delta m_i(\lambda_{i+1,-}), \tag{6.11}$$

which is independent upon Δm_{min}.

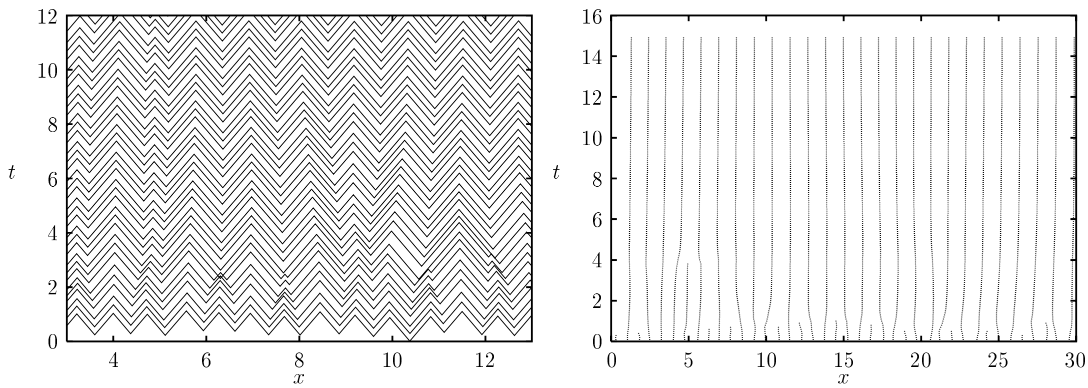

Figure 6.26: An example of the dynamics of the model. Left: a zoom of the ripple profiles, right: the evolution of the ripple crests. The time scale is arbitrary ($\lambda_{max} = 1.35$).

Secondly, the two parameters Δm_w and Δm_0 can be combined into just one other parameter, λ_{max}, which sets an upper limit for the ripple length (figure 6.25):

$$\lambda_{max} = \Delta m_w - \frac{\Delta m_0(\Delta m_w - \frac{1}{2})}{\Delta m_{min}}. \tag{6.12}$$

If the side of a ripple becomes longer than λ_{max} then there is room for another ripple which can dominate the large ripple. If the interaction is just described in terms of λ_{max} the steepness of the function is still left undescribed. This determines the magnitude of $\langle \Delta m \rangle_t$, which again sets the speed of the interaction which can be scaled out.

6.5.1 Results

Following the curve in figure 6.18, a reasonable choice of parameters for the interaction function is: $\Delta m_0 = -0.3$ and $\Delta m_w = 0.75$; Δm_{min} is arbitrarily set to -1. This gives $\lambda_{max} = 1.35$. These absoulte numbers for the mass is of course far too big, and a relaxation factor on the order of 1/20 is used. Results from a sample run with 100 initial ripples and the initial ripple length $\lambda_0 = 0.75$ are seen in figure 6.26. A fast coarsening process is seen in the beginning, followed by a slower relaxation towards the equilibrium state. A careful analysis showed that, given a large enough domain, the equilibrium wave length is *not* dependent upon the initial conditions. For this example $\lambda_{equ} = 1.15 \pm 0.02$. This value is in between the minimum wave length, 1, and the maximum wave length 1.35. It is, however, not just the average of the two.

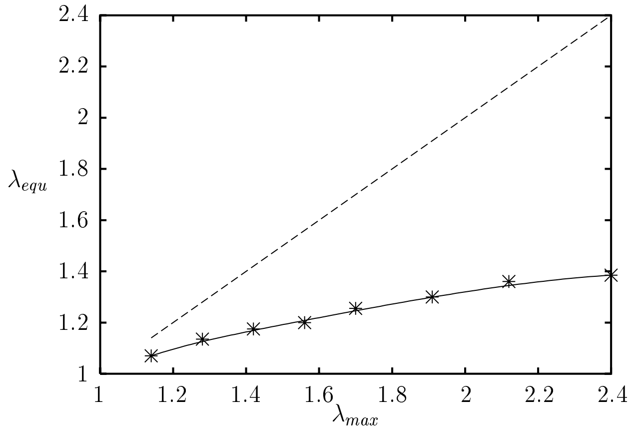

Figure 6.27: The equilibrium wave length for different values of λ_{max}. The dotted line is $\lambda_{equ} = \lambda_{max}$.

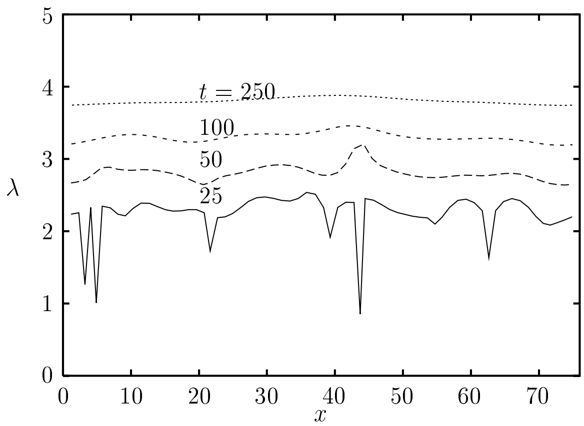

Figure 6.28: The evolution of the wave lengths in the model (same parameters as used in figure 6.26). Each line is shifted to allow them to be distinguished from each other.

The equilibrium wave length has been calculated for different values of λ_{max} (figure 6.27). Here it is even more clear seen that the equilibrium wave length saturates to a value smaller than the average of the minimum and the maximum wave length.

The possibilities of this model are far from exhausted. One particularly exciting aspect is the possibility of making a connection with so-called phase equations (Cross and Hohenberg, 1993). Such an equation should be able to describe the slow relaxation of the model, i.e, the final adjustment of the pattern. The evolution of the local wave lengths in the model are shown in figure 6.28. Apart from the curve for $t = 25$ where there are smaller ripples in between the more mature ripples, a smooth modulation of the wave length is observed, which should be captured by a continuous model.

Another obvious extension is to use the model for the case of two dimensional ripple profiles.

6.6 The equilibrium profile of ripples

The equilibrium profile of vortex ripples has been the topic of some speculation. One reason for the interest is that the steepness is important for the friction and the roughness (see the article "Wave plus current over a ripple-covered bed").

Sleath (1982) proposed a conformal mapping for the ripple profile, based on measurements of ripple profiles (figure 6.29). This profile have a rounded crest, and Sleath argued that this was an average equilibrium profile. The average was performed over the wave period, where the crest is rocking back and forth. The shape of the crest is quite important for the flow over the ripples, and a rounded crest seems to be particularly unsuited for the simulations of the flow over ripples, as this gives a less strong separation bubble than would have been the case with a ripple with sharp crest.

Fredsøe (1992) and Brøker (1985) have developed a simple model which gives either very triangular profiles or a parabolic profile (figure 6.29).

The basic concept behind the simple models of the ripple profile developed by Fredsøe and Brøker, is to calculate the profile that has a zero transport averaged over one period, i.e.,

$$\left\langle q_b(x,t,h_x) + \int_{h(x)}^{D} q_s(x,t)\,dy \right\rangle_t = 0 \tag{6.13}$$

for all x, where h_x is the bed slope. The bed load is a function of the slope of the bed through the gravity correction[1]. If the shear stress on the bed and the suspension are known, equ. (6.13) can be solved for $h_x(x)$, which can be integrated to find $h(x)$. In the models of Fredsøe and Brøker the idea is to make a plausible assumption of the shear stress and the suspension, and from that calculate the profile. In the bed-load-only-case, it was found by Brøker that almost any reasonable assumption gives a very triangular profile. By adding suspension she found corrections to the profiles, making the ripples less steep (figure 6.30).

[1]In fact the suspension is also a function of the bed slope through the bed boundary condition, but this has been ignored for the present purposes.

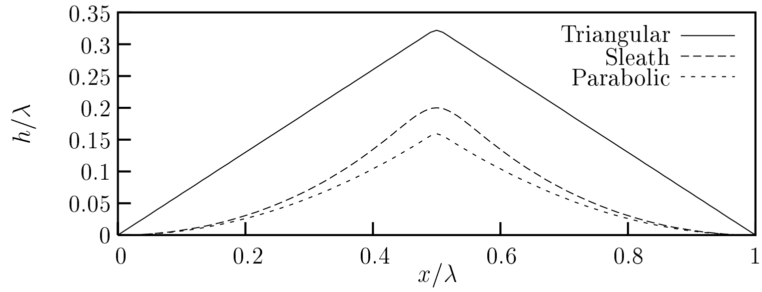

Figure 6.29: Three examples of ripple profiles: a triangular profile with sides the angle of repose (33 °), a parabolic profile with steepness $h/l = 0.1625$ as suggested by Fredsøe (1992) and the profile made by the conformal mapping of Sleath (1982). The steepness of the latter profile has been set to 0.2.

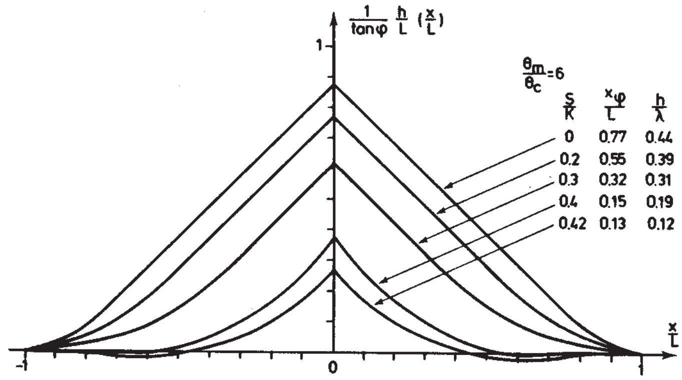

Figure 6.30: Example of the profiles found by Brøker. The less steep the profiles the more suspension (from Brøker (1985))

Using a fixed profile, the shear stress and the suspension have been calculated for $\theta' = 0.15$ and $w_s/U_m = 0.10$ (figure 6.31, left). Solving equ. (6.13) for h_x and imposing a maximum slope of the angle of repose, the profiles shown in figure 6.31, right is found. The profiles are almost triangular except for a small rounded trough. This shows that a major the part of the ripple is dominated by avalanches. As this method does not resolve the back and forth motion of the crest, the resultant steepness is too large, but apart from that there is not much difference between the simple calculation and

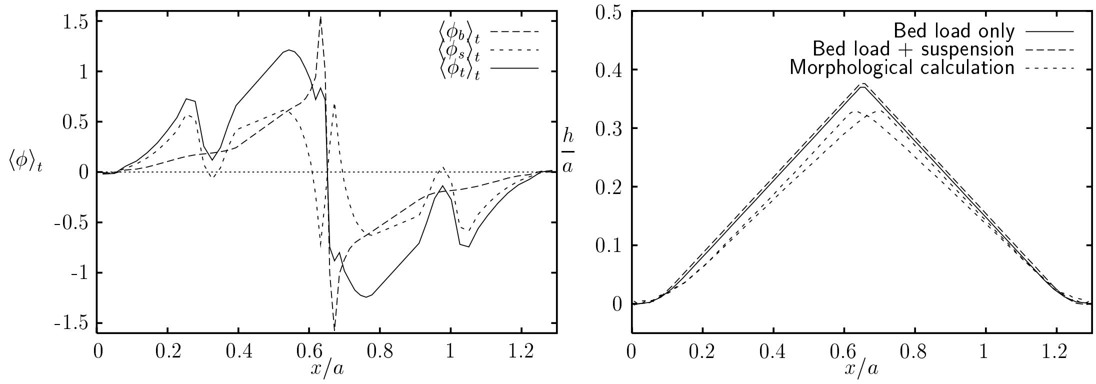

Figure 6.31: The sediment transport over a fixed profile averaged over one period (left) and the resultant profiles compared with the profiles from a morphological calculation, shown in the two extreme positions ($\theta' = 0.15,\ w_s/U_m = 0.10$).

the full numerical solution.

6.6.1 Results

Using the morphological calculations the ripple profiles have been calculated for $\theta' = 0.15$ and $\theta' = 0.50$ for a wide range of settling velocities (figure 6.32 and 6.33). In all cases in the regime dominated by bed load and near-bed transport, the ripples are very triangular, but they become slightly less steep as the settling velocity is lowered. This might be partly due to a larger back and forth motion of the crest as the sediment transport is increased, which gives rise to less steep ripples.

The ripples are in general steeper than could be expected from the measurements presented in section 6.1. The discrepancy might partly be due to the use of too large an angle of repose (33 °). As there is permanent motion on the sides of the ripples, the packing will be loose, and they can not be expected to reach the static angle of repose. In fact, Stegner & Wesfried (1998) found that the angle of repose on the ripples were 27 % to 15 % lower than the static angle of repose. This means that the steepnesses calculated here are overestimated by approximately 20 % to 30 %.

6.7 Waves plus current

The stability analysis for finding λ_m can in principle be repeated for the case of waves plus current. If the calculations needed were big for the wave-only

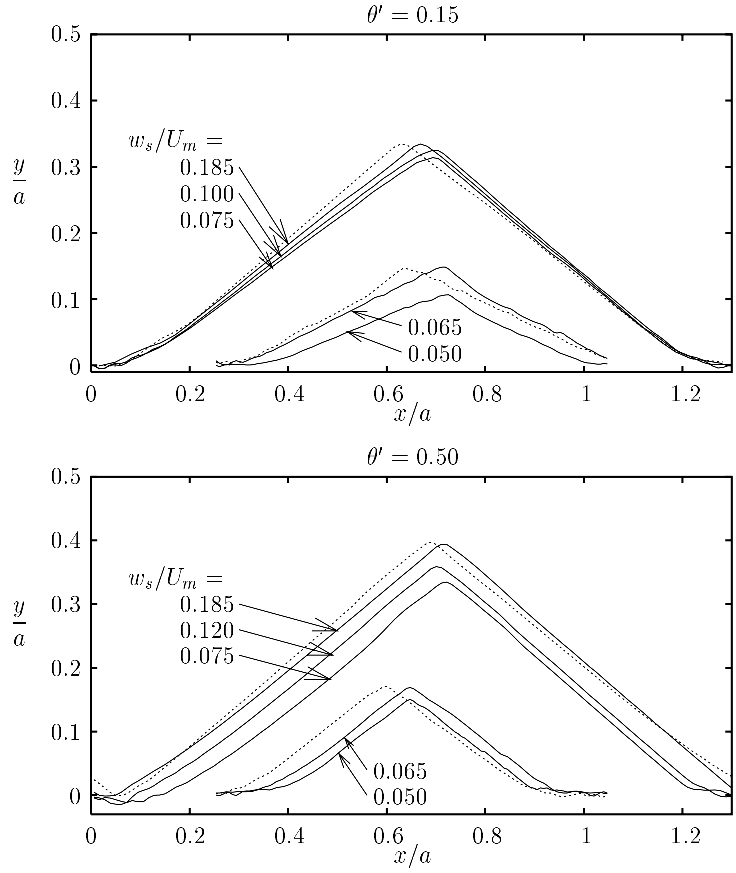

Figure 6.32: The equilibrium profiles for ripples with $\theta' = 0.15$ (top) and $\theta' = 0.50$ (bottom) and varying the settling velocity from $w_s/U_m = 0.185$ to 0.050. The profiles are shown at the end of the first half period, but two profiles (stippled lines) are shown at the end of the second half period to illustrate the movement of the profile during the period.

case, they are enormous for the wave plus current case. Furthermore the phase space in the case has been enlarged due to the appearance of the two quantities U_c/U_m and D/a.

As an example of morphological calculations under wave plus current conditions, the equilibrium profile has been calculated for $D/a = 5$ and a current strength varying between zero and U_m (figure 6.34 and table 6.2). For $U_c/U_m \leq 0.5$ the wave-only profile is only subject to minor changes due to the current, but for $U_c = U_m$ the profile is very asymmetric and clearly dominated by the current.

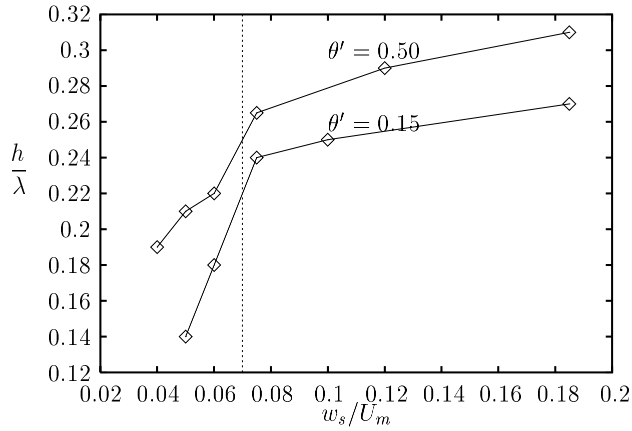

Figure 6.33: The steepness of the ripples as a function of the settling velocity.

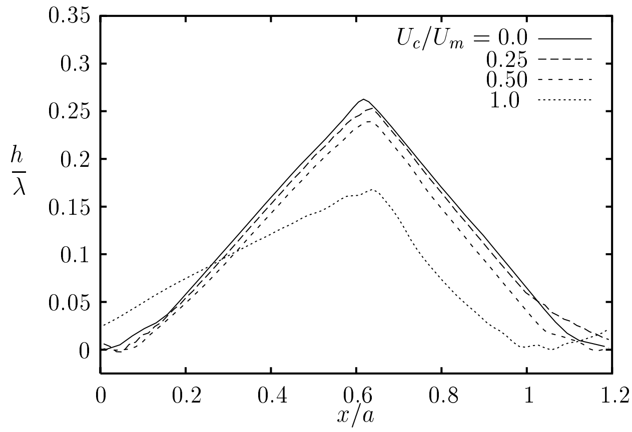

Figure 6.34: Ripple profiles in wave plus current situations ($\theta' = 0.15,\ w_s/U_m = 0.185$).

Table 6.2: The velocity c of the four ripples shown in figure 6.34

U_c/U_m	c/U_m
0	0
0.25	0.00058
0.50	0.00033
1.0	0.00083

6.8 Summing up

The important result in this chapter is that the minimal wave length can be calculated through a stability analysis of the fully developed profiles. It was illustrated in section 6.4 how this method could even be carried out using fixed profiles. The discrepancy between the results from the morphological calculations and the ones using fixed profiles still has to be accounted for. A very interesting question is how λ_m relates to the equilibrium wave length of the ripple. It was argued in section 6.2 that for a full understanding of this, a two-dimensional ripple profile will have to be considered, as the presence of defects are important. A generalisation of the simple model from section 6.5 to two dimensions might help to shed light on this. In relation to the simple model, it should be mentioned that it is very easy to write and interface equation which show ripple-like behaviour (e.g. Csahók, Misbah, and Valance (1998, Terzidis, Claudin, and Bouchaud (1998)). The model presented here is *not* barely based on symmetries and heuristic reasoning, but has a solid foundation based on physical facts.

A interesting question is posed by the sudden jump in λ_m at $w_s/U_m \approx 0.070$. This point marks a transition between ripples formed by near-bed sediment transport and ripples formed by advected suspension. This transition might have a deeper influence on the ripple dynamics. Nielsen (1979) classified a set of measurements into one- and two-dimensional ripples[2] and found, that the transition between one- and two-dimensional ripples was around around $w_s/U_m = 0.070$. This might also show that the ripple profile becomes chaotic and only obtains a steady state in a statistical sense.

The calculated ripple profiles are not surprisingly dominated by the sides being at the angle of repose. The most important parameter governing the steepness is thus the *dynamical* angle of repose.

[2]In fact Nielsen share the common misconception that because a one-dimensional ripple profile is created by a two-dimensional flow, the ripples are also two-dimensional. He thus classified the ripples into two- and three-dimensional ripple patterns.

Chapter 7

Discussion

The backbone of this study of ripples has been to develop a computational model, such that the flow and sediment transport could be studied in detail. The model was capable of performing morphological calculation of ripples. With the aid of the morphological calculations, the dynamics of ripples was studied.

7.1 A qualitative bifurcation diagram

Using the knowledge obtained about rolling grain ripples in chapter 3 and about vortex ripples in chapter 6 it is possible to sketch a bifurcation diagram for the creation of ripples (figure 7.1). As control parameter have been chosen the Shields parameter. Because of the subcritical nature of the bifurcation, there is an unstable branch going backwards from the first appearance of ripples at $\theta' = \theta_c$. This curve shows how large a perturbation is needed to initiate ripples if the Shields parameter is smaller than the critial Shields parameter. As soon as ripples are initiated they will continue to grow until they reach the state of equilibrium vortex ripple shown by the upper curve. This curve is almost horizontal, but the heigth do become slightly smaller as the Shields parameter is increased. The point marked θ_n is the point where there is no exchange of sediment between neighbouring ripples (see section 6.4). The ripples are still stable, and will be stable all the way down to as point where there is no motion even on the crests of the ripples. This point is probably very close to $\theta' = 0$.

Using the bifurcation diagram the question of whether an amplitude equation for the ripples can be derived using an expansion around the first bifurcation from the flat bed ($\theta' = \theta_c$) can be discussed. Strictly speaking the subcritical nature of the ripples does not exclude a description using am-

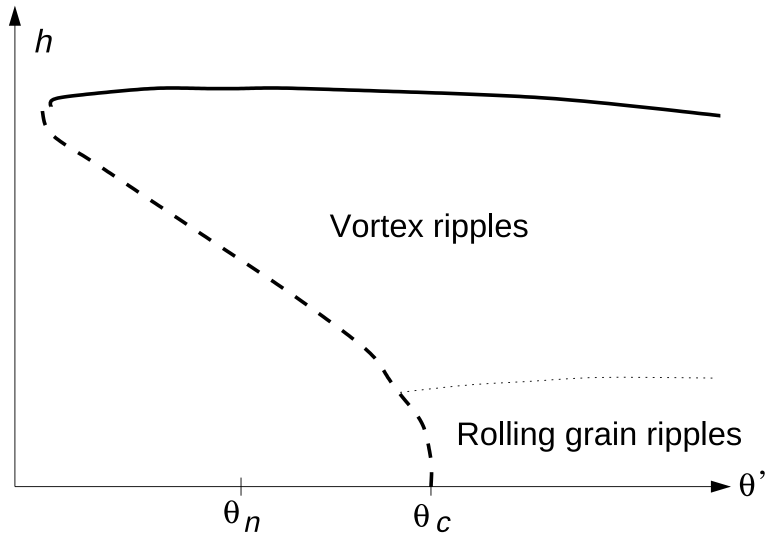

Figure 7.1: A qualitative bifurcation diagram, showing the first bifurcation from a flat bed. The region where rolling grain ripples are expected to occur is loosely sketched.

plitude equations. If the nonlinearities are sufficiently weak an expansion around the first bifurcation will be valid even though the patterns are fully developed and reach the upper line. The vortex ripples are, however, not merely weakly nonlinear. A more important objection is that the ripples created from a flat bed, the rolling grain ripples, a qualitatively different from the fully developed vortex ripples. A description of the dynamics of the rolling grain ripples can therefore not be expected to give any insight on the dynamics of the vortex ripples.

7.2 Summary of main findings

The main points found during the work will be briefly summarised:

- Rolling grain ripples can be described by a granular model. As the physics of rolling grain ripples and vortex ripples are different from each other, a description of the dynamics of the ripples based on an expansion around the flat bed state, i.e., an amplitude equation, is bound to fail.

- The flow and the sediment transport over fixed vortex ripples are similar to the transport over "live" ripples. This was illustrated by developing a method to obtain the minimal wave length using only fixed profiles.

- The relative friction (and thus the roughness) of a wave plus current flow over vortex ripples is mainly a function of U_c/U_m. The same is not the case for the dissipation.

- The sediment transport over ripples are dominated by near-bed sediment transport for $w_s/U_m \gtrsim 0.070$, and by advected suspension for $w_s/U_m \lesssim 0.070$.

- The time- and space-averaged bed load in wave plus current situations is negative, while the suspension is positive.

- The vortex ripples are an example of an extremely non-linear pattern forming system. It was conjectured that the dynamics of the vortex ripples could be described by considering only local interactions between neighbouring ripples.

The use of morphological calculation has proven to be an extremely powerfull tool in the study of ripples. It should, however, be used intelligently – a brute-force calculation with many ripples is not only computationally heavy, but it does not reveal much about the intrinsic mechanisms driving the ripples. The methods developed here for the study of vortex ripples, e.g., the stability analysis of the fully developed profiles, could probably be used with success on other structures formed by fluid flow (bars in rivers, mega ripples in the coastal zone etc.).

Chapter 8

Topics In Shell Models of Turbulence

In this part of the Thesis, some applications of shell models of turbulence are developed. Shell models have become a popular tool in statistical turbulence, and the amount of literature on shell models is large – there seems to be a whole industry producing papers on shell models. The reasons for the popularity of the shell models are twofold 1) it is relatively simple to integrate them numerically and extract high order moments and 2) they describe many of the statistical features of the Navier-Stokes equations, like intermittency, surprisingly well. One major drawback is that they are not derived from the Navier-Stokes equations, but are based on a heuristic reasoning and on conservation of the symmetries in the Navier-Stokes equations.

Two quite different applications of shell models are considered. One is the continuous limit of the so-called GOY model (the attached articles "Bursts and Shocks in a Continuum Shell Model" and "The Zero-spacing Limit of the GOY model"), and the other is the advection of a passive scalar by a minimal shell model (the attached article "Shell Model for Time-correlated Random Advection of Passive Scalars"). As the major part of the work is reported in the articles, only a brief presentation of shell models will be given here.

Many different shell models have been created (see e.g. Bohr *et al.* (1998)). To give a short introduction to shell models, the common GOY model by Gledzer, Ohkitani and Yamada (Gledzer, 1973; Yamada and Ohkitani, 1987) is described. This is the model in which the continuous limit is examined in section 8.2. A short introduction to the work on the advection of passive scalars is given in section 8.3.

8.1 The GOY model

A shell model consist of a discrete number of shells N. To each shell is associated a wave number k_n and a velocity u_n. The shell are spaced such that

$$k_n = r^n \quad \text{with} \quad 1 \leq n \leq N. \tag{8.1}$$

with the standard (arbitrary) choice $r = 2$ the whole inertial range can be covered with relatively few shells, typically between 20 and 30. The velocity of each shell u_n is a (complex) measure of the energy on the shell, and can also be regarded as the velocity difference $\delta v_n = |v(\ell) - v(x + \ell)|$ on an eddy of scale $\ell \sim k_n^{-1}$. The models are thus one-dimensional and therefore lot of the spatial structures observed in real turbulence are not captured in the models.

The crucial point is the interaction between the shells, which are determined using an analogy to the Richardson picture of the turbulent energy cascade. Energy is pumped in at the large scales (shell numbers one and two), forming large eddies. These eddies break up into smaller eddies, which again break upon into even smaller eddies, represented by energy on higher and higher shell numbers, until the eddies are so small that they are dissipated by viscosity. The main idea is that the interaction between the shells is local in k-space, that is, there is only interaction between neighbours and next-nearest neighbours.

The terms in the evolution equation for each shell is determined by analogy to the Navier-Stokes equations. The viscosity is the Fourier transform of the viscous term in the Navier-Stokes equations: $\nu k_n^2 u_n$, and are thus exact.

To preserve the right dimension, the advective terms, which couples the shells, are of the form $k_n u_a u_b$. In the GOY model this is written as:

$$\begin{aligned}(\frac{\partial}{\partial t} + \nu k_n^2)u_n = \\ i(a_n k_n u^*_{n+1} u^*_{n+2} + b_n k_{n-1} u^*_{n-1} u^*_{n+1} + c_n k_{n-2} u^*_{n-1} u^*_{n-2}) + f \delta_{n,n_f}\end{aligned} \tag{8.2}$$

where ν is the viscosity, f the forcing and n_f is the forcing scale. An asterix denotes complex conjugation. The model as it is written has three free parameters, a_n, b_n and c_n. One of the parameters can be gotten rid of by a rescaling of time, and the custom is to set $a_n = 1$. The two other parameters are set depending upon the conserved quantities of the Navier-Stokes equations. The conserved quantities can be written as:

$$Q_\alpha = \sum_{n=1}^{N} k^\alpha |u_n|^2 = \sum_{n=1}^{N} r^{n\alpha} |u_n|^2. \tag{8.3}$$

For the conservation of energy (in the absence of forcing and dissipation) $\alpha = 0$. This enforces the requirement that the coefficients follow the relation:

$$a_n + b_{i+1} + c_{i+2} = 0 \tag{8.4}$$

such that the parameters can be described in term of one free parameter, δ:

$$a_n = 1, \quad b_n = -\delta, \quad \text{and} \quad c_n = -(1 - \delta). \tag{8.5}$$

The behaviour of the model is dependent upon the value of δ, which determines the other conserved quantity. This can be either the enstrophy

$$\Omega = \sum_{i=1}^{N} k_n^2 |u_n|^2 \tag{8.6}$$

which defines a two dimensional variant of the GOY model ($\delta = 1 + r^{-2}$) (see e.g. Ditlevsen & Mogensen, (1996)). For three dimensional turbulence the other conserved quantity is the helicity $H = \sum \mathbf{k} \times \mathbf{v}(\mathbf{k}) \cdot \mathbf{v}(\mathbf{k})$ which in the GOY model becomes:

$$H = \sum_{i=1}^{N} (-1)^i k_n |u_n|^2 \tag{8.7}$$

and $\delta = 1 - r^{-1}$.

8.1.1 Properties of the GOY model

The observable which is commonly used is the pth. order structure function, which in a shell model is defined as:

$$S(p) \equiv \langle u_n^p \rangle \,. \tag{8.8}$$

The structure functions scale with k_n such that $S(p) \propto k_n^{\zeta(p)}$. From the Kolmogorov theory of turbulence the scaling of the structure functions are given as $\zeta(p) = \frac{1}{3}p$. This result is exact for the third order structure function, but for higher order structure functions a deviation from the Kolmorov scaling, is observed; the so-called anomalous scaling. One of the surprising facts is that the GOY model quite accurately have the same anomalous scaling of the structure functions as is seen in measurements of high Reynolds-number turbulence (Jensen *et al.*, 1991).

8.2 Continuous limit of the GOY model

The continuous limits of the GOY model have been studied in the attached articles “Bursts and Shocks in a Continuum Shell Model” and “Continuous Limit of the GOY Model”.

8.2.1 ϵ-expansion

The limit have been explored in two ways. First an epsilon expansion around $\lambda = 1$ was explored. To first order this gives the Parasi-equation (Parisi, 1990):

$$u_t^* + 3ikuu_k = -iku^2, \tag{8.9}$$

where subscript denotes differentiation and the expansion parameter has been eliminated by a rescale of time. This equation was studied in great detail in the first of the two articles. It was found that through a transformation of k and u such that $u = k^{-1/3}v$ and $k = (2x)^{-3/2}$ equ. (8.9) can be turned into a complex Burgers equation:

$$v_t^* - ivv_x = 0 \tag{8.10}$$

It was furthermore found that the real and the imaginary parts has a constant phase. For a pulse moving down the inertial range, the real part became zero, and only the imaginary part survived. Using that equ. (8.10) becomes:

$$v_t - vv_x = 0; \tag{8.11}$$

the Burgers equation, which can be integrated using characteristics. This equation forms shocks, and to integrate through the shock a conservation law has to be applied. In the transformed space the conservation of energy reads:

$$E = \int (2x)^{5/2} v^2 dx. \tag{8.12}$$

If the GOY model is expanded to third order one gets:

$$\begin{aligned} -iu_t^* &= 2\epsilon(1-2\epsilon)u(u+3ku_k)+ \\ &\left[u_k^2k^2(13+6k) + 7u^2 + u(3k^3u_{kkk} + \frac{31}{2}k^2u_{kk} + 34ku_k)\right]\epsilon^3 \end{aligned} \tag{8.13}$$

This equation does not form shocks as it has higher order terms. It does, however, form shocks in the second derivative. This makes it quite difficult to integrate it numerically.

8.2.2 The zero-spacing limit

The limit explored in the article "The zero-spacing limit of the GOY model" is slightly different. Here the shell spacing r is just set to one, such that the middle term in the GOY model (8.2) disappears:

$$\frac{\partial u_n^*}{\partial t} = -i(u_{n+1}u_{n+2} - u_{n-1}w_{n-2}). \tag{8.14}$$

This limit is rather weird, as this means that all the shells have the same k. However, as argued in the article, the qualitative behaviour resembles that of the GOY model for r larger than one, which justifies an examination of that limit. This examination form the basis of the article.

8.3 Advection of a passive scalar

In the statistical mechanics of a turbulent flow two main problems are studied: 1) the statistics of the velocity field and 2) the statistics of a scalar which is being passively advected by the velocity field. It turns out that the intermittency of a passive scalar is much stronger than the velocity field itself, giving rise to stronger anormal scaling (e.g. Jensen *et al.* (1992)).

In 1968 the Kraichnan model of the advection of a passive scalar were introduced which is basically the equation of motion for a passive scalar θ:

$$\frac{\partial \theta}{\partial t} + (\mathbf{u}\cdot\nabla)\theta = \kappa\nabla^2\theta + f_\theta \tag{8.15}$$

where κ is the diffusivity of the scalar, f_θ is forcing and $\mathbf{u}$ is the velocity field. The idea of the Kraichnan model is to advect the passive scalar by a solenoidal random velocity field with a prescribed spatial correlation and delta-correlated in time.

Benzi, Biferale & Wirth (1997) introduced a shell model of the Kraichnan model:

$$[\frac{d}{dt} + \kappa k_m^2]\theta_m(t) = i[c_m\theta_{m+1}^*(t)u_m^*(t) + b_m\theta_{m-1}^*(t)u_{m-1}^*(t)] + \delta_{1m}f(t) \tag{8.16}$$

where $b_m = -k_m$ and $c_m = k_{m+1}$ for imposing conservation of the scalar "energy" defined as $E = \sum_{n=1}^{N}\theta_n\theta_n^*$ in the limit of zero diffusivity and no forcing. The forcing term acting on the first shell is Gaussian and delta correlated in time. The advecting velocity field $u_m(t)$ is composed of independent complex Gaussian processes which are delta correlated in time:

$$\langle u_m(t)u_n^*(t')\rangle = k_m^{-\xi_{wn}/2}\delta(t-t')\delta_{nm} \tag{8.17}$$

where the exponent ξ_{wn} is the parameter determining the scaling of the velocity field. This can be seen as a turbulence parameter with a value between zero and two. This model is much easier to integrate numerically than the Kraichnan model and it has the further advantage that an analytical closure is provided for calculating the anomalous correction to the fourth order structure function (Benzi *et al.*, 1997). The model is, however, not able to reproduce the Obukov-Corrsin scaling for the second order structure function; $H(2) \sim k_m^{-2/3}$ given a velocity field scaling according to Kolmogorov scaling $\xi_{wn} = 2/3$.

In the work reported in the attached article ("Shell Model for Time-correlated Random Advection of Passive Scalars"), the model is extended such that the velocity field is correlated in time instead of just being delta correlated. The velocity field is generated by a Ornstein-Uhlenbeck process resulting in a signal exponentially correlated in time. The prescribed velocity field then becomes:

$$\langle u_m(t)u_n^*(t')\rangle = \frac{|v_m^2|}{\epsilon}\exp(-\frac{t-t'}{\epsilon\tau_m})\delta_{nm} \tag{8.18}$$

where now $v_m \propto k_m^{-\xi/2}$ describe the scaling of the velocity field, τ_m is the time correlation for shell m and ϵ is a parameter which determines the strength of the time correlation. For $\epsilon = 0$ the delta correlated limit is recovered. A dimensional argument gives the characteristic time for each shell:

$$\tau_m \propto \frac{1}{k_m|v_m|} \propto k_m^{\xi/2-1}, \tag{8.19}$$

and the scaling of the space- and time-correlations for each shell is then fully described by the parameter ξ. The value of $\xi = 2/3$ describes the Kolmogorov scaling of the velocity field, which is the limit explored in the article.

The model is studied analytically in the delta correlated limit and using perturbation theory the correction due to the time correlation is calculated (this part of the work is mainly due to P. Muratore-Ginanneschi). To verify the analytical work and to extend the results into the non-perturbative regime the model is integrated numerically.

The main results in the article are briefly highlighted:

- The relation between the delta correlated velocity field and the time correlated velocity field is:

$$\xi_{wn} = 1 + \frac{\xi}{2}. \tag{8.20}$$

  This mean that the value of ξ_{wn} which corresponds to the Obukov-Corrsin scaling is $\xi_{wn} = 4/3$, and explain why Benzi *et al.* (1997) were not able to find Obukov-Corrsin scaling.

- The method of Benzi *et al.* (1997) for calculating the anomalous scaling was extended to the sixth and the eight order structure functions. These results were confirmed by numerical integration of the model.
- The addition of the correlated velocity field resulted in strong anomalous corrections.
- The numerical integration of the model with time correlation also showed a strong correction to the delta correlated model for small values of the time correlation ϵ. The non universality became smaller as the physically relevant limit $\epsilon \approx 1$ was approached. However, it is not possible to say whether there is a clear saturation of the correction at some value of ϵ.

Bibliography

Anderson, R. A. (1990). Eolian ripples as examples of self-organization in geomorphological systems. *Earth-Science Reviews 29*, 77–96.

Aydin, I. (1987). *Computation and analysis of unsteady turbulent flow on a flat bottom and over rigid ripples*. Ph. D. thesis, Tohuku University.

Ayrton, H. (1910). The origin and growth of the ripple mark. *Proc. Roy. Soc. of London A84: 285.*

Bagnold, R. A. (1946). Motion of waves in shallow water, interaction between waves and sand bottoms. *Proc. Roy. Soc. of London A187*, 1–15.

Bagnold, R. A. (1954). Experiments on a gravity-free dispersion of large solid spheres in a newtonian fluid under shear. *Proc. Roy. Soc. of London A225*, 49–63.

Benzi, R., L. Biferale, and A. Wirth (1997). Analytic calculation of anomalous scaling in random shell models for a passive scalar. *Phys. Rev. Letters 78*, 4926.

Blondeaux, P. (1990). Sand ripples under sea-waves. part 1. ripple formation. *Journal of Fluid Mechanics 218*, 1–17.

Blondeaux, P., E. Foti, and G. Vittori (1996). Sand ripples under sea waves. part 4. wave-current ripples. To appear in JFM.

Blondeaux, P. and G. Vittori (1990). Oscillatory flow and sediment motion over a ripples bed. In *22. Int. Coastal Eng. conf.*, pp. 2186–2199. ASCE.

Blondeaux, P. and G. Vittori (1991). Vorticity dynamics in an oscillatory flow over an rippled bed. *Journal of Fluid Mechanics 226*, 257–289.

Bohr, T., M. Jensen, G. Paladin, and A. Vulpiani (1998). *Dynamicsal systems approach to turbulence*. Cambridge University Press.

Bohr, T., V. Putkaradze, and S. Watanabe (1997). Averaging theory for the structure of hydraulic jumps and separation in laminar free surface flows. *Phys. Rev. Letters 79*, 1038–1042.

Bradshaw, P., B. E. Launder, and J. L. Lumley (1996). Collaborative testing of turbulence models. *Journal of Fluids Engineering 118*, 243–247.

Brøker, I. (1985). Wave generated ripples and resulting sediment transport in waves. Series Paper 36, ISVA, The Danish Technical University.

Carstens, M., F. Neilson, and H. Altinbilek (1969). Bed forms generated in the laboratory under an oscillatory flow: analytical and experimental study. Technical Memorandum 28, U.S. Army Corps of Engineers, Coastal Engineering Research Center.

Cross, M. and P. Hohenberg (1993). Pattern formation outside of equilibrium. *Rev. of Mod. Phys. 65*(3), 854–1086.

Csahók, Z., C. Misbah, and A. Valance (1998). A nonlinear evolution equation for sand ripples based on geometry and conservation. Preprint: http://xxx.lanl.gov/ps/cond-mat/9811211.

Damgaard, J., R. Whitehouse, and R. Soulsby (1996). Bed-load sediment transport on steep longitudinal slopes. Submitted to: Journal of hydraulic engineering, ASCE.

Ditlevsen, P. (1996). Temporal intermittency and cascades in shell models of turbulence. *Phys. Rev. E 54*, 985–988.

Du Toit, C. and J. Sleath (1981). Velocity measurements close to rippled beds in oscillatory flow. *Journal of Fluid Mechanics 112*, 71–96.

Engelund, F. and J. Fredsøe (1976). A sediment transport model for straight alluvial channels. *Nordic Hydrology 7*, 293–306.

Foti, E. and P. Blondeux (1995a). Sea ripple formation: The heterogeneous sediment case. *Coastal Engineering 25*, 237–253.

Foti, E. and P. Blondeux (1995b). Sea ripple formation: The turbulent boundary layer case. *Coastal Engineering 25*, 227–236.

Fredsøe, J. (1974). On the development of dunes in erodible channels. *Journal of Fluid Mechanics 64*, 1–16.

Fredsøe, J. (1996). The stability of a sandy river bed. In T. Nakato and R. Ettema (Eds.), *Issues and directions in hydraulics*, pp. 99–113. Iowa Institute of Hydraulic Research.

Fredsøe, J. and R. Deigaard (1992). *Mechanics of Coastal Sediment Transport*. World Scientific.

Gallagher, E., S. Elgar, and E. Thornton (1998). Megaripple migration in a natural surf zone. *Nature 394*, 165–167.

Gledzer, E. (1973). *Sov. Phys. Dokl. 18*, 216.

Grass, A. and N. Ayoub (1982). Bed load transport of fine sand by laminar and turbulent flow. *Int. Conf. of Coastal Engineering*, 1589–1599.

Hansen, E., J. Fredsøe, and R. Deigaard (1994). Distribution of suspended sediment over wave-generated ripples. *Journal of Waterway, Port and Ocean Engineering 120*(1), 37–55.

Hoyle, R. and A. Woods (1997). Analytical model of propagating sand ripples. *Phys. Rev. E 56*(6), 6861–6868.

Hulcher, S. (1996). *Journal of Geophysical Research 101*(20), 727–744.

Hyoseob, K., B. O'Connor, and Y. Shim (1994). Numerical modelling of flow over ripples using sola method. In *24.th. Int. Conf. on Coastal Engineering, Kobe, Japan*, Volume 2, pp. 2140–2153.

Jensen, B. (1989). Experimental investigation of turbulent oscillatory boundary layers. Serier Paper 45, ISVA, the Danish Technical University.

Jensen, J. H. (1998). *Backfilling af Trenches and Dredged Channels*. Ph. D. thesis, ISVA, the Danish Technical University.

Jensen, M., G. Paladin, and A. Vulpiani (1991). Shell model for turbulent advection of passive-scalar fields. *Phys. Rev. A 45*(10), 7214.

Jensen, M., G. Paladin, and A. Vulpiani (1992). Shell model for turbulent advection of passive-scalar fields. *Phys. Rev. A 45*(10), 7214–7221.

Jonsson, I. and N. Carlsen (1976). Experimental and theoretical investigations in an oscillatory turbulent boundary layer. *Journal of Hydraulic Research 14*(1), 45–60.

Kovacs, A. and G. Parker (1994). A new vectorial bedload formulation and its application to the time evolution of straight river channels. *Journal of Fluid Mechanics 267*, 153–183.

Landau, L. and E. Lifshitz (1959). *Fluid Mechanics*. Butterworth & Heinemann.

Leonard, B. (1979). A stable and accurate convective modelling procedure based on quadratic upstream interpolation. *Computer Methods in Applied Mechanics and Engineering 19*, 59–98.

Lofquist, K. (1980). Measurements of oscillatory drag on sand ripples. In *17.th. Int. Conf. on Coastal Engineering in Sydney, Australia*, Volume 3, pp. 3087–3106.

Longuet-Higgins, M. S. (1981). Oscillating flow over steep sand ripples. *Journal of Fluid Mechanics 107*, 1–35.

Mayer, S., A. Garapon, and L. S. Sørensen (1998). A fractional step method for unsteady surface flow with applications to non-linear wave dynamics. *International Journal for Numerical Methods in Fluids 28*, 293–315.

Menter, F. (1993). Zonal two equation k-ω turbulence models for aerodynamic flows. In *AIAA-93-2906*. AIAA.

Meyer-Peter, E. and R. Müller (1948). Formulas for bed-load transport. In *Second meeting, Stockholm*, pp. 39–64. Int. Ass. for Hyd. Structures Res.

Nielsen, P. (1979). Some basic concepts of wave sediment transport. Series paper no. 20, ISVA, the Danish Technical University.

Nielsen, P. (1981). Dynamics and geometry of wave-generated ripples. *Journal of Geophysical Research 86*(C7), 6467–6472.

Nishimori, H. and N. Ouchi (1993). Formation of ripples patterns and dunes by wind-blown sand. *Phys. Rev. Lett. 71*, 197.

Nishimori, H., M. Yamasaki, and K. Andersen (1998). A simple model for the various pattern dynamics of dunes. *International journal of modern physics B 12*(3), 257–272.

Parisi, G. (1990). A mechanism for intermittency in a cascade model for turbulence. Preprint of the University of Rome II. Unpublished.

Patankar, S. V. (1980). *Numerical Heat Transfer and Fluid Flow*. Hemisphere, New York.

Patel, V. C. and J. Y. Yoon (1995). Application of turbulence model to separated flow over rough surfaces. *J. Fluids Engineering 117*, 234–241.

Perrier, G. (1996). *Numerical modelling of the transport of non-cohesive sediments by waves and currents over a rippled bed*. Ph. D. thesis, Departement Laboratoire National D'Hydraulique, France.

Perrier, G., E. A. Hansen, C. Villaret, R. Deigaard, and J. Fredsøe (1994). Sediment transport over ripples in waves and current. *Coastal Engineering*, 2043–2057.

Putkaradze, V. (1997). *Local structures in extended systems*. Ph. D. thesis, The Niels Bohr Institute, University of Copenhagen.

Raudkivi, A. (1997). Ripples on stream bed. *Journal of Hydraulic Engineering*, 58–64.

Rayleigh (1915). The principle of similitude. *Nature*, 66–68.

Saffman, P. (1970). A model for inhomogeneous flow. *Proc. Roy. Soc. of London A317*, 417–433.

Sarpkaya and Isaacson (1981). *Mechanics of Wave Forces on Offshore Structures*. Van Nostrand Reinhold.

Sato, S., H. Uehara, and A. Watanabe (1986). Numerical simulation of the oscillatory boundary layer flow over ripples by a k-ϵ turbulence model. *Coastal Eng. Japan 29*, 65–78.

Scherer, M. A., F. Melo, and M. Marder (1999). Sand ripples in an oscillating annular sand-water cell. *Physics of Fluids 11*(1), 58–67.

Sleath, J. (1976). On rolling-grain ripples. *Journal of Hydraulic Research 14*(1), 69–81.

Sleath, J. (1982). Friction coefficients of rippled beds in oscillatory flows. *Continental Shelf Research 1*(1), 33–47.

Stegner, A. and J. E. Wesfreid (1998). Dynamical evolution of sand ripples under water. Submitted to Phys. Rev. Letters.

Terzidis, O., P. Claudin, and J.-P. Bouchaud (1998). A model for ripple instabilities in granular media. *The European Physical Journal 5*, 245–249.

Tjerry, S. (1995). *Morphological calculation of dunes in alluvial rivers*. Ph. D. thesis, ISVA, the Danish Technical University.

Tsujimoto, G., N. Hayakawa, M. Ichiyama, Y. Fukushima, and Y. Nakamura (1991). A study on suspended sediment concentration and sediment transport mechanism over rippled sand bed using a turbulence model. *Coastal Eng. in Japan 34*(2), 177–189.

Versteeg, H. K. and W. Malalasekera (1995). *An Introduction to Computational Fluid Dynamics*. Longman Scientific and Technical.

Vittori, G. (1989). Non-linear viscous oscillatory flow over a small amplitude wavy wall. *Journal of Hydraulic Research 27*(2), 267–280.

Vittori, G. and P. Blondeaux (1990). Sand ripples under sea waves. part 2. finite-amplitude development. *Journal of Fluid Mechanics 218*, 19–39.

Vittori, G. and P. Blondeaux (1991). Sand ripples under sea waves. part 3: Brick-pattern ripple formation. *Journal of Fluid Mechanics 239*, 23–45.

Wiberg, P. and C. Harris (1994). Ripple geometry in wave-dominated environments. *Journal of Geophysical Research 99*(C1), 775–789.

Wilcox, D. C. (1988). Reassessment of the scale-determining equation for advanced turbulence models. *AIAA Journal 26*(11), 1299–1310.

Wilcox, D. C. (1993a). Comparison of two-equation turbulence models for boundary layers with pressure gradient. *AIAA Journal 31*(9), 1414–1421.

Wilcox, D. C. (1993b). *Turbulence Modeling for CFD.* DCW industries Inc.

Yamada, M. and K. Ohkitani (1987). *Prog. Theor. Phys 56*, 4210.

Zijlema, M. (1996). On the construction of a third-order accurate monotone convection scheme with application to turbulent flows in general domains. *Int. Journal for Numerical Methods in Fluids 22*, 619–641.

Attached article:

Wave plus current over a ripple-covered bed

Jørgen Fredsøe, Ken H. Andersen and B. Mutlu Sumer

Submitted to: Coastal Engineering

Attached article:

Shell Model for Time-Correlated Random Advection of Passive Scalars

K. H. Andersen and P. Muratore-Ginanneschi

Submitted to: Physical Review E.

Attached article:

Bursts and Shocks in a Continuum Shell Model

K. H. Andersen, T. Bohr, M. H. Jensen and P. Olesen

Proceeding of the Conference on Chaos and Disorder
in Honour of **Giovanni Paladin**
Journal de Physique IV (8), Pr6-121–130 (1998).

Attached article:

Pulses in the Zero-Spacing Limit of the GOY Model

K.H. Andersen, T. Bohr, M.H. Jensen, J.L. Nielsen and P. Olesen

Draft version.